Development of a Magnetic Gear for Dry-Cooling Power Plant Applications

by

Alexander Matthee

Thesis presented in partial fulfilment of the requirements for the degree of Master of Engineering (Electrical) in the Faculty of Engineering at Stellenbosch University

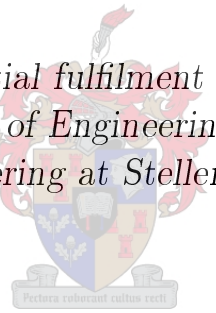

Department of Electrical and Elecgtronic Engineering,
University of Stellenbosch,
Private Bag X1, Matieland 7602, South Africa.

Supervisor: Prof. R-J. Wang

March 2017

Stellenbosch University https://scholar.sun.ac.za

Declaration

By submitting this thesis electronically, I declare that the entirety of the work contained therein is my own, original work, that I am the sole author thereof (save to the extent explicitly otherwise stated), that reproduction and publication thereof by Stellenbosch University will not infringe any third party rights and that I have not previously in its entirety or in part submitted it for obtaining any qualification.

Date: March 2017

Copyright © 2017 Stellenbosch University
All rights reserved

Stellenbosch University https://scholar.sun.ac.za

Abstract

Development of a Magnetic Gear for Dry-Cooling Power Plant Applications

A. Matthee

Department of Electrical and Elecgtronic Engineering,
University of Stellenbosch,
Private Bag X1, Matieland 7602, South Africa.

Thesis: MEng (Elec)

November 2016

Due to excessive mechanical gear failure in air cooled condenser (ACC) for dry cooling applications there is a need to investigates possible alternatives. In this study research is conducted into magnet gear (MG) technologies which could potentially replace mechanical gears for dry cooling applications. Three promising magnetic gear topologies are identified which include the magnetic harmonic gear (MHG), the magnetic planetary gear (MPG) and the flux modulated magnetic gear (FMMG).

Of the three identified MG topologies the MPG and the FMMG are deemed more viable from a manufacturing perspective. Two small prototypes are constructed and tested to gain further knowledge on the potential advantages and disadvantages of each topology. The PMG achieved the highest torque density of 139 kNm/m^3 compared to the FMMG with 87 kNm/m^3. Although the PMG achieved the highest stall torque output it also suffered from the highest losses with efficiency of 70% at full load compared to the FMMG prototype with 95% efficiency. These losses were caused by frictional losses in the PMG due to mechanical complexity. The relatively simple mechanical design of the FMMG topology makes it a suitable candidate for this study.

To have a more objective comparison between the FMMG and the mechanical gear, a new FMMG prototype is optimally designed using 2D finite element method (FEM) according to the same specifications of an existing single-stage helical mechanical gear. The design is further refined to achieve higher efficiency after which the performance is verified by 3D FEM calculation. The

Stellenbosch University https://scholar.sun.ac.za

mechanical design is also checked by performing mechanical stress analysis on all the critical sections of the design.

Experimental tests of both the FMMG and the equivalent mechanical gear are conducted for performance comparison. The mechanical gear achieved a maximum efficiency of 95% under rated conditions of 132 Nm torque and 160 rpm on the output shaft. The gear is also tested at 1.5 pu condition (198 Nm) and obtained an efficiency of 96%. The magnetic gear achieved results trailing within 2% of the mechanical gear's efficiency. The measured maximum efficiency of the FMMG are 93.5% and 95% at rated and 1.5 pu conditions, respectively. The power rating of the gears at 1.5 pu conditions is about 3.3 kW.

The magnetic gear performed reasonably well in comparison with the mechanical counterpart. Both gears achieved efficiency in the mid 90% range. With the added advantage of over load protection and reduced noise transfer the magnetic gear appears to be a valid replacement for the mechanical gear in this specific application.

Stellenbosch University https://scholar.sun.ac.za

Uittreksel

Ontwikkeling van 'n Magnetiese Rat vir Droë Verkoeling Toepassings in Kragstasies

A. Matthee

Departement Elektriese en Elektroniese Ingenieurswese,
Universiteit van Stellenbosch,
Privaatsak X1, Matieland 7602, Suid Afrika.

Tesis: MIng (Elek)

November 2016

As gevolg van oormatige meganiese rat falings in lug verkoelde kondensators vir droë lug verkoeling toepassings is daar 'n groot nood vir ondersoek in moontlike alternatiewe. Navorsing word in hierdie studie voltooi in die magnetiese rat veld om 'n moontlike plaasvevanger vir meganiese rat to verkry. Drie belowende magnetiese rat topologieë is geïdentifiseer naamlik die harmoniek magnetiese rat (HMR), die magnetiese planetêre rat (MPR) en die vloed modulerende magnetiese rat (VMMR).

Uit hierdie drie keuses is die MPR en die VMMR beskou as die mees belowend van 'n vervaardigings oorpunt. Twee klein skaal prototiepes is gebou en getoets om verdere kennis op te bou oor die potensiale voordele en nadele van elke topologie. Die PMR het die hoogste wringkrag digtheid van 139 $\mathrm{kNm/m^3}$ bereik in vergelyking met die VMMR van 87 $\mathrm{kNm/m^3}$. Alhoewel die PMR die hoogste wringkrag digtheid bereik het dit ook die meeste verliese ervaar met 'n effektiewiteit van 70% teen vollas in vergelyking met die VMMR met 'n effektiewiteit van 95%. Die verliese in die PMR is veroorsaak deur wrywing as gevolg van meganiese kompleksiteit. Die relatiewe eenvoudige meganiese ontwerp van die VMMR maak die hierdie rat topologie 'n aanvaarbare kandidaat vir hierdie studie.

Om 'n meer objektiewe vergelyking tussen die VMMR en die meganiese rat te bereik is 'n nuwe VMMR prototiepe optimaal ontwerp, deur middel van 2D eindige element metode (EEM), volgens dieselfde spesifikasies as 'n bestaande

Stellenbosch University https://scholar.sun.ac.za

enkel fase heliese meganiese rat. Die ontwerp is verder verfyn om 'n hoër effektiewiteit te bereik wat daarna bevestig is deur 3D EEM simulasies. Die meganiese ontwerp van die VMMR prototiepe is ook nagegaan deur middel van 'n meganiese stress analiese op kritiese dele van die ontwerp.

Toetse van beide die VMMR en die ekwivalente meganiese rat word uitgevoer vir prestasie vegelyking. Die meganiese rat het 'n maksimum effektiewiteit bereik van 95% onder gegradeerde omstandighede van 132 Nm wringkrag en 160 rpm spoed op die uittree as. Die rat het ook 'n effektiewiteit van 96% bereik onder 1.5 maal toets omstandighede van (198 Nm). Die magnetiese rat het kort op die hakke van die meganiese rat presteer en binne 2% van die meganiese rat se effektiewiteit bereik. Die gemete maksimum effektiewiteit van die VMMR is 93.5% and 95% by gegradeerde en 1.5 maal gegradeerde omstandigehede. Die krag uittree by 1.5 maal gegradeerde omstandighede is 3.3 kW.

Die magnetiese rat het redelik goed presteer in vergelyking met die meganiese eweknie. Altwee ratte het effektiewiteit bereik van rondomby 95%. Met die begevoegde voordeel van oorlading beskerming en verminderde geraas oordrag betoon die magnetiese rat waarde as 'n moontlike plaasvervanger die 'n meganiese rat vir hierdie toepassing.

Stellenbosch University https://scholar.sun.ac.za

Acknowledgements

I would like to acknowledge the following people and express my sincerest gratitude for their assistance in the completion of this study.

Firstly to my study leader Professor Rong-Jie Wang who always provided me with guidance and allowed a flexible structure for me to thrive and complete my master's degree.

To all my friends at Stellenbosch, many of whom are also in the process of completing studies, for all the support and good times I will never forget.

To Dr. Danie Els for all his mechanical knowledge without which catastrophic failure would have been inevitable.

To Charles Agenbach for all his help during the mechanical design and endless hours passing around wrenches and tools during the test setup and testing phase.

And finally for all the lab and workshop staff who helped me, usually in a crisis, to do whatever needed to be done to aid in my testing or construction of the prototypes.

Stellenbosch University https://scholar.sun.ac.za

List of Publications

The following publications refer to the small scale prototype magnetic gears developed preceding the large scale prototype of this study.

1. Matthee, A., Gerber, S., Wang, R.-J., "A high performance concentric magnetic gear," in Proceedings of the Southern African Universities Power Engineering Conference, (SAUPEC), Johannesburg, South Africa, pp. 203–207, 28-29 January 2015; doi: 10.13140/RG.2.1.1493.6167

2. Wang, R.-J., Matthee, A., Gerber, S., Tlali, P. M., "Calculation of torque performance of a novel magnetic planetary gear," IEEE Magnetics Letters, vol. 7, issue 1, 1303805, 2016; doi: 10.1109/LMAG.2016.2564948

Stellenbosch University https://scholar.sun.ac.za

Contents

Stellenbosch University https://scholar.sun.ac.za

Stellenbosch University https://scholar.sun.ac.za

List of Figures

Stellenbosch University https://scholar.sun.ac.za

Stellenbosch University https://scholar.sun.ac.za

Stellenbosch University https://scholar.sun.ac.za

Stellenbosch University https://scholar.sun.ac.za

List of Tables

Stellenbosch University https://scholar.sun.ac.za

Stellenbosch University https://scholar.sun.ac.za

Nomenclature

Variables

E	Young's modulus	[m]
θ	Rotation angle	[rad]
τ	Shear stress	[Pa]
η	Efficiency	[%]
S_y	Shear yielding strength	[Pa]
S_{ut}	Ultimate tensile strength	[Pa]
n_z	Safety factor in z axis	[units]
λ_0	Gap initial position	[mm]
λ_t	Gap time varying position	[mm]

Abbreviations

MG	Magnetic gears
HS	High speed
LS	Low speed
PMG	Planetary magnetic gear
$FMMG$	Flux modulated magnetic gear
PM	Permanent magnets
$NdFeB$	Neodymium Iron Boron
PMM	Permanent magnet machine
CSP	Concentrated solar power
HMG	Harmonic magnetic gear
RTC	reversible temperature coefficient
CNC	Computer numerical control
FE	Finite element
TS	Torque sensor
UUT	Unit under test
ACC	Air cooled condenser
FFT	Fast fourier transform

Stellenbosch University https://scholar.sun.ac.za

FEA	Finite element analysis
FEM	Finite element method
$MMFD$	Modified method of feasible direction
$2D$	Two-dimensional
$3D$	Three-dimensional
LCD	Lowest common denominator
LCM	Lowest common multiple
$PEEK$	PolyEtherEtherKetone

Symbols

k	Kilo
M	Mega
m	Milli
rpm	Revolutions per minute
Nm	Newton metre
W	Watts
Q_c	Heat energy of cold reservoir
Q_h	Heat energy of hot reservoir
Q_W	Heat energy converted to work
T_H	Temperature of hot reservoir
T_C	Temperature of cold reservoir
P_w	Number of sinusoidal cycles between HS and LS rotors
ω_h	Angular velocity of HS rotor
ω_l	Angular velocity of LS rotor
p_l	Number of magnetic pole pairs on the LS rotor
p_h	Number of magnetic pole pairs on the HS rotor
p_s	Number of magnetic pole pairs on the PM carrier
z_r	Number of teeth on the ring gear
z_s	Number of teeth on the sun gear
z_p	Number of teeth on the planet gear
ω_r	Angular velocity of the ring gear
ω_s	Angular velocity of the sun gear
ω_c	Angular velocity of the carrier
N_s	Number of segments on the modulator
G_r	Gear ratio
f_c	Cogging torque factor
N_c	Lowest common denominator

Stellenbosch University https://scholar.sun.ac.za

BH_{max}	Maximum energy product
B_r	Remanent magnetic flux
H_c	Coercive magnetic force
ΔT	Change in temperature
E_T	End effect ratio

Stellenbosch University https://scholar.sun.ac.za

Chapter 1

Introduction

Globally the majority of power plants burns fossil fuels such as coal, oil, natural gas and converts the thermal energy to electricity. The underlying working principle of this energy conversion is closely related to the two thermodynamics laws [1, 2, 3]. The theory of a heat engine is often used to explain the concept of thermal energy, work and exhaust heat in a thermal power plant.

As shown in Figure 1.1, for a heat cycle to work efficiently the temperature difference between the heat source and the cold reservoir should theoretically be as large as possible, but is of course limited to what is practically achievable. The relation between the work performed (W), heat taken from the hot reservoir (Q_H) and heat rejected to cold reservoir (Q_C) is governed by the following equation:

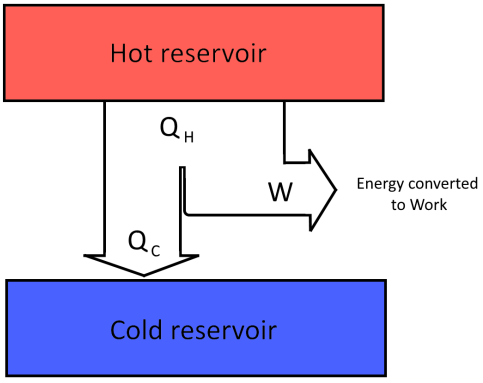

Figure 1.1: The heat flow of a heat engine.

$$W = Q_H - Q_C = \left(1 - \frac{T_C}{T_H}\right) Q_H \tag{1.1}$$

Stellenbosch University https://scholar.sun.ac.za

where T_H and T_C are temperatures of hot and cold reservoir, respectively. The efficiency of the heat engine (η) can thus be calculated using:

$$\eta = \frac{W}{Q_H} = 1 - \frac{T_C}{T_H} \tag{1.2}$$

It is therefore essential for the cold reservoir to effectively dissipate heat into the surroundings to maintain a low temperature T_C for optimum system operation [4].

Recent years showed an increase in the use of cleaner renewable energy sources (e.g. wind, solar and hydro) for electrical power generation. Among them, the concentrating solar power (CSP) technologies have received considerable attention for utility scale applications. This may be because for CSP plants the heat can be stored quite efficiently and used for power generation even after sunset [5, 6]. Figure 1.2 shows a typical power tower type CSP power plant and a diagram of the plant layout.

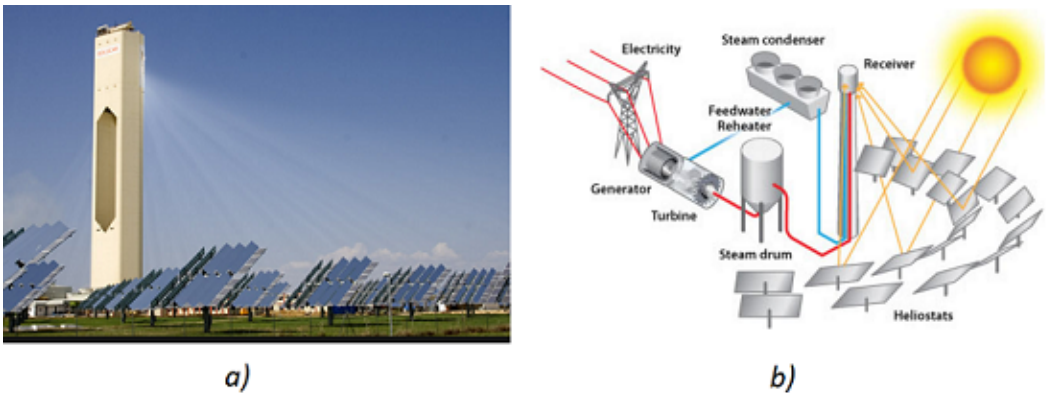

Figure 1.2: CSP power plant (a) collector [7] (b) plant layout diagram [8]

Similar to the principle of a heat engine, the thermal receiver (hot reservoir) of a CSP power plant can be heated up to 300 to 500°C [9]. The cold reservoir in Figure 1.2(b) exists in the form of a steam condenser. This component is used to cool the steam flowing through the system. Cooling on this scale can be achieved amongst other methods such as water cooling, natural convection of air through parabolic towers or in the case relevant to this study, by air cooled condensers (ACCs).

ACCs are used in the cooling phase of power plants where water cooling is not readily available [10, 11]. In certain regions water may be a scare commodity or perhaps legislation may not allow the use of water for cooling. ACC technology does not require water to condense the process fluid. The process involves exhaust steam from the turbine flowing through tube bundles of an

Stellenbosch University https://scholar.sun.ac.za

ACC and is condensed in these parallel flow tubes using air flow induced by large fans [12]. Figure 1.3 shows a section of an A-shaped ACC assembly with a zoomed-in view of the tubes used to conduct heat from steam. The heated steam arrives in the large pipes on top of the ACC and the fans force air from beneath.

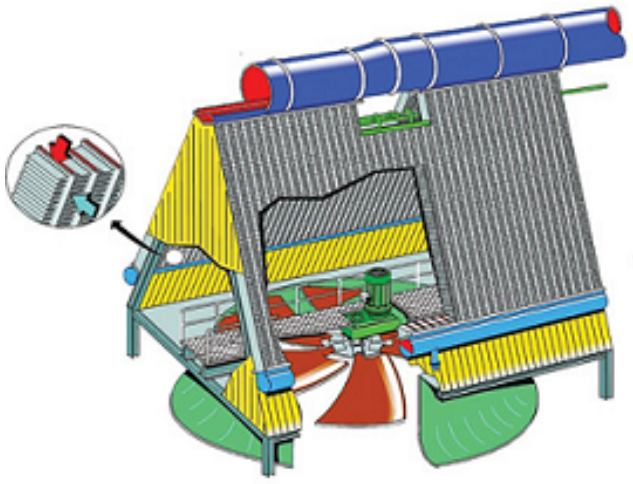

Figure 1.3: The configuration of an A-shape ACC assembly [13]

The air flows through radiator tubes allow the heat to be transferred into the atmosphere via forced convection. Figure 1.4 shows photos of the inside of an A-frame ACC cooling unit. In Figure 1.4(a) a fan during operation and in (b) a large induction motor used to drive the system. The mechanical gear is situated between the motor and the fan but is not visible in these images. A typical power station would consist of hundreds of these ACC assemblies working in unison to regulate the cold reservoir.

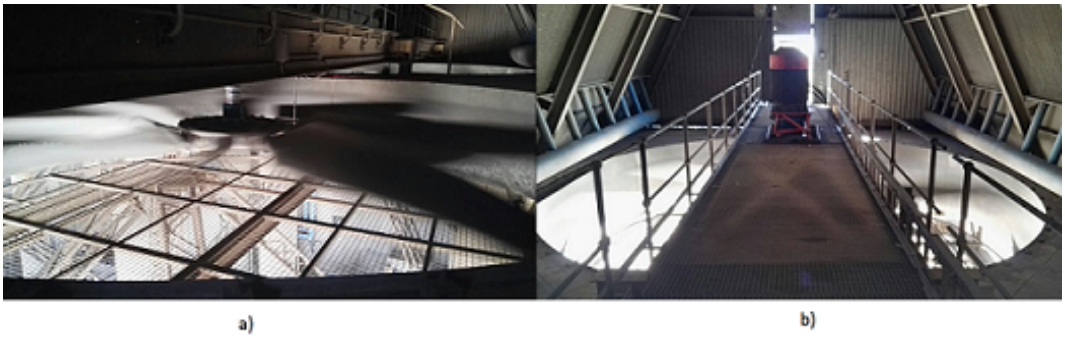

Figure 1.4: ACC unit in operation with (a) fan and (b) induction motor

Stellenbosch University https://scholar.sun.ac.za

Figure 1.5 illustrates the major moving mechanical parts of an ACC assembly clearly showing the large induction motor connected to a mechanical gear, which reduces the rotational speed and increases the torque of the motor, connected to a fan.

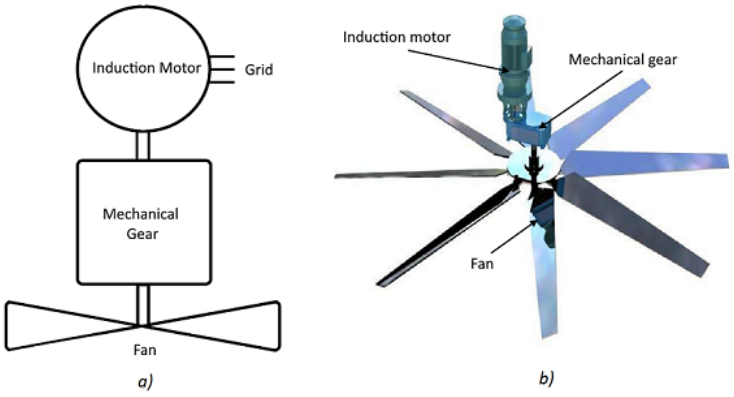

Figure 1.5: (a) ACC moving parts assembly diagram (b) CAD drawing of moving parts in an ACC [14]

Figure 1.6 shows an image captured of a portion of the ACC units from below at Matimba power station in South Africa. The total number of ACC units is 288.

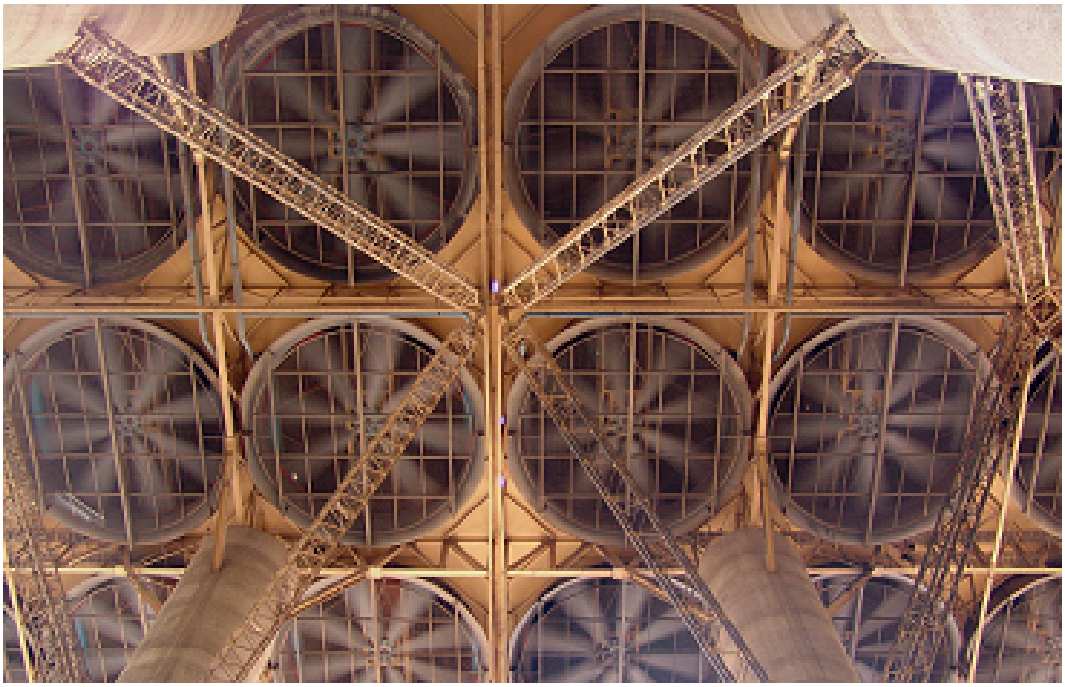

Figure 1.6: Image of ACC units from below [15]

Stellenbosch University https://scholar.sun.ac.za

1.1 Problem statement

CSP power plants require many large ACC units to perform the cooling operation. These ACC units are driven by line-fed induction motors due to the fact that using a soft starting drive would decrease running efficiency, but the direct-online starting causes large start torques to be experienced throughout the whole system [16].

A recent investigation on ACC failure recorded the number of failures since inception amounts to over 30 gearbox units per year on average to date out of 288 gearboxes at Matimba power station [14].

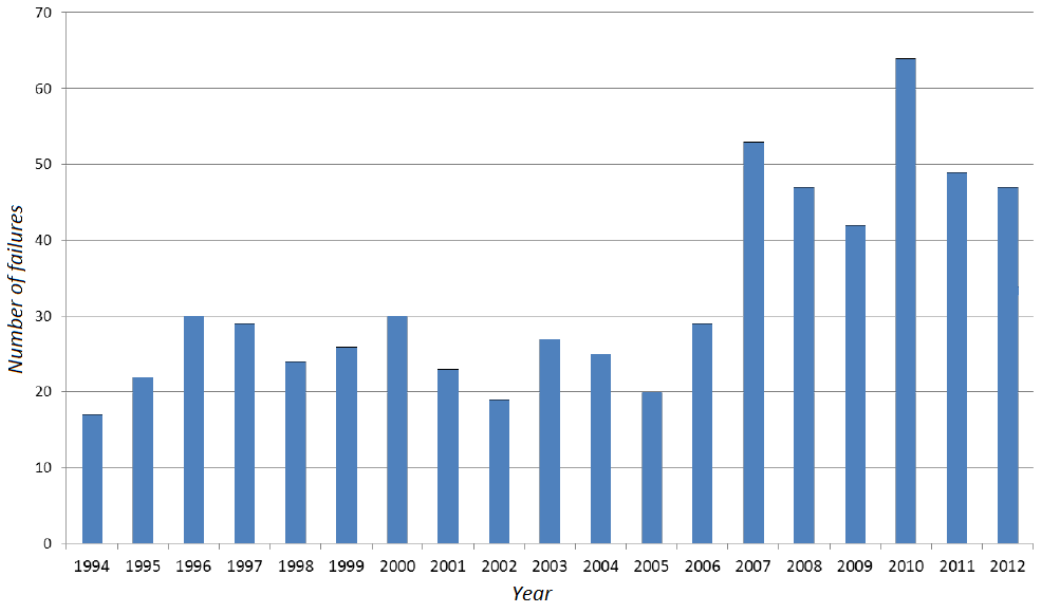

Figure 1.7: Annual number of failures since inception [14]

These units are run for months without shutting down therefore the cost of running the units efficiently outweigh the stress caused momentarily on these units by starting in direct-online configuration [17]. Fan vibrations [18] as well as wind [19] caused load spikes which are detrimental to gear performance and lifespan.

Another large concern is the need for continuous oil change and monitoring. Large volumes of expensive oil needs to be changed on every gearbox on an annual or bi-annual basis. Lack of the oil or incorrect oil causes damage such as micro pitting on the gear teeth, reducing performance and eventually resulting in failure. A common source of oil leak is caused by dry wells working looses from their press fit. With the gears running under extreme load fluctuation

Stellenbosch University https://scholar.sun.ac.za

conditions and questionable oil change practices failures such as is shown in Figure 1.8 occur frequently [14]. The chipping and micro pitting on the gear teeth can clearly be seen in this image.

Figure 1.8: Damaged gears of an ACC gearbox [14]

The operation of a mechanical gear unfortunately requires contact between gear teeth which transmit load spikes, vibration and require cooling and lubrication to operate reliably. These inherent qualities are part of the technology and cannot easily be circumvented. Gear failures have been reported in the field sometimes mere months after installation [20]. It is therefore warranted to investigate possible alternatives.

Stellenbosch University https://scholar.sun.ac.za

1.2 Reseach aims

The objective of this study is to investigate possible alternatives to improve the reliability of ACCs in the field. The best suited Magnetic gear (MG) design is to be investigated and evaluated to compare the possible replacement of mechanical gears in the field with MGs. A mechanical gear will be tested and these results will be used as a benchmark to compare directly the performance of an MG in all aspects. Previously MGs have been designed and tested in lab conditions. Although they show promising results, a clear advantage is not proven as mechanical gears and MGs has not been compared with exact load and speed conditions.

Inherent characteristics of MGs are expected to mitigate such problems as previously mentioned. With overload protection and resistance to vibration transfer, due to no mechanical contact between input and output shafts, the MG proposed may prove to reduce downtime of these ACC systems as well as boost efficiency. In this study an MG is designed and tested to be compared directly with a mechanical gear in the same class. The objectives are as follows:

- Investigate alternatives to mechanical gears to improve the reliability of ACCs
- Design a highly efficient MG in similar power class as the reference mechanical gear
- The MG should be tested and compared to a mechanical gear under similar load conditions.
- The ultimate goal is to determine if the MG is superior to the mechanical gear in performance and service life.

1.3 Research approach

Existing gear technologies will be examined to investigate possible replacements for the mechanical gear. The most promising magnetic gear topologies will be further investigated and possibly developed into a small scale prototype. This should provide additional information to make the most advantageous design choice.

The selected topology will be designed according to the specifications of a commercial mechanical gear. This will provide valuable insights on the areas where magnetic gears are dominant or lacking. The mechanical gear will also be used as a benchmark for performance comparison to the MG prototype.

Stellenbosch University https://scholar.sun.ac.za

For the initial electromagnetic design 2D Finite element (FE) software is used. This allows rapid development simulations to be performed to arrive at a design which promises comparative performance to the mechanical counterpart. The 2D software also allows multiple iterations of simulations to be performed to optimise the design by use of commercial optimisation software. To verify the 2D FE design, 3D FE analyses will also be conducted. The 3D FE simulation is more time consuming but approaches results which is closer to what is achieved in practice. The 3D FE simulation is therefore only used once the design has been optimised by making use of 2D FE software.

From the optimised and verified simulations the active components are then exported to CAD drawings. To support the active components of the gear a mechanical design is performed for the structure of the gear, shafts, casing and all required manufacturing of parts and auxiliary tools required to perform assembly of the gear.

The mechanical parts will be reviewed. After satisfactory design refinement has taken place all components required will need to be converted to drawings to be manufactured. The manufactured components will be assembled according to the assembly plan.

The mechanical gear is then tested according to all required test specifications. Once the series of test procedures have been conducted the magnetic gear is subjected to identical tests and the performance is compared.

1.4 Layout of the thesis

- Chapter 2: Different MG topologies will be evaluated and a suitable topology will be identified for the project.
- Chapter 3: The design aspects of the chosen gear topology will be presented.
- Chapter 4: The design and optimisation procedure of the chosen gear topology will be discussed.
- Chapter 5: The construction and manufacturing aspects of the magnetic gear design will be described.
- Chapter 6: The performance evaluation and gear comparison will be conducted.
- Chapter 7: This will be the conclusion of this study's results as well as any recommendations for future work.

Stellenbosch University https://scholar.sun.ac.za

Chapter 2

Magnetic gear technologies

Magnetic gearing is by no means a new idea. A patent was issued for early magnetic gear (MG) designs as far back as the year 1901 [21]. These early gears suffered from very low torque density and therefore did not receive much attention from industry at the time. However, with breakthroughs in magnet technology such as Neodymium Iron Boron (NdFeB) in the 1980s and novel design topologies in the past two decades, the technology has drastically improved in effectiveness and is therefore receiving increasingly more attention from industry and research establishments.

Early magnetic gears mainly focussed on spur type and worm type designs [22]. These were essentially designed according to the mechanical equivalent but with magnets used to repel and attract one another hence realising a gear ratio. Figure 2.1 shows some early magnetic spur gear designs. A magnetic worm gear patented in 1972 is displayed in Figure 2.2 [23].

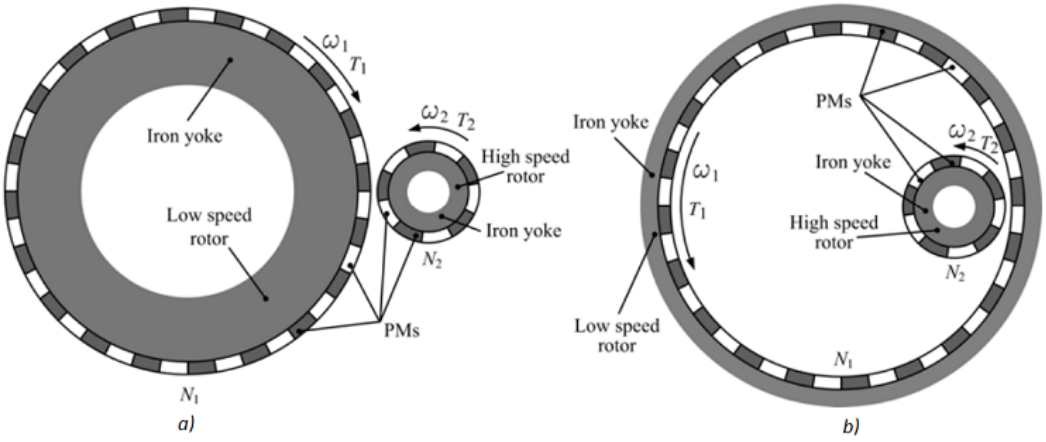

Figure 2.1: Early magnetic gears with (a) Spur gear (b) Internal ring gear [24]

Stellenbosch University https://scholar.sun.ac.za

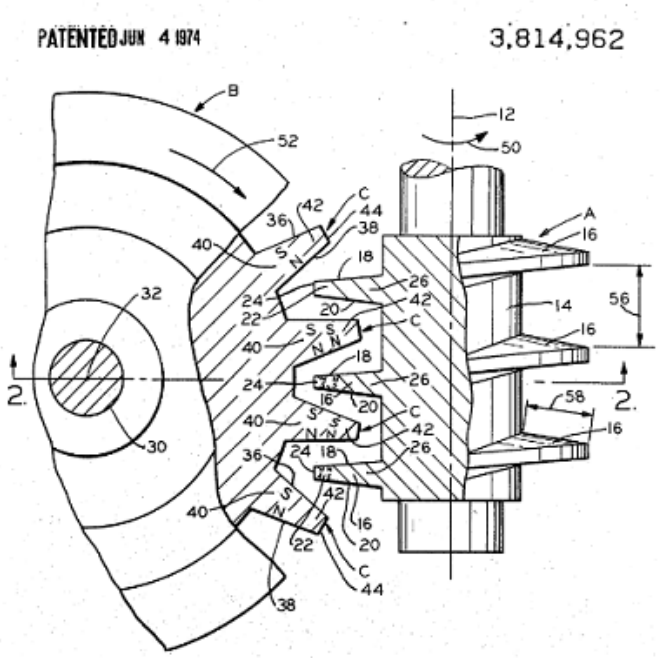

Figure 2.2: Worm gear patented in 1974 [23]

In general, these early designs suffered from very poor torque density due to ineffective magnetic coupling as well as the much lower energy density of permanent magnet materials compared with modern permanent magnets.

In 2001 a paper was published which proved a flux modulated magnetic gear could achieve a high torque density [25]. This caused a spike in research into the field as MGs have finally reached the point of competing with traditional mechanical gears. With MGs now having potential comparable torque densities to common spur or helical gears [25] as well as advantages such as no contact between input and output shafts, high efficiency, reduced noise and overload protection, many potential commercial applications can now have MGs as possible replacements of mechanical gears.

Although magnetic gears can be designed almost for each mechanical gear type as shown in Figure 2.3, so far there are only a few MG topologies that demonstrate competitive torque capability against mechanical counterparts. They are flux modulated magnetic gears (FMMG) (see Figure 2.4(a)) [26, 27, 28, 29], magnetic harmonic gears (see Figure 2.4(b)) [30, 31], and magnetic planetary gears (MPG) (see Figure 2.4(c)) [22]. One common feature of the three MG topologies is that almost all of the magnetic poles are contributing to torque transfer at any given time [22].

Stellenbosch University https://scholar.sun.ac.za

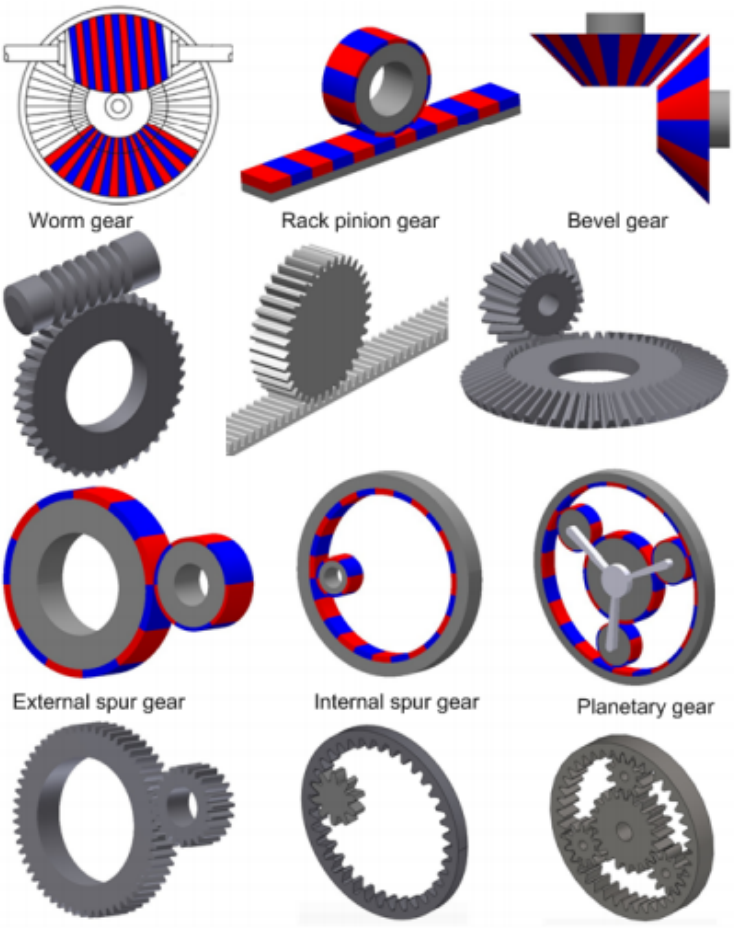

Figure 2.3: Mechanical and similar magnet gears [22]

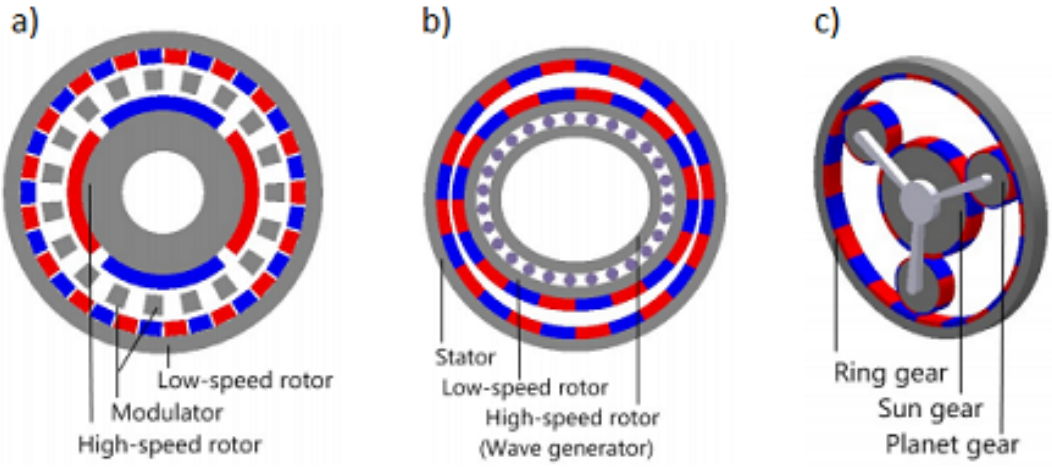

Figure 2.4: (a) Flux modulated magnetic gear, (b) Harmonic magnetic gear, (c) Magnetic planetary gear [22]

Stellenbosch University https://scholar.sun.ac.za

2.1 Harmonic magnetic gears

As illustrated in Figure 2.4(b), a harmonic magnetic gear (HMG) contains three concentric components, namely, a stationary PM carrier, a high-speed rotor and a flexible low-speed rotor. The key advantages of a HMG include high torque density, high gear ratio and ripple free torque transmission [32].

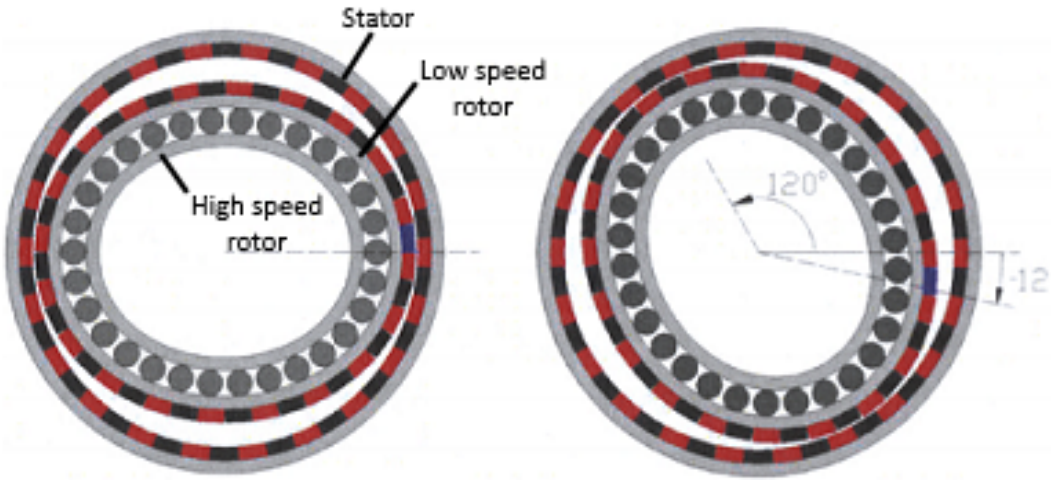

Figure 2.5: Harmonic gear with 10:1 gear ratio [32]

The HMG operates as follows: As the high-speed rotor rotates it deforms the flexible low-speed PM rotor creating sinusoidal time-varying of the air-gap between the low-speed rotor and PM carrier. This variation in air-gap modulates the field produced by the PMs on the low-speed rotor and a dominant asynchronous space harmonic field is produced which couples with the magnetic fields of the PM carrier to achieve torque transmission and gear action [32].

The sinusoidal variation in air-gap width can be mathematically expressed as in Equation (2.1):

$$\text{gap}(\theta, t) = \lambda_0 + \lambda_t \cos\left(P_\omega(\theta - \omega_t)\right) \tag{2.1}$$

with λ_0 and λ_t the initial gap size and gap width, respectively and ω_t the angular velocity of the high-speed rotor and P_ω the number of sinusoidal cycles between the low-speed rotor and PM carrier due to the shape of the rotor. P_ω can be one, two or three depending on mechanical construction [32, 33]. For $P_\omega = 2$, the gear ratio can be expressed as:

$$\frac{\omega_h}{\omega_l} = Gr = \frac{-P_l}{2} \tag{2.2}$$

Stellenbosch University https://scholar.sun.ac.za

with ω_l and P_l the angular velocity and number of magnetic pole pairs on the LS rotor, respectively and ω_h the angular velocity of the HS rotor [32]. For the gear in Figure 2.5 with $P_l = 20$ and $P_\omega = 2$ the resultant gear ratio is 10:1. The radial flux density waveform of the gear due to the LS PMs in the air-gap is given in Figure 2.6(a). The working harmonic is labelled in Figure 2.6 (b) as $P_l + P_\omega$ and this couples with the magnetic field of the PM carrier. The number of magnetic pole pairs on the PM carrier P_s must therefore satisfy Equation (2.3) [33]:

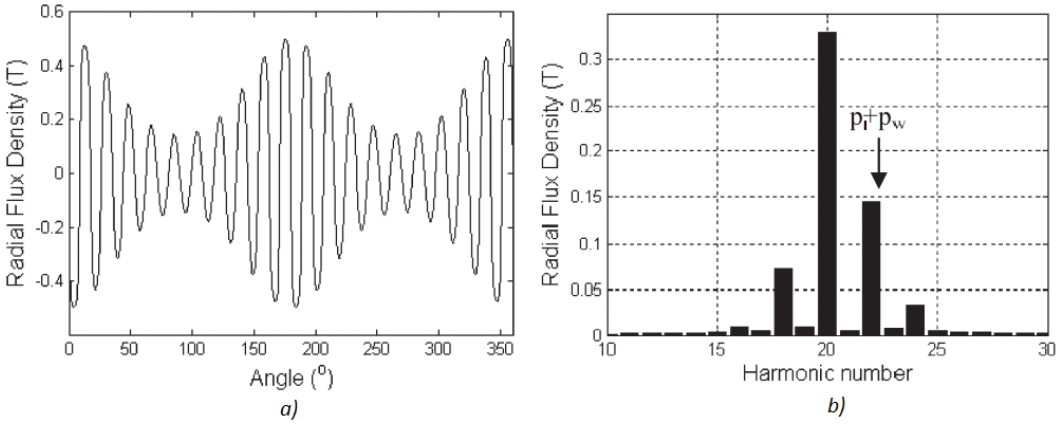

Figure 2.6: Radial flux density waveform distribution in the air-gap [33]

$$P_s = P_l + P_\omega \tag{2.3}$$

This agrees with the working harmonic order labelled in Figure 2.6 (b). The harmonic gear achieves almost ripple free torque output according to [32, 33].

Although the performance of this type gear seems promising, it does have a very complex mechanical structure and would be difficult to manufacture. As can be seen in Figure 2.5 the high-speed rotor or wave generator of the gear requires a flexible oval structure in order to operate. A fundamental part of the operation of the HMG is the mechanism for creating a time varying air-gap in a sinusoidal fashion between the low-speed shaft and high-speed shaft.

For this to be achieved the gear requires a rigid oval structure which moves a flexible component using bearings or rollers to shape the magnet carrying wave generator [34]. As the aim of this study is to investigate a possible replacement for an application with unreliable mechanical gears, a complex design with many moving parts will not be a good option. Harmonic gears are also more suited to a slightly higher gear ratio required for the purpose of this study [30].

Stellenbosch University https://scholar.sun.ac.za

2.2 Magnetic planetary gear

Planetary gears are commonly used for high torque applications such as the first stage of the wind turbine gearbox [35]. The planetary gear consists of three major components. These include the sun gear and ring gear as well as the carrier which structurally supports the planetary gears. A typical layout of a mechanical planetary gear is shown in Figure 2.7. Under normal circumstances one of these three components will be kept stationary while the other two are free to rotate at the specified gear ratio [29].

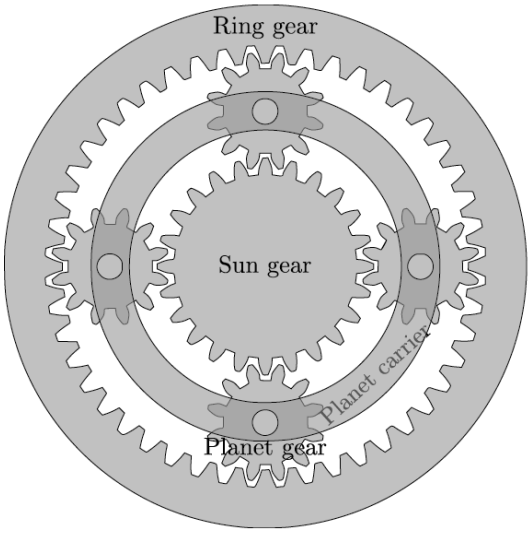

Figure 2.7: Mechanical planetary gear

The gear ratio depends on radii of the components which in case of the mechanical planetary gear is a function of the number of teeth per gear. This relationship between the number of teeth on components is governed by the following equation with ring gear (z_r), sun gear (z_s) and planet gear (z_p):

$$z_r = z_s + 2z_p \tag{2.4}$$

Angular velocity of the variables; sun gear (ω_s), ring gear (ω_r) and planet carrier (ω_c) is calculated by Equation 2.5.

$$\omega_s z_s + \omega_r z_r = \omega_c(z_s + z_r) \tag{2.5}$$

MGs operate similarly to mechanical gear except that permanent magnets replace the teeth of the mechanical gear. A magnetic planetary gear generally will have PMs poles which satisfy the same relationship as in Equation (2.4). To maintain synchronism the number of planet gears should be selected with care [31]. Figure 2.8 illustrates an example of a magnetic planetary gear. Depending on which component is stationary, three transmission modes with different gear ratios can be realized for a planetary gear [22].

Stellenbosch University https://scholar.sun.ac.za

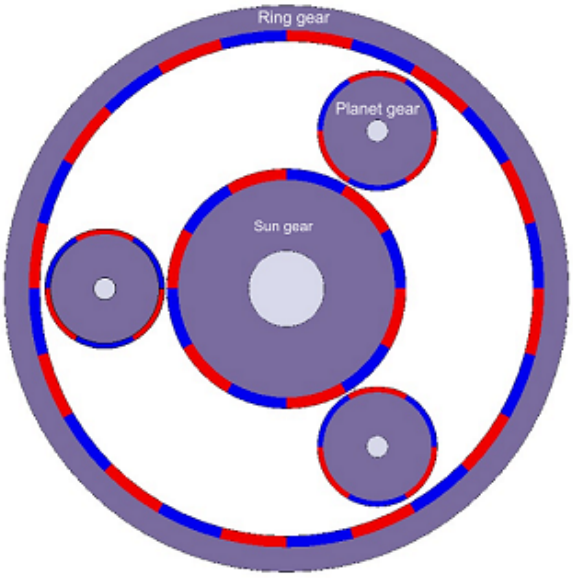

Figure 2.8: Magnet planetary gear components

2.3 Flux modulated magnetic gears

The FMMG appears to be one of the most promising MG designs. The gear consists of three major parts, i.e. an outer low-speed rotor, a flux modulator and a high-speed rotor as shown in Figure 2.9.

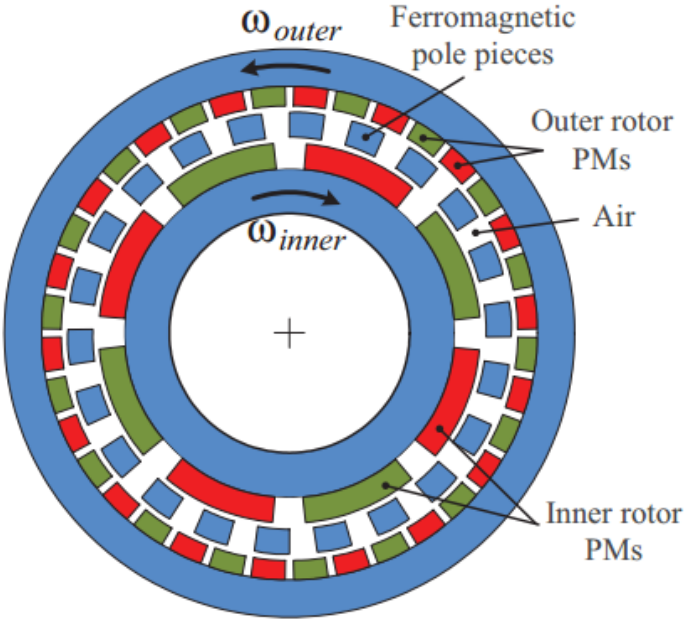

Figure 2.9: Flux modulated magnetic gear components [36]

Stellenbosch University https://scholar.sun.ac.za

The FMMG consists of two PM carrying rotors. The magnetic fields established by the two PM rotors are modulated by the magnetic pole pairs located in between these two rotors to produce working field harmonics corresponding to the pole-pairs of each PM rotor.

In most electrical machines higher order harmonics are not desirable as they may adversely affect the torque quality and overall efficiency [37, 38]. In the case of the magnetic gear, specific orders of harmonic are amplified and used to an advantage [38]. This section will attempt to explain how the characteristics of harmonics are used in magnetic gears to achieve a gear ratio between input and output shafts.

According to [38, 39], the radial magnetic field in the air-gap adjacent to the low-speed rotor of an FMMG may be expressed by Equation (2.6), where p_h is the number of PM pole pairs on the high-speed rotor, N_s the number of segments on the Modulator, Ω_r and Ω_s is the speed of the HS rotor and modulator respectively (See Appendix A for full solution):

$$B_r(r,\theta) = \sum_{m=1,3,5...} b_{rm}(r)cos(mp_h(\theta - \Omega_r t) + mp_h\theta_0) \times (\lambda_{r0}(r) + \sum_{j=1,3,5...} \lambda_{rj}(r)cos(jN_s(\theta - \Omega_s t))) \tag{2.6}$$

After some mathematical manipulation, it becomes:

$$\begin{aligned} B_r(r,\theta) = \lambda_{r0} \sum_{m=1,3,5} b_{rm}(r)cos(mp_h(\theta - \Omega_r t) + mp\theta_0) + \frac{1}{2}[\\ \sum_{m=1,3,5}\sum_{j=1,3,5} \lambda_{rj}(r)B_{rm}(r)cos((mp_h + jN_s)(\theta - \frac{jN_s\Omega_s t + mp_h\Omega_r t}{mp_h + jN_s}) + mp_h\theta_0) + \\ \sum_{m=1,3,5}\sum_{j=1,3,5} \lambda_{rj}(r)B_{rm}(r)cos((mp_h - jN_s)(\theta - \frac{mp_h\Omega_r t - jN_s\Omega_s t}{mp_h - jN_s}) + mp\theta_0)] \end{aligned} \tag{2.7}$$

In the case that the modulator is fixed, in equation (2.7), the modulator speed $\Omega_s = 0$. It can be shown that the amount of pole-pairs produced by the HS shaft or LS shaft have a space harmonic flux waveform given by [39]:

$$\begin{aligned} p_{mk} &= |mp_h + kN_s| \\ m &= 1, 3, 5, ...\infty \\ k &= 0, \pm1, \pm2, \pm3, ... \pm\infty \end{aligned} \tag{2.8}$$

Stellenbosch University https://scholar.sun.ac.za

with N_s the number of steel poles of the modulator and p_{mk} the number of magnetic poles on the space harmonic flux waveform distribution. To enable the FMMG to work, the number of pole-pairs of the LS rotor p_l should be equal to p_{mk}. The largest asynchronous space harmonic is usually realized when m = 1 and k = -1 [25] so that $p_l = N_s - p_h$. The gear ratio is thus:

$$G_r = -\frac{p_l}{p_h} \tag{2.9}$$

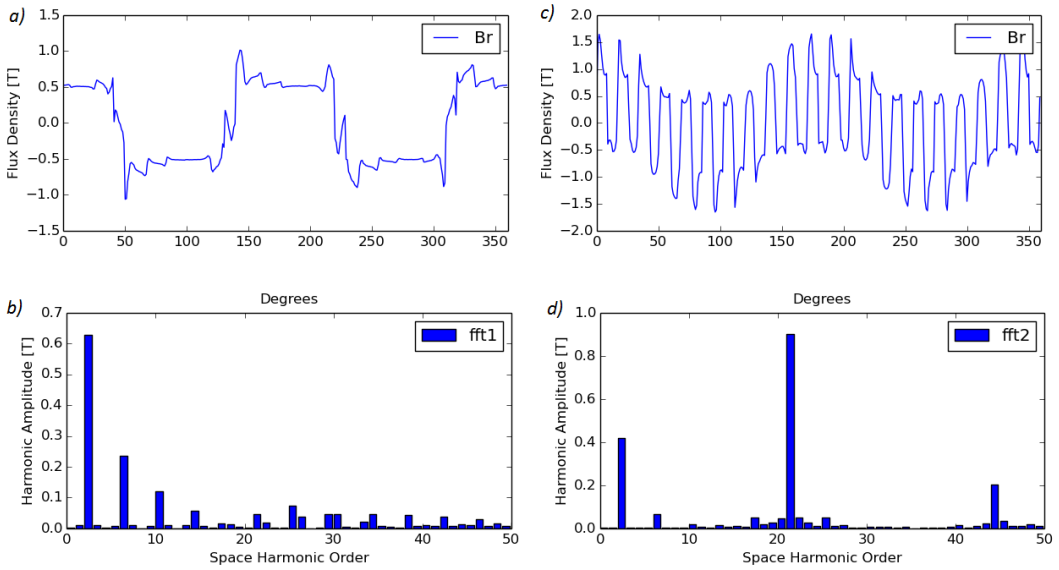

Figure 2.10: Magnetic flux distribution in the HS and LS airgaps of a magnetic gear with (a) Flux waveform in HS air-gap, (b) FFT of Flux in (a), (c) Flux waveform in LS air-gap, (d) FFT of (c)

Consider an FMMG with $p_h = 2$ and a gear ratio of $G_r = 10.5$ as an example, for the gear to function the number of PM pole pairs on the LS shaft should be 21. Figure 2.10 shows the magnetic flux density waveforms in the HS and LS air-gaps and their respective space harmonic contents. Figure 2.10 (b) and (d) clearly shows the prominent 2nd and 21st harmonics in the inner and outer air-gaps.

2.4 Comparison of MG topologies

Among the three types of MGs discussed in this chapter, both MPG and FMMG technologies are potentially suitable candidates for the application stated in Chapter 1. In this section they are further compared in order to make an informed decision for the best suited topology for the intended application.

Stellenbosch University https://scholar.sun.ac.za

2.4.1 Prototypes built for performance evaluation

To investigate the performance and practical aspects of the MG topologies under consideration, both an FMMG and an MPG prototypes have been designed, constructed and experimentally evaluated.

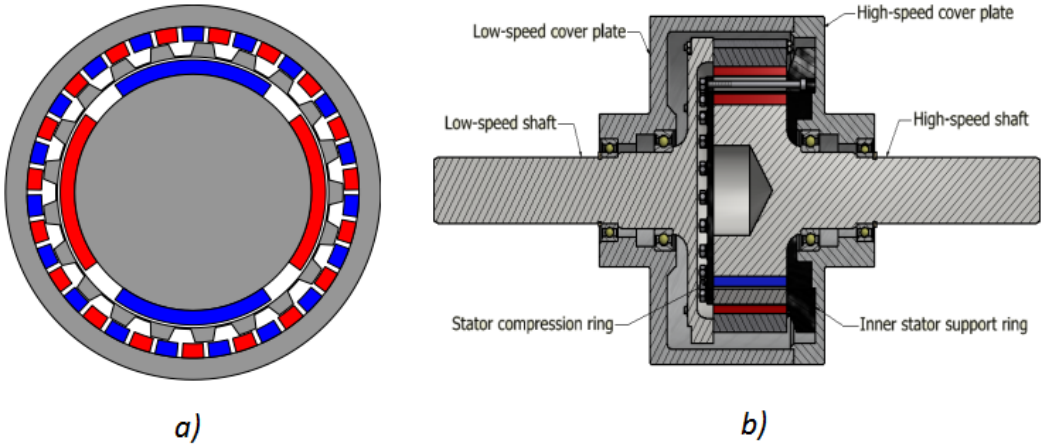

Figure 2.11: 2D view of FMMG (Left), Sectional side view of FMMG, [38]

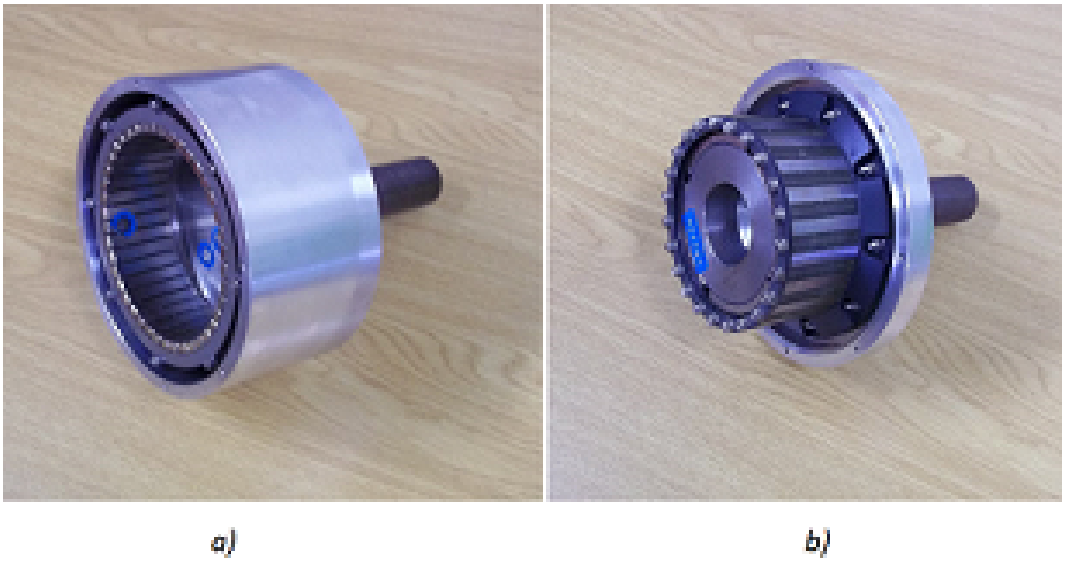

Figure 2.12: Flux modulated magnetic gear sub assemblies (a) LS sub assembly and (b) HS sub assembly with modulator

The optimized 2D FE design of an FMMG and its mechanical layout can be seen in Figure 2.11. The gear performed very well and a peak stall torque measurement of 46 Nm was achieved on the LS shaft. The full load efficiency

Stellenbosch University https://scholar.sun.ac.za

at a test speeds up to 1600 rpm was measured at 95% [38]. The volume torque density of the gear is about 87 kNm/m^3. Figure 2.12 shows the main components of the constructed FMMG prototype.

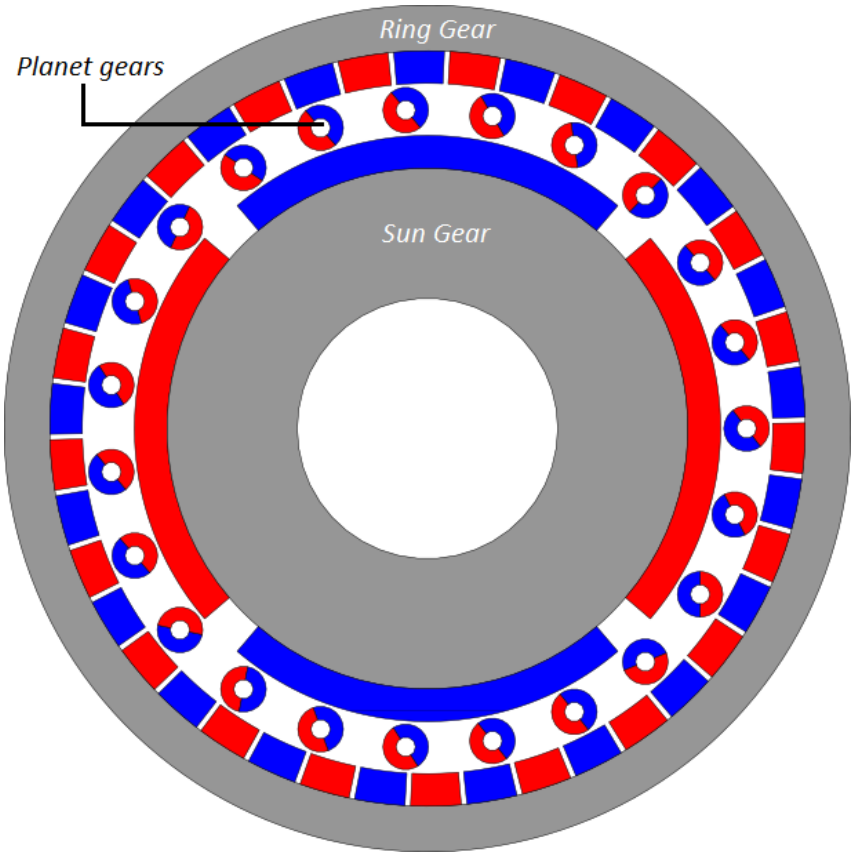

Figure 2.13: Magnet planetary gear components

As illustrated in Figure 2.13, the planetary magnetic gear prototype investigated consists of a planet carrier which is held stationary with the input shaft connected to the sun gear and output to the ring gear. The planet gears would rotate about their own axis on the stationary carrier. The planet gears rotate with a rate proportional to the ratio (z_s/z_p). The rotation of the planet gears then results in a rotation in the ring gear to a ratio of (z_p/z_r).The stationary planet carrier $(\omega_c = 0)$ will result in a gear ratio (G_r) according to $(-z_s/z_r)$ [28], with the negative sign indicating opposite directions of rotation between sun and ring gears and therefore opposite directions of rotation on the input and output shafts. for Common magnetic planetary gears as well as mechanical gears the gear ratio GR is related to Equation (2.4) but due to the flux modulating effect, gear designs such as in Figure 2.13 can be realized where the planet gears number equal $(z_r + z_s)$ [27].

Stellenbosch University https://scholar.sun.ac.za

For performance reference both FMMG and MPG prototypes are designed to have the same dimensions. The design parameters are given in Table 2.1.

Table 2.1: Design parameters of the magnetic planetary gear

Parameter	**Value**
Sun gear PM pitch [fraction of pole pitch]	0.9
Sun gear yoke inner diameter [mm]	41
Sun gear yoke thickness [mm]	18.8
Sun gear PM thickness [mm]	5
Sun gear air-gap length [mm]	0.6
Planet gear PM outer diameter [mm]	7
Planet gear inner diameter [mm]	3
Ring gear PM pitch [fraction of pole pitch]	0.897
Ring gear air-gap length [mm]	0.6
Ring gear PM thickness [mm]	5
Ring gear yoke thickness [mm]	7.5
Ring gear yoke outer diameter [mm]	130
Number of sun gear pole pairs	2
Number of ring gear pole pairs	21
Number of planet gears	23
Gear ratio	10.5
Stack length [mm]	40
Volume [m^3]	5.31×10^{-6}
Magnet material and grade	NdFeB (N35H)

Table 2.2 summarizes the torque performance of the two MG designs. The peak torque or stall torque measured from the FMMG was 46 Nm [38] whereas the measured peak torque for the MPG achieved a torque of 74 Nm during the peak stall torque test [29].

Table 2.2: Comparison of torque performance

Performance	Planetary MG	Flux modulated MG
Stall torque predicted	78.3 Nm	54.6 Nm
Stall torque measured	74 Nm	46.2 Nm
Gear's active volume	531×10^{-6} m^3	531×10^{-6} m^3
Torque density measured	139.35 kNm/m^3	87 kNm/m^3
PM material used	1.0225 kg	0.8086 kg
Torque / PM mass	72.3 Nm/kg	57.1 Nm/kg
Efficiency at full load	70%	95%

However, the MPG suffered significant mechanical losses and the efficiency was measured as about 70% at full load and speed of 1000 rpm. These losses were

Stellenbosch University https://scholar.sun.ac.za

caused by the friction between planet gears and the carrier. Using low friction bearings to support the planet magnets for instance could be a possible solution to decrease frictional losses and realize the true potential of this design [29].

However, adding bearings increases the amount of moving parts and mechanical complexity which would be an extra factor to consider in long term maintenance of the gear. The planetary gear is therefore disregarded as the ideal selection for this study. An image of the main components of the MPG is shown in Figure 2.14.

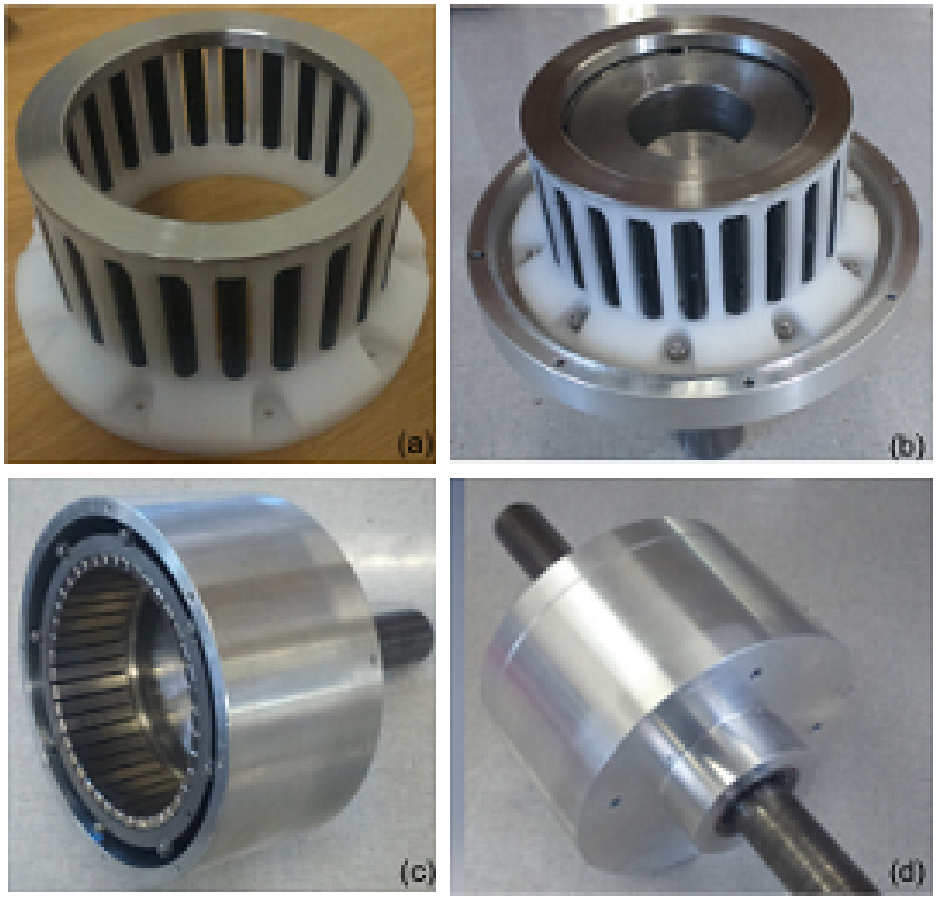

Figure 2.14: Magnet planetary gear prototype with (a) Carrier with stainless steel support ring, (b) Carrier and HS assembly, (c) LS and low speed casing assembly and (d) full gear assembly [29]

Stellenbosch University https://scholar.sun.ac.za

2.4.2 Discussion

Of the three promising magnetic gear topologies chosen for further investigation two of these designs proved to have promise for the application. The MHG proves to be an interesting topology with large effective gear ratio range, high torque density and near ripple free torque transfer [31, 32, 40]. These positive attributes considered it must be stated that mechanical complexity can be a major factor in machine life-span, manufacturing difficult and therefore expense. The fact that so little research has been published on MHGs is a clear indicator that the machine is mechanically challenging and should therefore be deemed inappropriate for this application until further research and investigation is performed in this technology.

The PMG and FMMG appear to be the most promising of the short listed MG topologies. Many publications are available on PMGs most of which reported successful results [41, 27, 30] and some which experienced difficulties due to mechanical complexity [28, 26] including the prototype manufactured in this study [29]. The PMG appears to exhibit the highest torque density but also suffered from the highest losses and therefore exhibited the lowest efficiency.

The FMMG is composed of the most manufacturable mechanical components and assembly structure, which would greatly reduce manufacturing cost and time. From a large amount of successful prototypes produced and published [25, 42, 39, 43] and from the successful results on the FMMG prototype [36]. As well as achieving a full load efficiency of 95% and torque density of $87kN/m^3$ the FMMG appears to be the most likely MG topology to select to achieve success on the large scale gear prototype. The simple design and reliability of the FMMG design evaluated are essential to the potential success of this study. From a cost stand point the FMMG also requires less PM material and would be cheaper to manufacture a larger scale model. The large scale prototype design selected for this study is therefore the FMMG.

Stellenbosch University https://scholar.sun.ac.za

Chapter 3

Design aspects of FMMGs

In this chapter various important aspects pertaining to the design of FMMGs such as gear ratio specifications, 3D end effects, loss mechanism, modulator design and PM demagnetization risk are discussed.

3.1 Relations between pole-pairs and modulation pieces

As explained in previous chapters, the relationship between the number of PM pole-pairs of HS rotor and LS rotor, p_h and p_l, and the number of segments in the modulator, N_s, and their respective angular velocity, ω_h, ω_l and ω_m, is governed by the following equation:

$$\omega_h\, p_h + \omega_l\, p_l = \omega_m\, (p_h + p_l) \tag{3.1}$$

For correct coupling of the magnetic flux waveforms the number of segments N_s should equal $p_h + p_l$. Depending on which component of an FMMG is kept stationary, two different gear ratios can be realized. In the case that the modulator is fixed, i.e. $\omega_m = 0$, the gear ratio is simply:

$$G_r = \frac{\omega_l}{\omega_h} = -\frac{p_l}{p_h} \tag{3.2}$$

where the minus sign represents that the HS and LS rotors rotate in an opposite direction. If the LS rotor is chosen to be stationary, i.e. $\omega_l = 0$, a higher gear ratio can be obtained:

$$G_r = \frac{\omega_h}{\omega_l} = \frac{p_h + p_l}{p_h} = 1 + \frac{p_l}{p_h} \tag{3.3}$$

An important consideration when designing an FMMG is the smoothness in torque transmission. If a large torque ripple is present the machine performance could suffer as well as other unwanted phenomenon like vibration, oscillation and increased noise. Similar to conventional PM electrical machines,

Stellenbosch University https://scholar.sun.ac.za

the cogging/ripple torque is caused by the interaction between the PM poles and the stator teeth (modulation pole-pieces in MGs) [44, 45]. As a design guideline, a cogging torque factor, f_c, introduced in [46] has often been used to estimate the severity of cogging/ripple torque:

$$f_c = \frac{2p\,N_s}{N_c} \tag{3.4}$$

where p is the number of pole pairs of HS or LS rotor, N_s is the number of segments in the modulator and N_c is the lowest common multiple (LCM) of $2p$ and N_s. From this equation it is clear the higher the LCM the smaller the cogging/ripple torque will be. Therefore, when choosing the number of pole-pairs and modulator segments in the gear, it is desirable to, as far as possible, choose suitable combinations that coincide with a large LCM. This usually requires gear ratios to be chosen as fractions instead of integer values. Figure 3.1 shows the torque output of an MG with a 3.5:1 gear ratio. The LCM of this gear is 28 as the $p_h = 4$ and the $N_s = 14$ and a significant torque ripple is present. The cogging factor calculated for these parameters is 4.0.

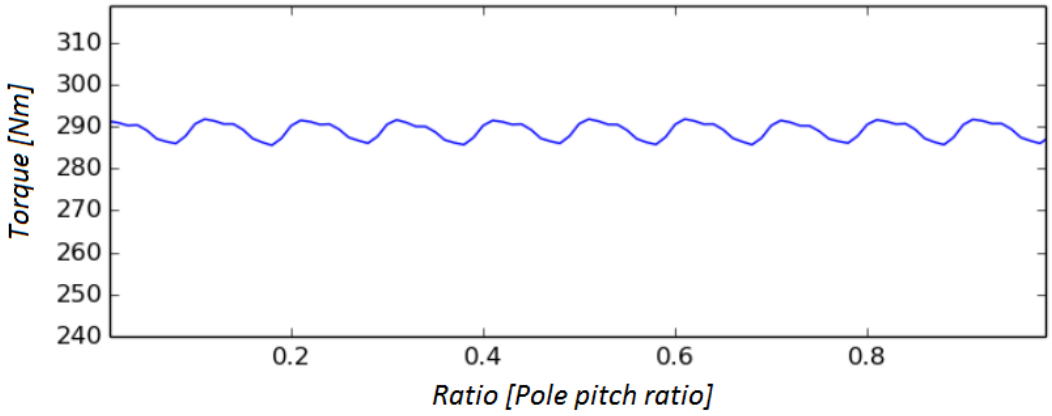

Figure 3.1: Torque output of an MG with 3.5:1 gear ratio

3.2 3D end effects and mitigation measures

End leakage flux can be defined as the magnetic flux which does not follow the intended path hence it does not effectively contribute to the intended purpose [47]. In this case between the rotors of the magnetic gear, especially at the ends of the stack length. The magnetic flux should ideally run in the radial direction and minimally if at all in the axial direction. Generally 2D simulations will yield a larger output performance result as they do not take axial flux and therefore leakage flux into consideration during FE analysis [36].

Stellenbosch University https://scholar.sun.ac.za

For this reason 3D FE simulations are required to verify 2D simulations and achieve a more realistic expectation of what practical measured values will deliver. Figure 3.2 shows a magnetic equivalent circuit of the flux and reluctance behaviour at the end of the stack of a magnetic gear.

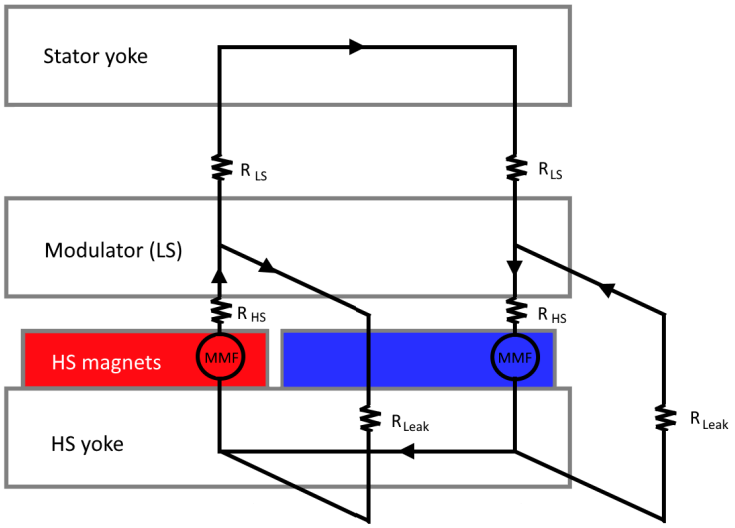

Figure 3.2: Magnetic equivalent circuit for the end leakage flux of a magnetic gear

In Figure 3.2 the R_{HS} presents the reluctance of the HS magnets and air-gap, R_{LS} the reluctance of the LS magnets and air-gap and R_{Leak} the reluctance of the leakage component [36]. Ideally the R_{Leak} components should be infinite but this is not practically possible. It is however possible to increase this R_{Leak} reluctance value by implementing techniques such as using non-magnetic material as far as is practically possible in the regions prone to the presence of end leakage flux [38]. From previous projects involving design, manufacturing and testing of MGs, such as in [38, 36, 48], it is known that the achievable peak torque is roughly 80% of the 2D simulation results. End leakage flux is largely responsible for this discrepancy. Therefore during the 2D design phase the gear should achieve an output of higher than rated torque as shown in (3.5).

$$T_{2D} = \frac{T_{rated}}{80\%} = 1.25 T_{rated} \tag{3.5}$$

This is simply a non-formal rule of thumb of what to expect for 2D FE simulations to practical results. To maintain a reasonable operating margin the maximum torque of an MG should be even higher.

Stellenbosch University https://scholar.sun.ac.za

3.3 Losses in an MG

The losses present during operation of a magnetic gear are originated from several sources. A diagram showing the most significant losses experienced in an MG is given in Figure 3.3. The mechanical losses consist of bearing losses ($P_{bearing}$) and windage losses ($P_{windage}$) while the electromagnetic losses consist of magnet losses (P_{magnet}) and core losses (including eddy current losses (P_{eddy}) and hysteresis losses ($P_{hysteresis}$)) and secondary losses ($P_{secondary}$).

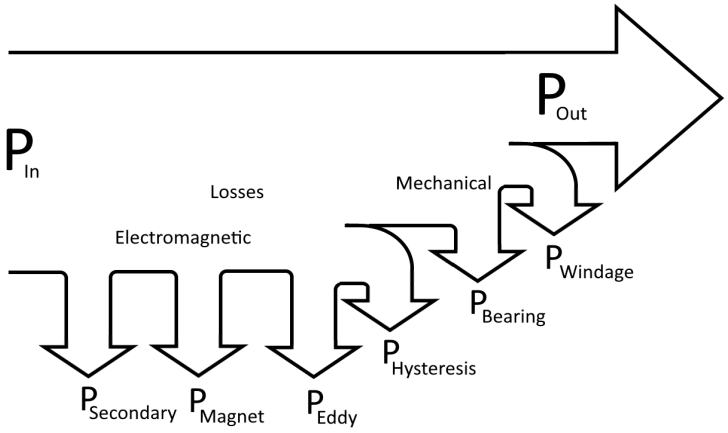

Figure 3.3: Diagram of power and losses in a magnetic gear

3.3.1 Core losses

Core losses relevant to magnetic gears consist of eddy current and hysteresis losses in the electrical conductive materials forming part of magnetic circuit.

3.3.1.1 Eddy Current losses

Eddy currents are local electrical currents induced in conductors by varying magnetic fields. The higher frequency components are responsible for the the most eddy current losses. Eddy current losses in electrical conductive materials can be reduced by a common method of lamination of the active steel components. Figure 3.4 illustrates how the eddy currents are induced in a solid conductive material and a similar volume of laminated sections of conductive material. The sum of the induced losses in the smaller eddy currents circulation in the laminations is much smaller than the losses induced in a solid conductive material freely allowing eddy currents to flow. The laminations have special coatings on both sides for electrical insulation from one another.

Stellenbosch University https://scholar.sun.ac.za

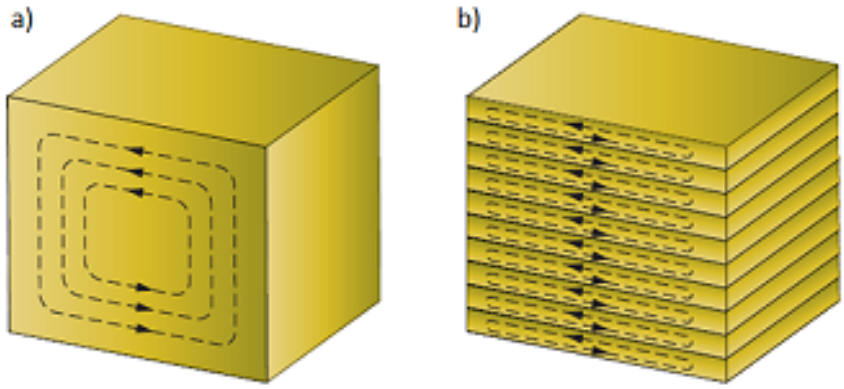

Figure 3.4: (a) Eddy current flow patterns in a solid conductor, (b) laminated conductor, [49]

As the eddy current losses increases proportionally to the square of the frequency of field variations [50]. It is important to keep the electrical frequency of a MG low [51, 50].

An accurate frequency analysis FEA approach can be used to determine the eddy current loss in electrical laminated steel [52]:

$$P_e = \sum_{e=1}^{n_{elem}} \left\{ \sum_{k=1}^{N} b(|B_k|, f_k) \times {f_k}^2 \right\} \times V_e \tag{3.6}$$

where n_{elem} is the number of elements in the mesh, f_k is the k^{th} order frequency, $b(|B_k|, f_k)$ is the coefficient of magnetic flux density $|B_k|$ determined by the frequency separation method at f_k [52], V_e is the size of each element and N is the maximum frequency order.

3.3.1.2 Hysteresis losses

Magnetic hysteresis is the lagging of magnetisation of a ferromagnetic material such as iron or steel. Variations in magnetic field penetrating such a material will attempt to align the magnetic domains in the material but the alignment process generally does not occur simultaneously with the field, but lags behind it [53]. Figure 3.5 shows a diagram of a hysteresis loop with notes on the points of coercivity and remanence.

Magnetic materials are generally classified into hard or soft magnetic materials. The difference between the two is in their behaviour in the absence of a magnetic field. A material with a high remanence magnetisation and coercive field coupled with a low magnetic permeability is classified as a hard magnetic material [55].

Stellenbosch University https://scholar.sun.ac.za

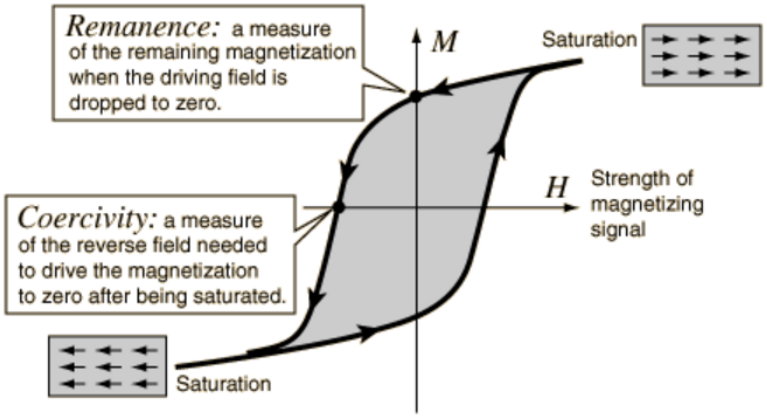

Figure 3.5: Hysteresis loop showing remanence and coercivity definitions [54]

A soft magnetic material has a low remanence magnetisation and coercive field but a much higher relative permeability. Magnets are normally characterised as hard magnetic materials and metals, such as iron, characterised as soft. Soft magnetic materials are desirable for applications which requires the material to be easily magnetised and demagnetised such as the yokes of the magnetic gears or cores of transformers [55]. Figure 3.6 shows the difference between the hysteresis loops of these two types of materials.

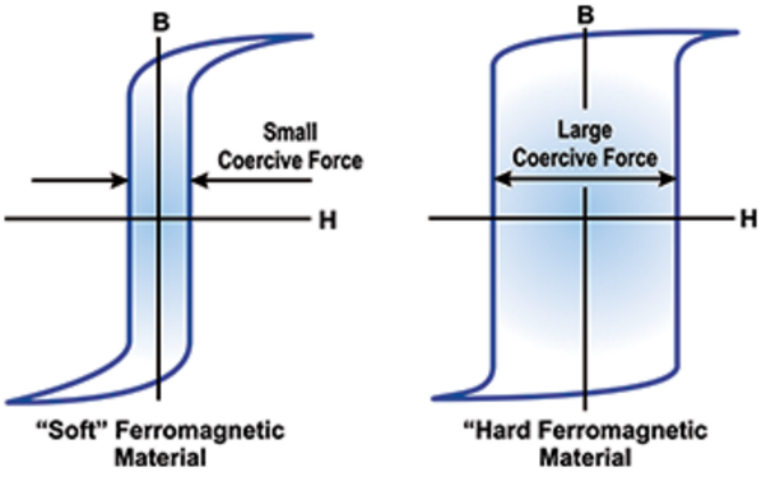

Figure 3.6: Hysteresis loop of a soft and hard magnetic material [56]

Hysteresis loss is a heat loss due to the magnetic properties of the specific material itself. The magnetic particles or domains tend to line up with the applied magnetic field and when this field keeps changing direction the continuous movement of particles as they attempt to align with the varying field vector produce molecular friction. This friction, in turn, causes heat and therefore

Stellenbosch University https://scholar.sun.ac.za

losses [57]. These losses occur with the reversal of magnet fields so the applied frequency of the varying magnetic field will of course also have an effect on these losses.

The hysteresis losses are computed by FEA applying loop approach as described in [52]:

$$P_h = \sum_{e=1}^{n_{elem}} \left\{ f \sum_{k=1}^{n_{loop}} \alpha(B_k) \times V_e \right\} \tag{3.7}$$

where f is the fundamental frequency, $\alpha(B)$ is the coefficient of magnetic flux density determined by the frequency separation method [**?**], B_k is the amplitude of the k^{th} loop for each component of magnetic flux density and n_{loop} is the number of hysteresis loops considered.

One method to mitigate hysteresis losses is to use heat-treated silicon steel laminations [57]. Once the steel is formed the laminations are heated and then allowed to cool. This annealing process aids in the reduction of hysteresis losses.

3.3.2 Mechanical losses

Although an in depth mechanical analysis is not in the scope of this study, it is important to apply sound mechanical practice for the mechanical design and construction of the magnetic gear. The most substantial mechanical power losses generated in an electrical machine generally has two components: aerodynamic loss and bearing loss [58]. The losses are attributed to moving rotors disturbing and interacting with the fluid or air in the machine and contact friction between moving parts in the case of bearings respectively.

Bearings are used to provide a low friction constrained coupled motion between two mechanical parts. A wide variety of bearing types exist. Some are more suited to certain applications than others. Bearings produce two types of losses: rolling and sliding friction, these are caused by the bearing gyroscopic pivotal motion between the balls or rollers and the rings and cage.

Due to all the complex movements of the components of the bearing under which vibration of the machine has a detrimental effect on bearing lifespan, the magnetic gear may have a potential advantage as the non-contact properties between the shafts is predicted prevent vibrations from one shaft to be transferred to the other [58, 59].

Stellenbosch University https://scholar.sun.ac.za

Another effect to keep in mind is electromagnetic losses in the bearing. The bearings are generally made of steel which is a magnetic material. If bearings are located near one of the high magnetic flux dense areas in the magnetic gear or electrical machine, eddy currents may be induced which causes heating of the bearing increasing the frictional losses and decreasing bearing lifespan [58].

The mechanical loss component caused by aerodynamic drag power is frequently referred to as windage loss. The losses due to the aerodynamic interaction with the components originate from three main causes: pressure drag, induced drag and skin friction [58]. From Figure 3.7 is is clear that the rotor speed has a significant effect on the windage losses [60].

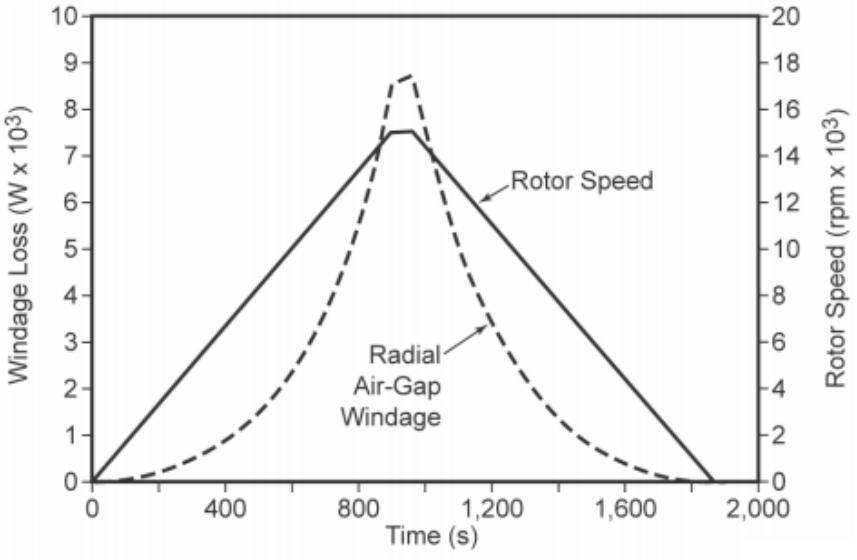

Figure 3.7: Graph of rotor speed vs windage losses [60]

3.3.3 Secondary losses

The FMMG designed and manufactured in [51] suffered from large end effect losses. The casing of this specific gear was manufactured from mild steel which has a very low magnetic reluctance. This in turn amplified the effects of the leakage flux which reduces the effective magnetic coupling between the LS and HS rotors. This leakage flux would also penetrate the mild steel casing inducing large eddy currents and therefore large losses in the gear. Losses of about 200 W were measured at a speed of 2000 rpm [51].

Figure 3.8 shows a magnetic flux density plot of the gear in [51] which was further investigated in [36]. The image in Figure 3.8 on the right shows clearly

Stellenbosch University https://scholar.sun.ac.za

where eddy currents were induced in the casing at the section supporting the modulator [36].

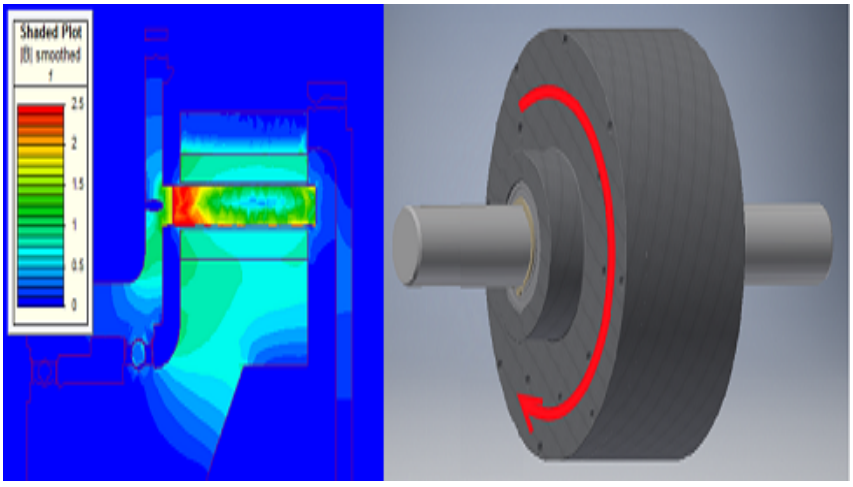

Figure 3.8: (Left)End Effects experienced in the magnetic gear, (Right) CAD drawing of MG to illustrate area effected [36]

By replacing the mild steel casing with a non-magnetic metal such aluminium the reluctance path in the affected area can be greatly increased. Non-magnetic or non-ferrous metals such as aluminium have a relative magnetic permeability close to unity [61].

3.4 Modulator design

In an FMMG, flux modulator is the key to the magnetic gearing effect. Mechanically the pole pieces on the modulator need to withstand strong magnetic forces exerted by both HS and LS PM rotors. For the ease of assembly and improved structural stiffness, inner bridges shown in Figure 3.9 are often used.

These bridges provide not only additional mechanical strength to the modulator, but also some performance benefits. As can be seen in Figure 3.10, with these bridges, the air-gap flux density waveform becomes a lot smoother. Figure 3.11 is the FFT of Figure 3.10 and clearly shows the reduction of higher order harmonics and the slight increase in the fundamental 2^{nd} order component.

To demonstrate the significance of this small design alteration the simulated ohmic losses caused by eddy currents in the HS is shown in Figure 3.12. A transient FE 2D simulation with motion was conducted at a speed of 12000 rpm [36]. There is clearly a large loss reduction, especially at higher speeds. The

Stellenbosch University https://scholar.sun.ac.za

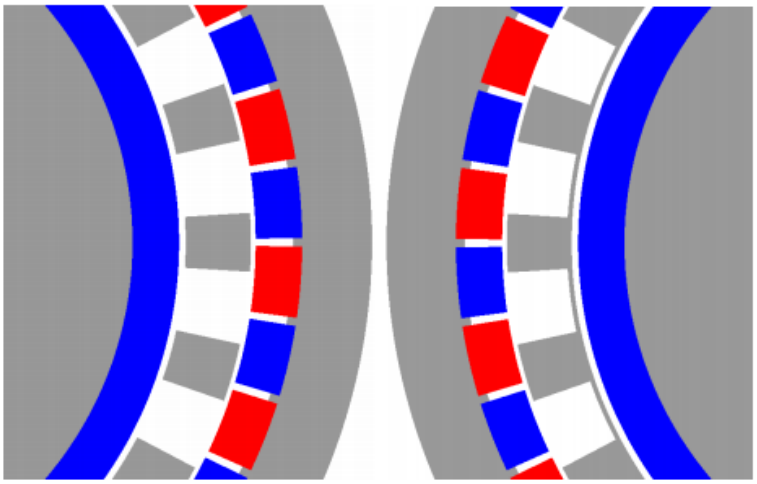

Figure 3.9: Modulator without bridges (left) with bridges (right) [36]

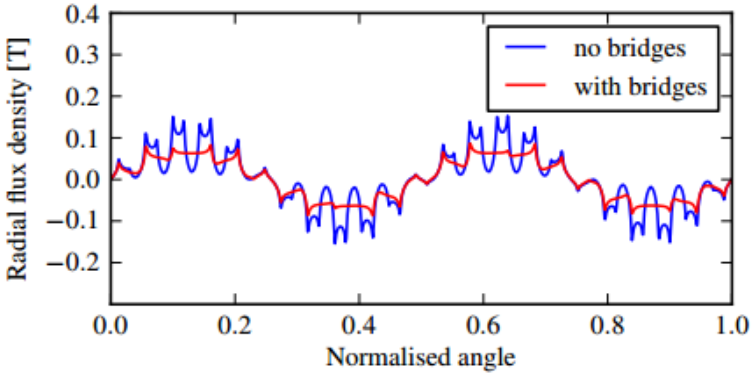

Figure 3.10: Magnetic flux waveform in the HS air-gap [36]

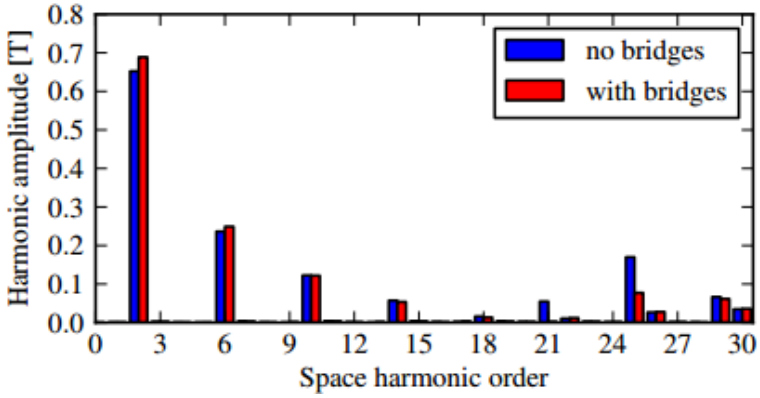

Figure 3.11: Magnetic flux waveform in the HS air-gap [36]

reduction in simulated torque on the output shaft as a result of these bridges was a mere 2.6% reduction from 53.4 Nm to 52 Nm on the LS [36].

Stellenbosch University https://scholar.sun.ac.za

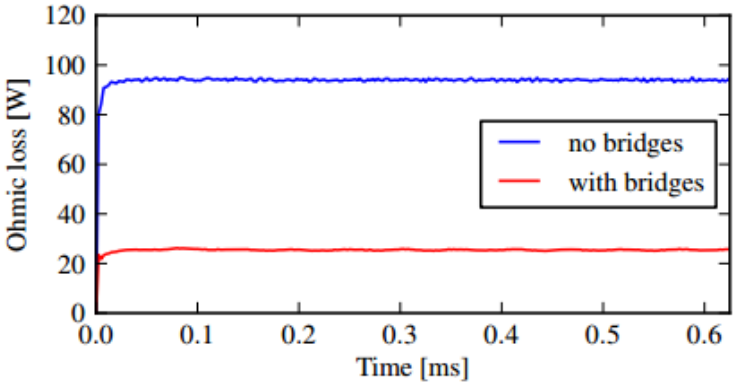

Figure 3.12: Losses in the HS magnets at a speed of 12000 rpm [36]

3.5 Demagnetization risk in PMs

When a magnet, or hard magnetic material, is first exposed to a magnetic field it's initially randomly magnetized domain moments are rotated to align with the externally applied magnetic field until saturation. Once the applied field is removed the magnetization is partially reverted to it's remanent magnetic value. A certain amount of energy is now stored in the magnet which is now referred to as a permanent magnet (PM).

This energy remains stored in the magnet indefinitely or until such point as the PM is demagnetized or heated to a point that it is demagnetize or damaged. This energy remains in the magnet as no net work is done on its surroundings. The advantage of this of course is that a PM can be used instead of a magnetized soft material or coil which would need a constant power source to maintain this field which generates heat and therefore losses [55].

Figure 3.13 (a) shows the second quadrant of a PM's demagnetization curve. The remanent magnetization B_r, the coercive field H_c values and the operating point P are characteristics of a PM [55]. A parameter to characterize a PM is the maximum energy product or BH_{max} as seen in Figure 3.13 (b). This is a measure of the energy density and is often used to classify the PM into a grade. The BH_{max} is related to the area within the hysteresis loop, and is defined as the largest rectangle that can be inscribed under the PM's Normal Curve in quadrant two. The shape and size of the hysteresis curve as well as the values of B_r, H_c as well as the temperature of the PM will affect this BH value [62]. The operating point is the intersection of the PM's load line and and the demagnetization curve. The load line is a straight line of which the slope is determined by various design parameters, of which geometry is the main factor [55]. A BH curve of an N42 grade NdFeB magnet can be seen in Figure 3.14 with two separate load lines.

Stellenbosch University https://scholar.sun.ac.za

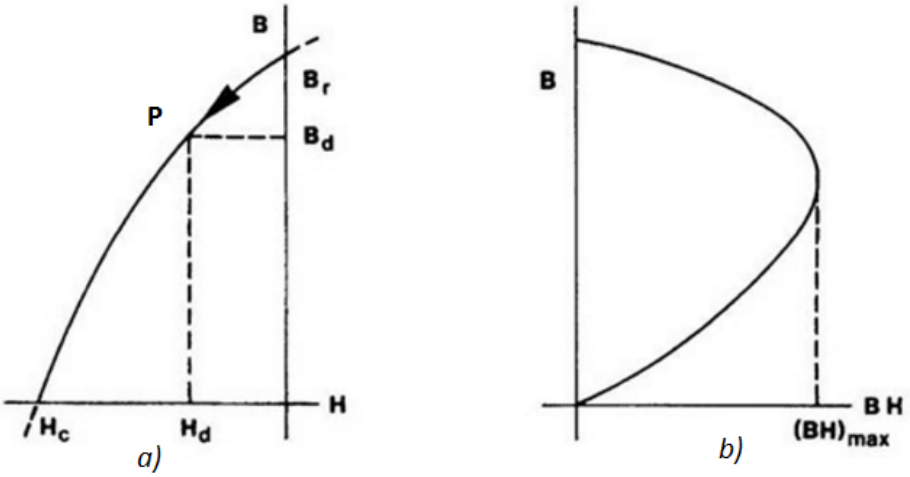

Figure 3.13: (a) Second quadrant of a magnet's demagnetization curve (b) Energy product BH as a function of B [62]

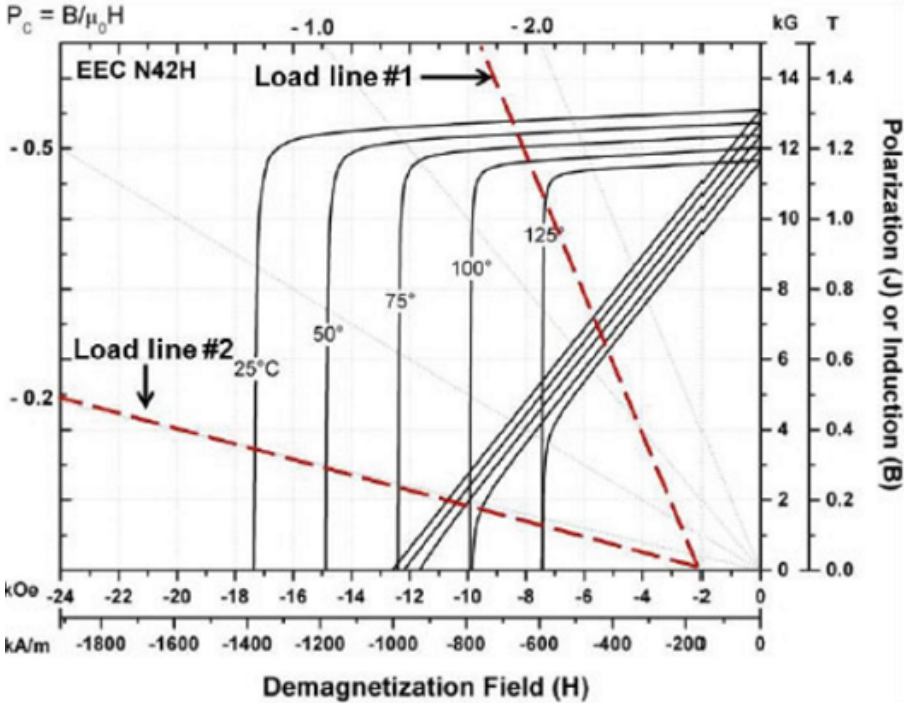

Figure 3.14: A typical demagnetization curve of N42H NdFeB magnets [63]

The demagnetization curves are seen for the same magnet at different temperatures. This N42H magnet can operate for temperatures up to 120°C with load line #1 as it intersects the curve well above the knee but the magnetic circuit for load line #2 (a different magnet) can only be used up to 75°C as the line intersects the curve close to or below the knee [63]. Residual induction magnetic flux changes in PMs with a change in temperature is a potential

Stellenbosch University https://scholar.sun.ac.za

problem that should be considered in every design. The reversible temperature coefficient or (RTC) can be considered as the change in residual induction B_r for a change in temperature of the PM material ΔT. This RTC varies for different magnet materials, [63, 64]. See Table 3.1 for some common magnet type RTCs:

Table 3.1: Permanent magnet and their RTCs [63]

Magnet type	RTC (%/°C)
Ceramic	-0.2
AlNiCo	-0.03 to 0.02
NdFeB	-0.11
SmCo5	-0.04
Sm2Co17	-0.035

As shown in Table 3.1 NdFeB magnets have one of the largest RTC coefficients. In this study, high temperatures are not a major concern although they will be investigated further later in the thesis. NdFeB magnets are not only available in different grades but are also available for different temperature rating. Figure 3.15 shows the BH_{max} degrading over temperature for H, UH, SH and EH type NdFeB PMs [63].

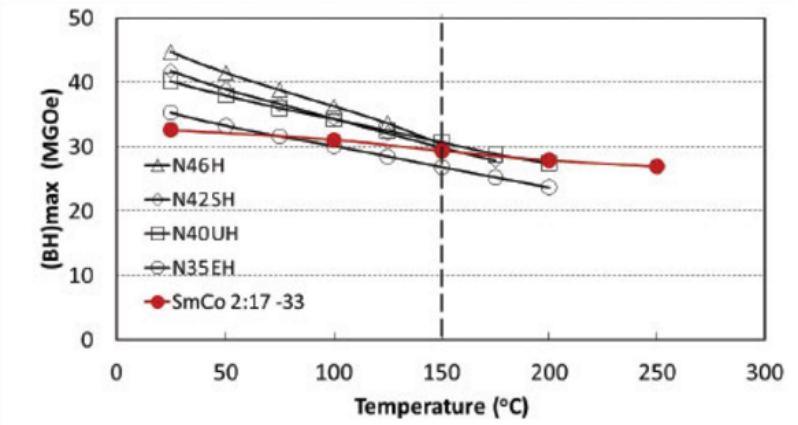

Figure 3.15: Different grades of PMs BH_{max} vs temperature [63]

As the temperature increases the risk of demagnetization increases [65]. A simulation is run with a magnetic gear design with at a PM temperature of 25°C as well as at 100°C. The grade of the PM is N48H that is specified to operate at temperatures up to 120°C.

The MG's 2D simulation output torque performance at the initial temperature was calculated at 348 Nm and due to the RTC the performance at 100°C was

Stellenbosch University https://scholar.sun.ac.za

calculated at 224 Nm. The demagnetization proximity prediction simulation results for the two cases is shown in Figure 3.16.

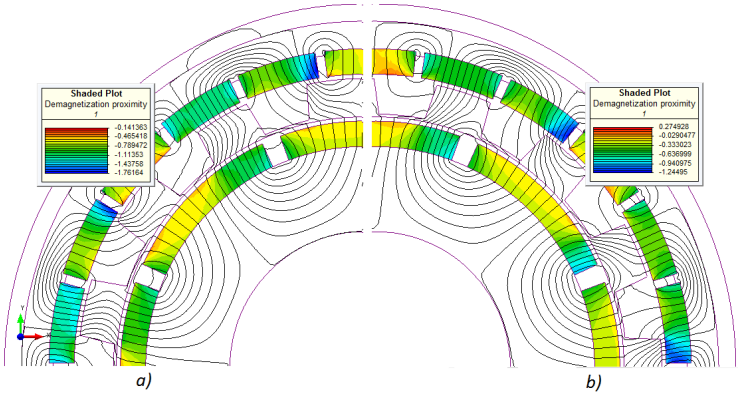

Figure 3.16: Simulated demagnetization proximity for (a) 25°C (b) 100°C

As can be seen in Figure 3.16(b) the proximity to demagnetization is much higher in the higher temperature simulation. Not only does it have a closer proximity to demagnetization levels but as seen in Figure 3.17(b) partial irreversible demagnetization on some of the inner edges of the PMs are visible. This tends to happen especially at the trailing or leading edge of the PMs as these areas are prone to high magnetic flux density. Figure 3.17(a) is the same simulation at 25°C and is predicted to free from any demagnetization effects.

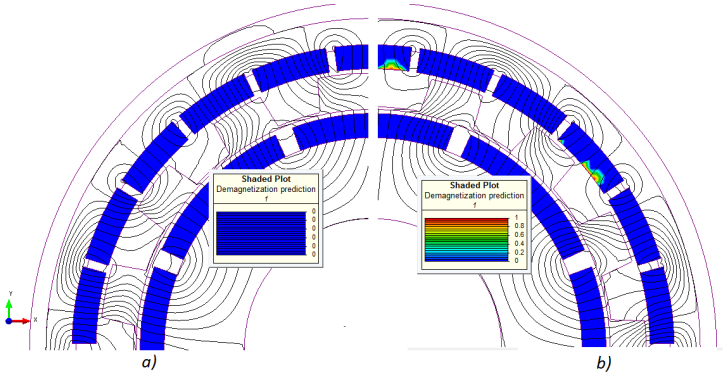

Figure 3.17: Simulated demagnetization prediction for (a) 25°C (b) 100°C

Comparing with conventional electrical machines, the demagnetization risk of an FMMG is more severe. This is because practically 50% of magnets on both PM rotors experience opposing magnetic fields at any given time. The highest risk of demagnetization in this FMMG design occurs when the MG is overloaded as explained in [66]. Care should be take to check for possible demagnetization at this point at higher temperature operations or risk causing permanent damage to the PMs.

Stellenbosch University https://scholar.sun.ac.za

Chapter 4

Design and optimization

4.1 Design specifications

The main objective of the project is to evaluate the viability of direct replacement of the mechanical gear with a magnetic gear for ACC applications. Therefore, the design specifications of the magnetic gear are determined based on a benchmark mechanical helical gear given in Table 4.1.

Table 4.1: Specifications of the mechanical helical gear

Specification	Value
Manufacturer	SEW Eurodrive
Part number	RX87 AD4
Rated torque (Nm)	132
Gear ratio	3.78:1
Service factor	2.3
Maximum torque (Nm)	305
Input speed (rpm)	600
Output speed (rpm)	158

Both gears will be tested in down-speed configuration as would be used in the field for an ACC. The magnetic gear will be designed for the same rated torque and a gear ratio that is closest to that of the mechanical gear. The maximum load torque of the mechanical gear is assumed to be 198 Nm, which equals 1.5 pu of its rated torque. To ensure that the MG will achieve this a design safety margin is added to this value. The ensure the 198Nm torque is achievable a design margin of 250Nm is chosen which must be obtained in the 3D FE simulations.

Stellenbosch University https://scholar.sun.ac.za

4.2 Design and optimization procedure

As described in Chapter 3, the gear ratio of an MG is governed by (3.3). Unlike mechanical gears, the selection of number of pole pairs and modulator pole-pieces for realizing required gear ratios could have significant influence on the MG's performance. MGs therefore are somewhat limited in the range of gear ratios that are practically achievable. In addition, the number of pole pairs should be small to keep the fundamental frequency, and therefore the electromagnetic losses low. Although both outer PM rotor and flux modulator can be used as low-speed rotor in an MG, the latter has some advantages such as improved mechanical stability, relatively simple structure and no casing needed. For this study, the flux modulator is selected as low speed rotor. The gear ratio is thus determined by:

$$G_r = \frac{\omega_h}{\omega_m} = \frac{p_m}{p_h} = \frac{p_h + p_l}{p_h} = 1 + \frac{p_l}{p_h} \tag{4.1}$$

where p_h is the number of magnet pole-pairs of high speed rotor, p_l is the number of PM pole-pairs of the outer PM carrier, p_m is the number of pole-pieces of the flux modulator, ω_h and ω_m are the rotational speeds of high speed PM rotor and modulator, respectively. To realize a gear ratio as close as practically possible to that of the mechanical gear, a few design options are summarized in Table 4.2.

Table 4.2: Design options for the MG design

p_l	p_h	p_m	G_r
5	2	7	3.5
6	2	8	4
7	3	10	3.33
8	3	11	3.67
9	3	12	4
10	4	14	3.5
11	4	15	3.75
12	4	16	4
13	5	18	3.6
14	5	19	3.8
15	6	21	3.5
16	6	22	3.67
17	6	23	3.83
18	7	25	3.57
19	7	26	3.71
20	7	27	3.86
21	8	29	3.625
22	8	30	3.75

Stellenbosch University https://scholar.sun.ac.za

The gear ratio of 3.75:1 is the closest practically achievable to the 3.78:1 ratio of the mechanical gear. Both designs with $p_h = 4$ and $p_h = 8$ can realize the same gear ratio. However, considering the frequency related core loss, $p_h = 4$ is a better design option. The gear ratio in Equation (4.1) is positive which indicates that both HS and LS rotors will rotate in the same direction.

4.2.1 2D FE design and optimization

As previously mentioned the maximum load torque of the gears is 198 Nm. In order to account for the end-effects of MGs, 3D FE modelling is preferred. However, 3D FE simulation is computationally more expensive, especially in a design optimization environment. An alternative is to employ 2D FE simulation to find an optimum design, which is then calibrated using an end-effect ratio E_T as follows [67]:

$$T_{3D} = T_{2D}\, E_T \tag{4.2}$$

where $E_T = 0.6 \sim 0.8$ dependant on quality of the design. Figure 4.1 shows the major dimensions of the mechanical gear. As the MG is designed as a possible replacement of the mechanical gear, the overall size and dimensional profile of the MG should also be relatively compatible.

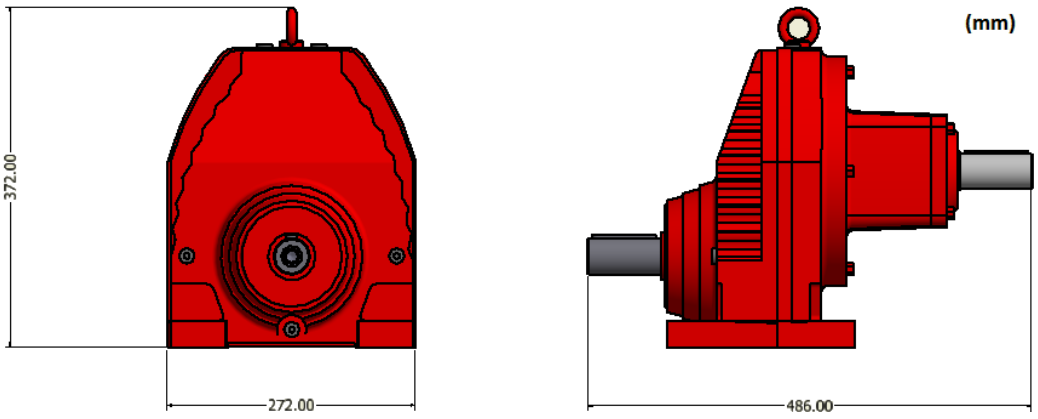

Figure 4.1: CAD drawing of the mechanical helical gear [68]

Since the aspect ratio of the MG has a strong influence on the impact of the end-effects [67], a relative long stack length of 100 mm was chosen which is manageable length considering assembly. The diameter of the gear would now have to be increased to achieve the torque requirements. Increasing the diameter of the gear has an exponential effect on the output torque while increasing the stack length has an approximate linear increase in torque. For the purpose of avoiding tight mechanical tolerances the air-gap lengths are chosen to be 1 mm. NdFeB magnets with N48H grade are used.

Stellenbosch University https://scholar.sun.ac.za

The objective function of the optimization is to maximize the stall torque of the MG per volume, which is subjected to the torque constraint:

$$\text{Objective Function} = \text{MAX}(\frac{T_{stall}}{V_{gear}}); \quad T_{stall} \geq 330\,\text{Nm} \tag{4.3}$$

with the design variables shown in Figure 4.2 and defined in Table 4.3. The initial values and ranges of each variable are given in Table 4.4. These limits are generally set to values that are practical to manufacture, i.e. if the magnets are too thin or thick, they may break or would be too expensive to manufacture. Similarly the yokes and shafts would need to be of sufficient thickness to withstand the large amount of torque of the MG.

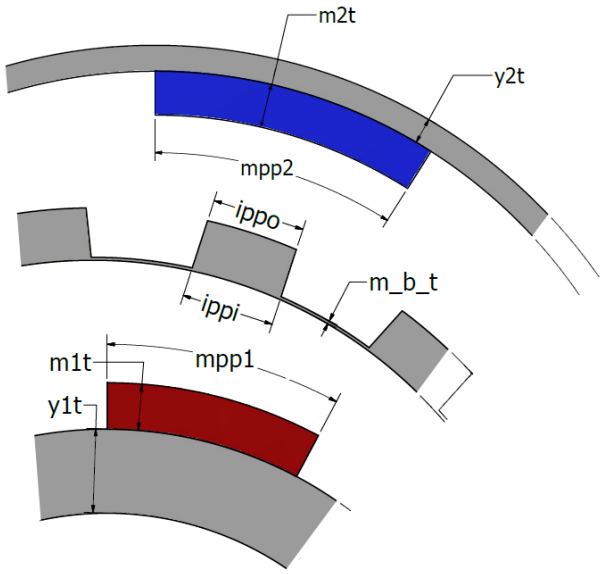

Figure 4.2: Design variables of the MG

Table 4.3: Definition of design variables for the MG

Variable	Description
mpp1	HS magnet ratio of total area
mpp2	Stator magnet ratio of total area
ippi	Modulator tooth inner thickness (ratio of pole)
ippo	Modulator tooth outer thickness (ratio of pole)
m1t	HS magnet thickness
y1t	HS yoke thickness
m_b_t	Modulator bridge thickness
m2t	Stator magnet thickness
y2t	Stator yoke thickness

Stellenbosch University https://scholar.sun.ac.za

Table 4.4: Design variables for MG

Variable	Unit	Low boundary	Up boundary	Initial value
mpp1	-	0.8	0.9	0.85
mpp2	-	0.8	0.9	0.85
ippi	-	0.2	0.8	0.5
ippo	-	0.2	0.8	0.5
m1t	mm	3.0	6.0	5.0
y1t	mm	3.0	30	5.0
m_b_t	mm	0.1	1.0	0.5
m2t	mm	3.0	6.0	5.0
y2t	mm	3.0	10.0	5.0

The performance calculation of MG is performed using SEMFEM, an in-house FEM electromagnetic package. For the optimization, the Modified Method Of Feasible Direction (MMFD) algorithm from VisualDoc software suite is employed. VisualDoc communicates these variables to SEMFEM by writing values to a file, which is in turn read by the SEMFEM python script for every iteration of the optimization process. Figure 4.3 shows a flowchart of the optimization process.

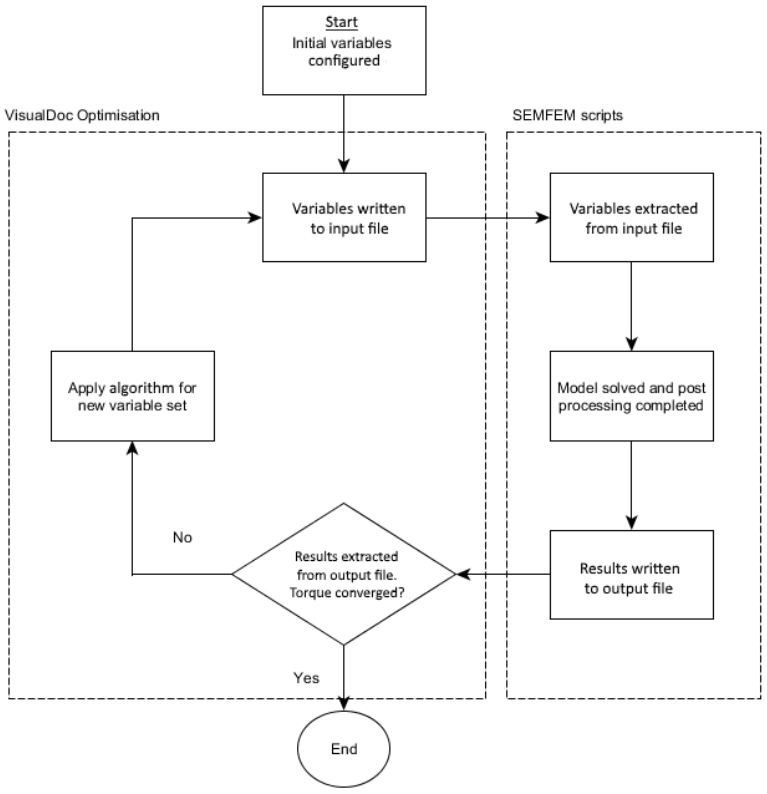

Figure 4.3: Optimization process flow chart

Stellenbosch University https://scholar.sun.ac.za

The values of variables as a function of optimization iterations are displayed in Figures 4.4 and 4.5.

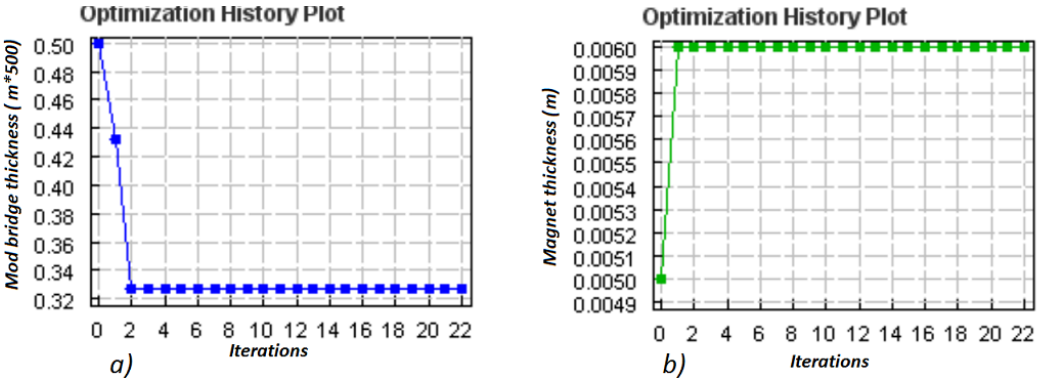

Figure 4.4: Plot of (a) modulator bridge thickness (scaled by 500), (b) HS rotor and PM carrier magnet thickness

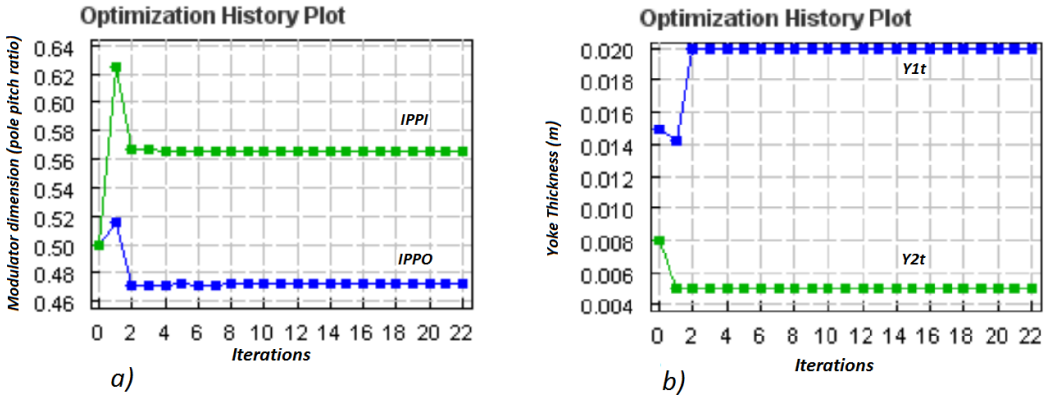

Figure 4.5: Plot of (a) Modulator tooth width, (b) HS and PM carrier yoke thickness

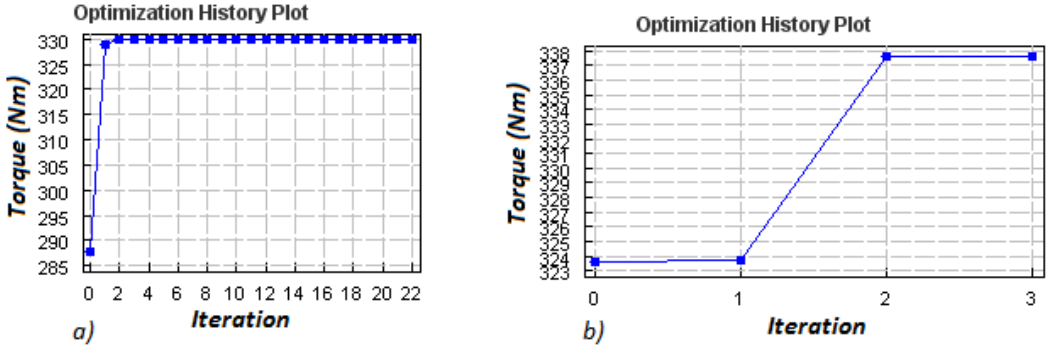

Figure 4.6: Plot of (a) Initial run with large step size, (b) Final run with fine step size

Stellenbosch University https://scholar.sun.ac.za

It is important to check the optimization values to make certain they are indeed global maximum values as an optimization can at time converge to a local maximum [29]. Different initial values would need to be tested to ensure that the optimal value has truly been reached. Figure 4.6(a) is the result of the initial optimization with a large step size while Figure 4.6(b) illustrates the final optimization run taking the previous values as initial values with a few changes to confirm no local maximum points were converged to. As the design is near optimum the software converges after only a few iterations. The torque output value of 337 Nm is deemed as an acceptable value. The optimization results are summarized in Table 4.5.

Table 4.5: Optimized design parameters of the magnetic gear

Parameter	Value
HS number of pole pairs	4
LS number of steel segments	15
PM carrier number of pole pairs	11
Gear outer radius [mm]	81.5
PM carrier yoke thickness [mm]	5.5
PM carrier magnet thickness [mm]	6
Modulator (LS) thickness [mm]	9
HS magnet thickness [mm]	6
HS yoke thickness [mm]	20
Modulator segment inner thickness [ratio of pole pitch]	0.57
Modulator segment outer thickness [ratio of pole pitch]	0.46
Modulator bridge thickness [mm]	0.65
Outer air-gap width [mm]	1.0
Inner air-gap width [mm]	1.0
Magnet grade	N48H
PM carrier magnets volume [ratio of area]	0.90
HS magnets volume [ratio of area]	0.90
Gear ratio	3.75:1
LS torque (2D results) [Nm]	337
HS torque (2D results) [Nm]	89
LS Rated speed [rpm]	160
HS Rated speed [rpm]	600
Stack length [mm]	100

In Figure 4.7 the optimized modulator segments can be seen with a inner and outer tooth thickness of 0.57 and 0.46 ratio of pole pitch respectively. The PM carrier yoke thickness seen in Figure 4.8 reached an optimal value of 6.5 mm with the inner spacers included for magnet spacing to ease the

Stellenbosch University https://scholar.sun.ac.za

assembly process. Provisions are also made in the outer section of the yoke for the threaded stainless rods to compress and support the PM carrier yoke.

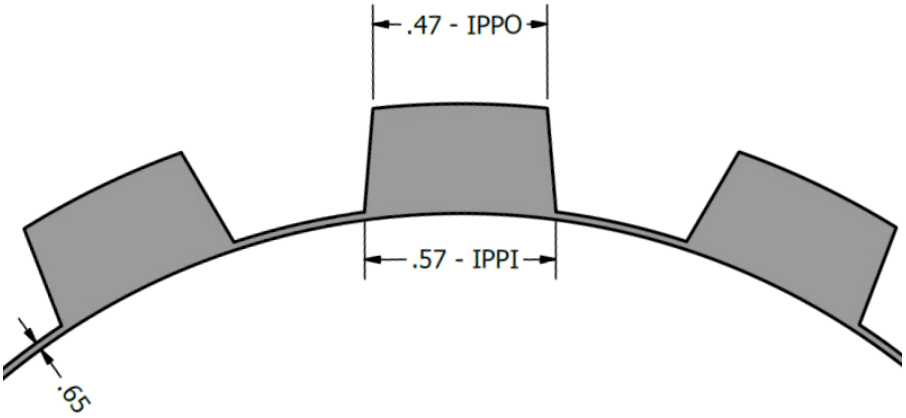

Figure 4.7: Drawing and dimensions of modulator segments and bridge

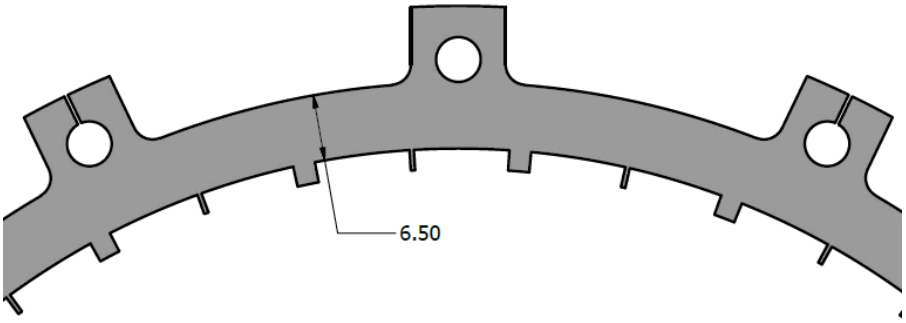

Figure 4.8: Drawing and dimensions of PM carrier yoke showing spacers used for magnet positioning

To verify the design harmonics, the magnetic flux waveforms and their space harmonic distributions in the HS and LS air gap are plotted in Figures 4.9 and 4.10, respectively. The FFTs clearly show the dominant 4^{th} and 11^{th} harmonic components as expected. The 4^{th} harmonic order is diminished by the modulator in the LS air gap similarly to the 11^{th} harmonic order component in the HS air gap. This serves as proof of a strong magnetic coupling between the active components.

Stellenbosch University https://scholar.sun.ac.za

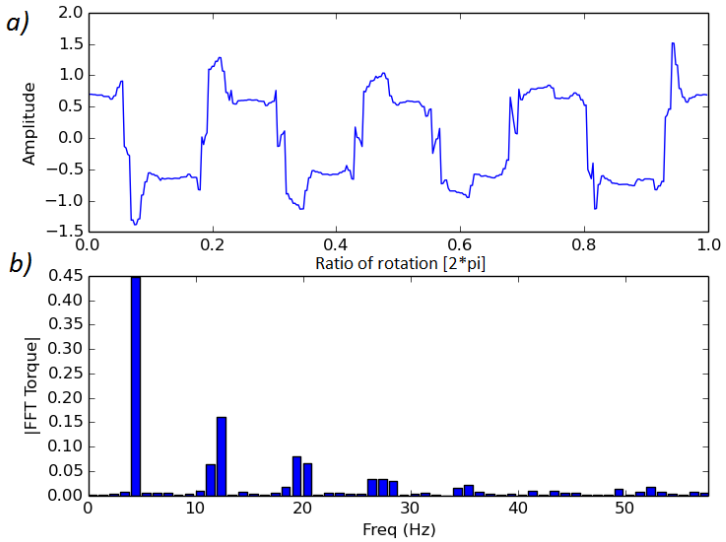

Figure 4.9: Magnetic flux density distribution in the HS airgap with (a) Radial flux (b) FFT of flux in (a)

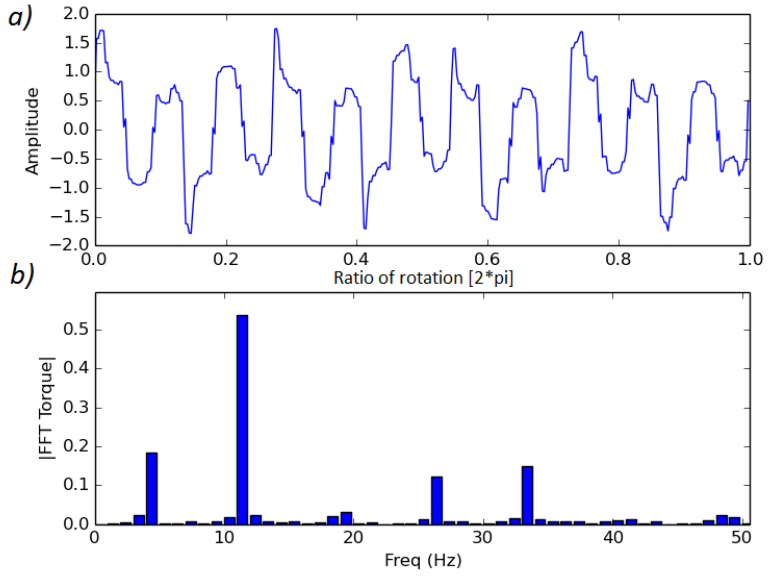

Figure 4.10: Magnetic flux density distribution in the LS airgap with (a) Radial flux (b) FFT of flux in (a)

Figure 4.11 shows the optimized 2D FE model of the MG. The four magnetic pole pairs can be seen on the inner high-speed rotor, with the red magnets representing North polarity and blue representing South. The outer PM carrier has 11 magnetic pole pairs and the modulator consists of 15 steel segments. The bridges connecting the steel segments can also be seen in this image as well as the yokes of the outer PM carrier and high-speed rotor of which the mag-

Stellenbosch University https://scholar.sun.ac.za

nets are slightly embedded. Embedding the magnets into the yokes reduces performance slightly but allows the magnets to be assembled and aligned with more accuracy.

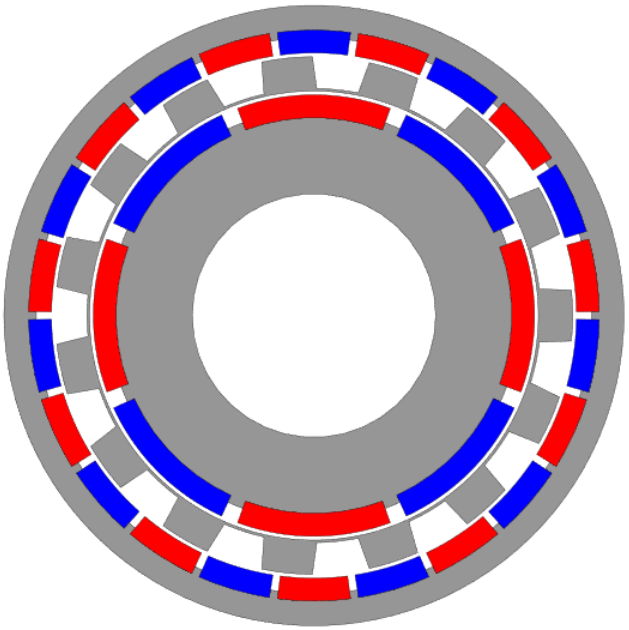

Figure 4.11: Image of magnetic gear after optimization

Figure 4.11 shows the basic design which will be further refined in the following sections to reduce losses as well as ensure mechanical stability.

4.2.2 3D FE design verification

MagNet 7 of Infolytica was used for the 3D FE simulation to verify the 2D FE results. Due to magnetic symmetry on the Z-axis only a half stack length needs to be included in 3D model, which helps to reduce simulation time. Figure 4.12 shows a sectional flux arrow and shaded plot of the 3D gear half model.

The calculated stall torque of the MG from 3D FE simulation is 281 Nm as seen in Table 4.6, which is 23.8% less than that of the 2D results. As the 3D FE simulation takes into account axial leakage flux the result is far closer to what is to be expected in the practical measurements.

Table 4.6: Computed stall torque of the MG by 2D and 3D FE simulations

Simulation model	Stall torque [Nm]	Variation [%]
2D FEM	337	-
3D FEM	281	23.8%

Stellenbosch University https://scholar.sun.ac.za

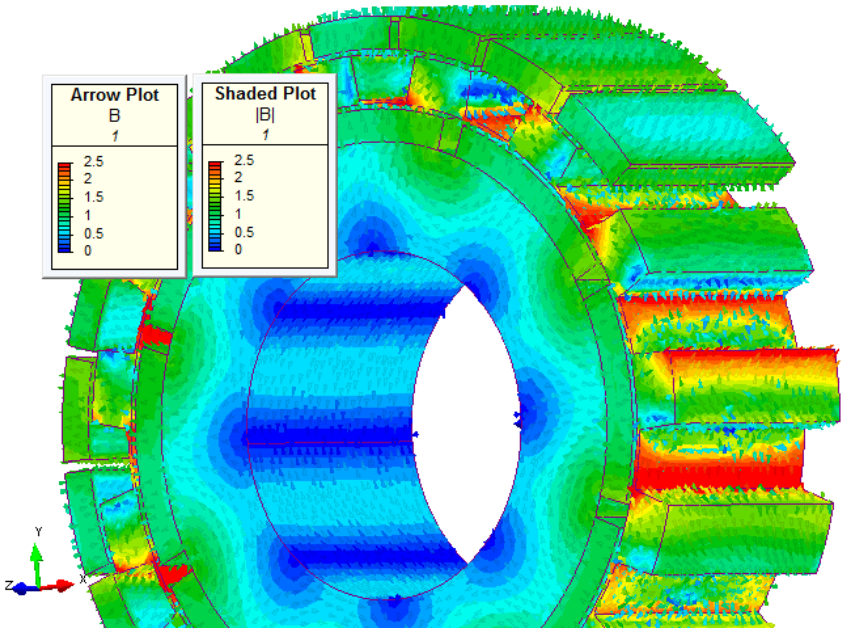

Figure 4.12: 3D simulation output with arrow and shaded plot of the magnetic field strength in the MG

4.3 Design refinement

4.3.1 Loss calculation

To evaluate the electromagnetic losses of the MG transient 2D FE motion solver of MagNet 7 was used to compute both hysteresis and eddy current losses of the MG at steady-state. Since the modulator (as low-speed rotor) rotates 3.75 times slower than the high-speed rotor, two motion components with respective rotation speed must be defined in 2D FE model.

The simulation is run over 20 ms with time steps of 0.1 ms. As the losses appear to stabilize very quickly and longer simulation time is not deemed necessary. Running the current design in a 2D FE motion simulation with the HS rotor rotating at 600 rpm and the LS rotor rotating at 160 rpm produces ohmic losses in the HS and PM carrier magnets as shown in Figure 4.13. The losses caused by eddy currents and hysteresis in the HS yoke, modulator and PM carrier can be seen Table 4.7.

Table 4.7: Core losses in the yokes

Component	Eddy current losses [W]	Hysteresis losses [W]
HS yoke	3.48	0.01
LS (Modulator)	4.8	0.556
PM carrier yoke	2.14	0.183

Stellenbosch University https://scholar.sun.ac.za

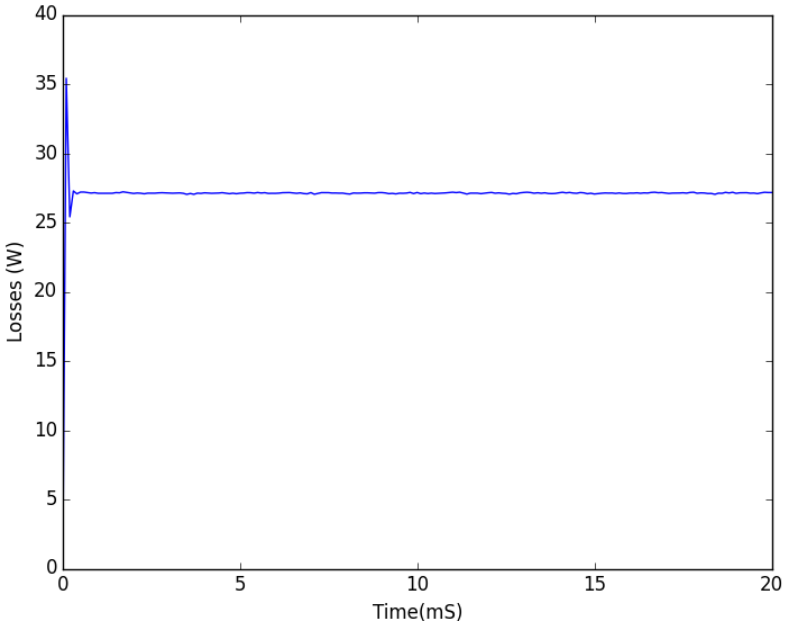

Figure 4.13: Ohmic losses in the PMs in 20 ms motion simulation

For interest sake the simulated eddy current losses in each component in case of solid steel yokes as well as laminated steel are compared in Table 4.8. It is clear the laminations are essential to MG performance especially in the modulator and PM carrier. The laminations reduce losses in the PM carrier yoke and modulator by 99.51% and 99.66% respectively.

Table 4.8: Core losses in gear components for solid and laminated yokes

Component	Losses (solid core) [W]	Losses (laminated core) [W]
HS yoke	3.49	0.11
PM carrier yoke	440.3	2.32
LS (Modulator)	1425	5.356

The HS yoke experiences only slight flux variations with frequency and therefore does not suffer from large eddy current losses. To simplify machine construction and reduce manufacturing costs the HS yoke is manufactured from solid steel. To address the losses in the PMs segmentation is implemented into the design. Magnets on both the HS and PM carrier are divided into two equal sized sections with a slight gap in between. As the magnetic poles are now divided into two and will therefore have two repelling poles placed adjacent to one another assemble is somewhat complicated. The steel segments between the magnets allow proper spacing to be maintained between the magnetic poles. Figure 4.14 shows the difference between non-segmented (a) and segmented (b) PMs in the gear.

Stellenbosch University https://scholar.sun.ac.za

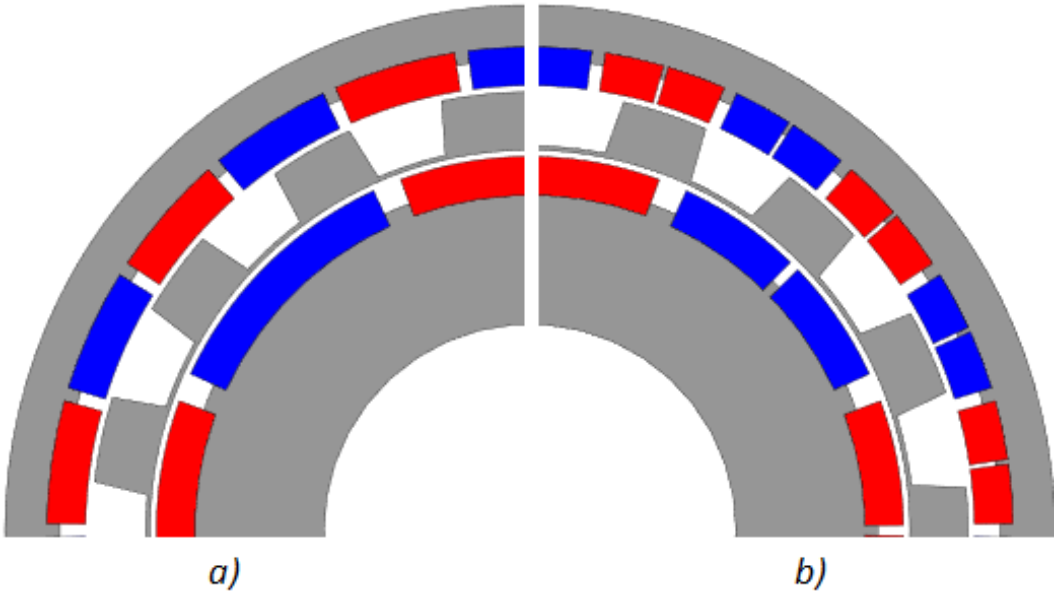

Figure 4.14: Magnet poles in (a) the original MG design, (b) modified MG design with segmented magnets

Figure 4.15 clearly shows the effectiveness of segmentation of magnets in mitigating the ohmic losses in PMs. The losses are effectively reduced from 27 W by about 50% to 13.44 W.

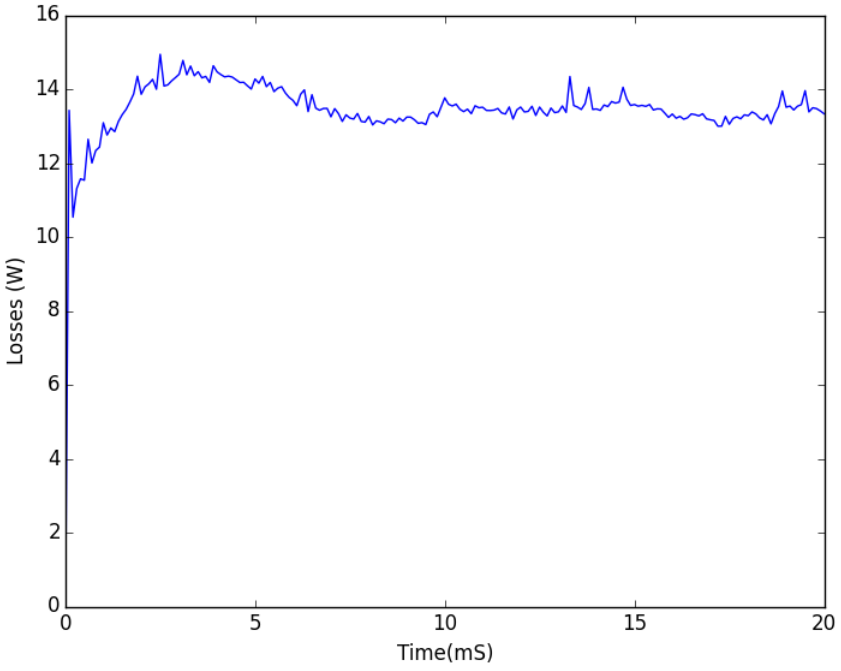

Figure 4.15: Eddy current losses in the magnets for segmented magnets

Stellenbosch University https://scholar.sun.ac.za

The modulator bridges are included thus far in the design. Table 4.9 shows the effects of magnet segmentation and modulator bridges to the MG performance. It can be observed that (i) the modulator bridges cause a small reduction in magnet losses as well as stall torque, (ii) magnet segmentation reduces the magnet losses and the stall torque of the MG by 50% and 15%, respectively.

Table 4.9: Losses for segmented vs non-segmented magnets

Configuration	Magnet losses [W]	Stall torque [Nm]
Non-Segmented with no bridge	30.9	360.8
Non-segmented with bridges	27.02	346.25
Segmented with bridges	13.44	294

It is possible to divide the magnets into more segments but the decrease in torque would be more severe. For this MG design, segmenting the magnetic poles into two sections has been deemed to be sufficient.

4.3.2 Demagnetization check

As described previously, NdFeB magnets are sensitive to high temperatures and the risk of demagnetization increases at high working temperature [69]. In addition, the MG's performance also decreases with an increase in PM temperature. Reducing the losses in the magnets is especially vital as this may effect the performance and lifetime of the machine. The predicted stall torque of the MG design is 294 Nm which is above the required 250 Nm torque threshold. However, this calculation was based on 25°C. Considering that the losses in the gear are not negligible the performance of the gear should be checked at higher temperatures.

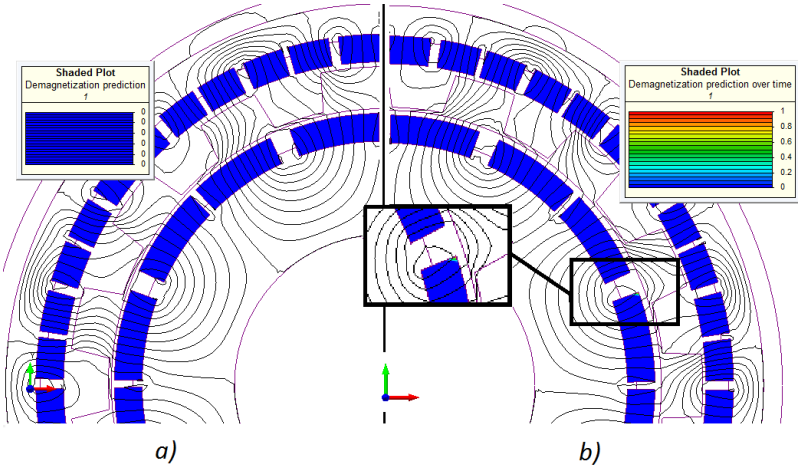

Figure 4.16: Demagnetization prediction plot of the MG at (a) 25°C and (b) 75°C

Stellenbosch University https://scholar.sun.ac.za

The demagnetization analysis of the MG was conducted at 25°C and 75°C respectively. The simulation predicts no demagnetization in the gear at 25°C as shown in Figure 4.16(a) even when the gear is at it's maximum load angle and the probability of demagnetization is at a maximum. The gear experiences some demagnetization at higher temperatures at the trailing edge [70, 71] of the PM carrier magnets as seen in Figure 4.16(b). The general level of demagnetization can be seen in Figure 4.17.

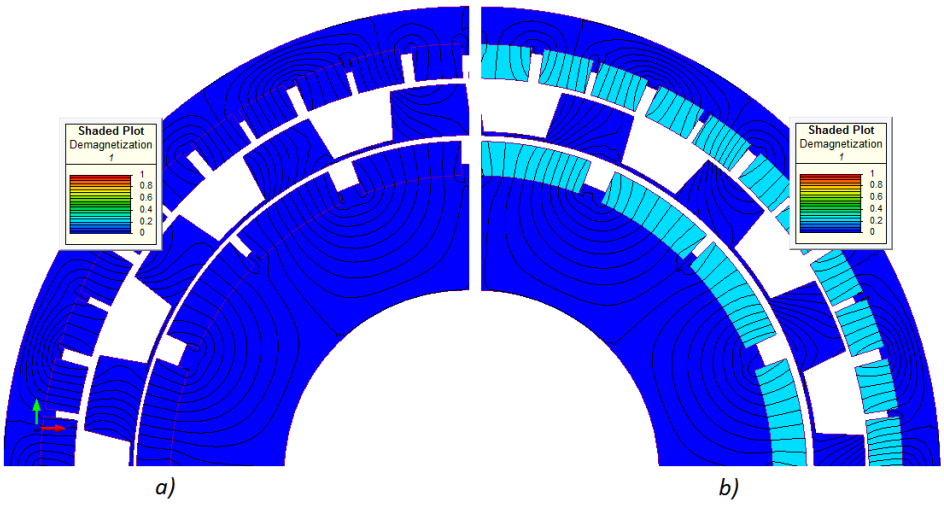

Figure 4.17: Demagnetization plot of the MG at (a) 25°C and (b) 75°C

The ohmic losses appear to be be more concentrated in the corners of the magnets as seen in Figure 4.18. One possible solution is to remove the corners of the magnets as shown in Figure 4.19.

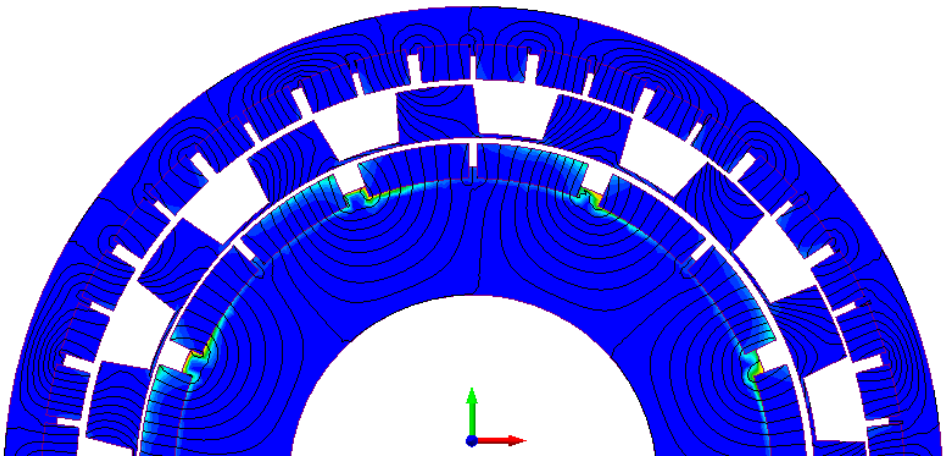

Figure 4.18: Time averaged ohmic loss plot

Stellenbosch University https://scholar.sun.ac.za

Removing the corner sections of the magnets has a slight impact on the torque performance of the gear. The torque output is reduced to approximately 281 Nm. But with the a highly concentrated section of ohmic losses removed the losses in the PM have now been reduced to 8.0 W from 13.44 W. In this case, the total losses in the gear are found to be 20.76 W as shown in Table 4.10, which excludes any mechanical losses.

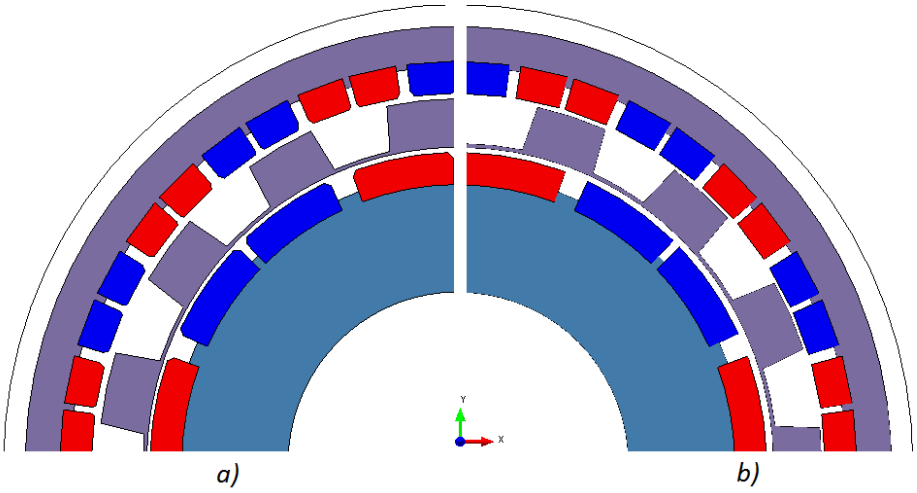

Figure 4.19: Gear design with (a) corners of magnets removed, (b) with unshaped PMs

Table 4.10: Calculated core loss components in the MG design with shaped PMs

Loss in component	Loss [W]
PMs (ohmic)	8.0
Laminated yokes (eddy current)	12.41
Laminated yokes (hysteresis)	0.354
Total	20.76

Figure 4.20 illustrates how the gear performance decreases with increase in PM temperature. It can be seen that the stall torque of the MG decreases from 281 Nm at 25°C to 229 Nm at 75°C. To ensure the MG to meet with the required torque specification, the gear's internal temperature should not be more than 60°C.

Stellenbosch University https://scholar.sun.ac.za

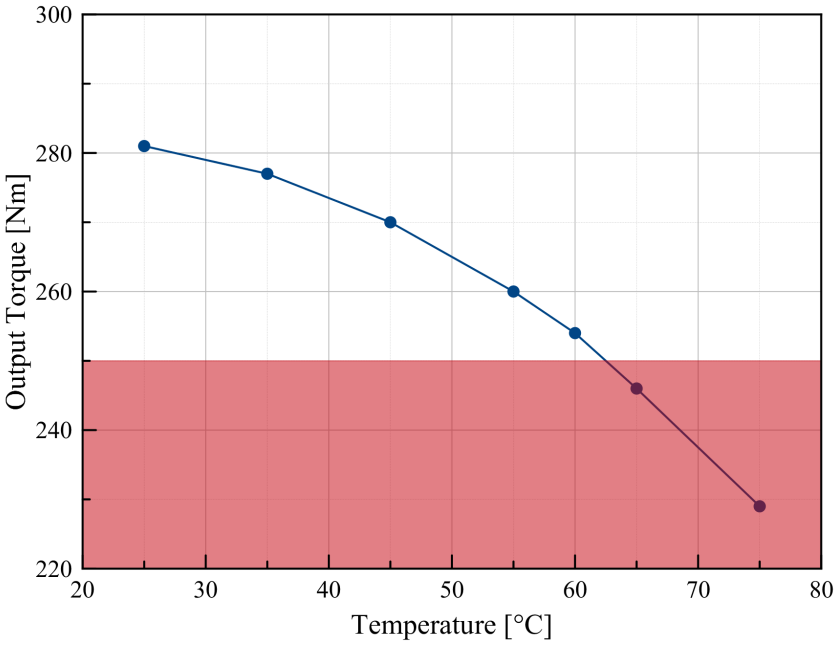

Figure 4.20: Graph indicating the simulated output torque vs gear internal temperature

4.3.3 Torque quality

With the chosen magnetic pole pairs and steel modulator segments shown in Table 4.2 the cogging factor of the MG design can be calculated as:

$$f_c = \frac{2p_h N_s}{\text{LCM}(2p_h, N_s)} = \frac{2p_l N_s}{\text{LCM}(2p_l, N_s)} = 1 \tag{4.4}$$

which indicates that relatively smooth torque profile can be realized. Figure 4.21 displays the output torque profile of the MG design, which is of much better torque quality compared to the graph shown in Figure 3.1.

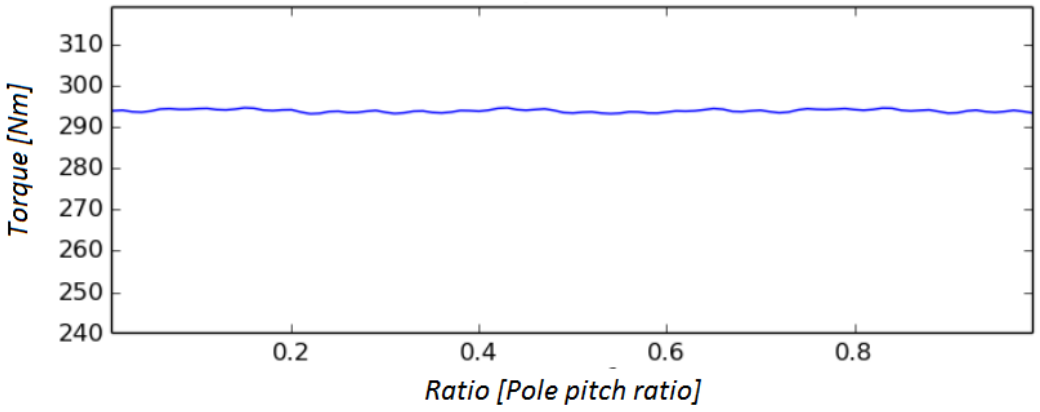

Figure 4.21: The output torque as a function of rotor position of the MG

Stellenbosch University https://scholar.sun.ac.za

4.3.4 Leakage flux

In Figure 4.22 the Aluminium end casing is incorporated into the 3D FE model. As expected some leakage flux component exists which may induce eddy currents in the casing although the amplitude of the leakage flux density is as low as 0.02 T. Possible ways of limiting these eddy current losses include increasing the space between the active stack and the end casing or making holes/slots in the end casing.

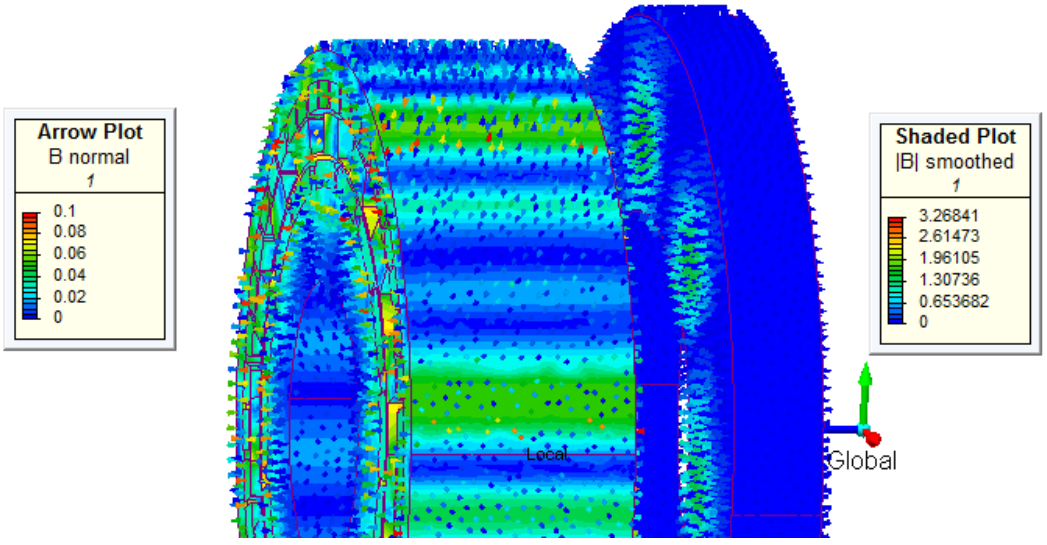

Figure 4.22: 3D simulation output with arrow and shaded plot of the magnetic field strength in the MG

4.3.5 Final 3D FE result check

Changes implemented during the design refinement phase may have negatively effected stall torque output, although decreasing the potential losses. An updated 3D simulation is run which achieves an output of 254Nm. Table 4.11 summarises the final design predicted MG performance.

Table 4.11: Results of final 2D and 3D FE output torque simulations

Simulation model	Output torque[Nm]	Variation [%]
2D	281	-
3D	254	10.6%

Stellenbosch University https://scholar.sun.ac.za

4.4 Mechanical design

This section includes the steps involved in the mechanical design aspects of an FMMG. Manufacturing cost, complexity and mechanical stress on components are also considered. Figure 4.23 shows CAD drawings of the mechanical benchmark gear and the designed FMMG.

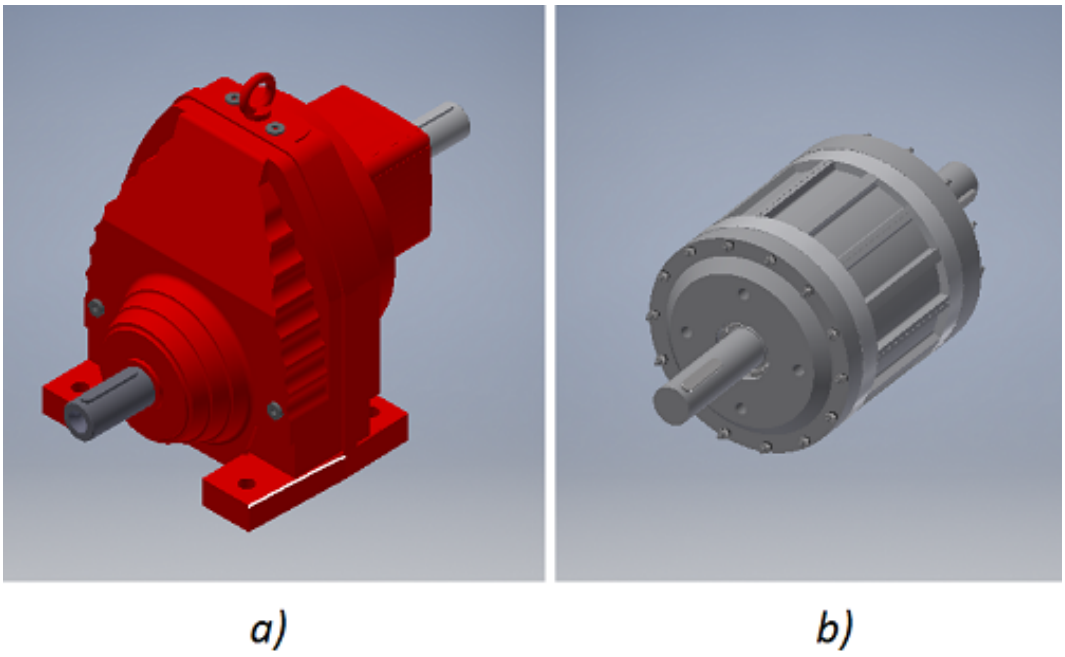

Figure 4.23: (a) SEW commercial mechanical gear (b) Designed magnetic gear

Although the mechanical gear has a power rating of approximately 5 kW the gear will not be tested at maximum speed but instead at rated torque. The gear has a rated torque of 132 Nm as seen in Table 4.1. The maximum permissible torque on the gear (M_a) is 305 Nm before possible damage to the gear. This includes spikes in load as would be experienced for the ACC application.

4.4.1 Mechanical design considerations

The first thing to consider is how to stabilize the two shafts on both ends. The gear designed in [36] was manufactured with a 40 mm stack length and had two bearings per shaft on a single side only.

With the higher rated torque of this MG as well as the longer stack length of 100 mm the shafts would need to be supported on each side. The gear shafts would need to be arranged as in Figure 4.24 with the HS inside the LS and

Stellenbosch University https://scholar.sun.ac.za

the PM carrier on the outside of the LS.

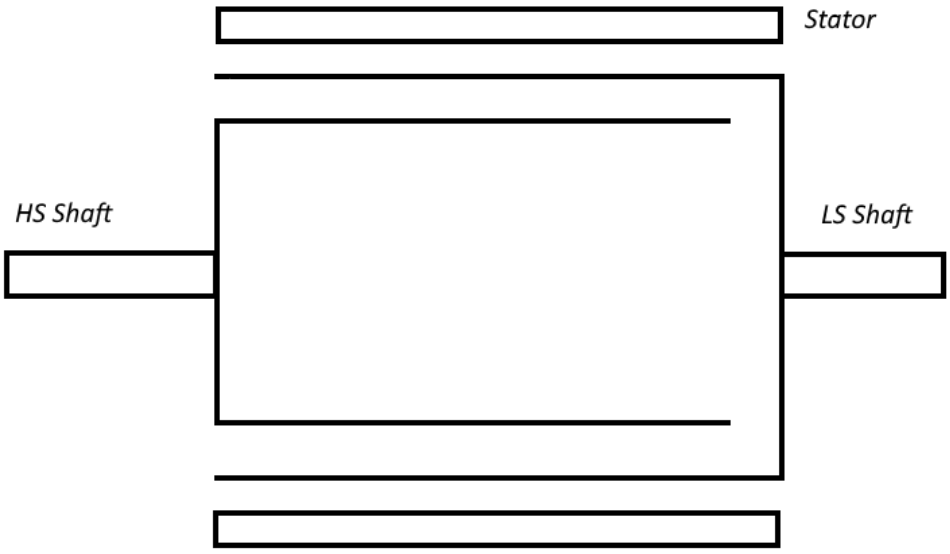

Figure 4.24: Diagram of the mechanical layout of the MG

Each shaft requires two bearings, therefore the HS would need a bearing supported by the inside of the LS and the LS would require a bearing supported on the casing on the HS side. This is challenging as a support structure would need to be placed around the HS shaft connected to the end of the modulator of the LS.

The area requiring support on the LS on both sides are also the areas which experience high magnetic flux density due to the close proximity of the magnets and end leakage flux. The materials would therefore need to be manufactured from non-magnetic materials and the bearings need to be placed as far as possible from the areas with high flux density.

The material supporting the LS is ideally made of a non-magnetic material but finding a replacement for steel proved to be quite a challenge. At first acetal copolymer was considered as it was used in the planetary MG in [29]. After running simulations on the material it was found that the output torque would be too large for the material to handle. The strength of the material as well as the Young's Modulus (E) should be sufficient to carry the torque load as well as be rigid enough to not oscillate during operation.

Stellenbosch University https://scholar.sun.ac.za

The E value vs strength can be seen for some common materials in Figure 4.25. As can be seen steels have an excellent rating and is also cheap and easy to machine.

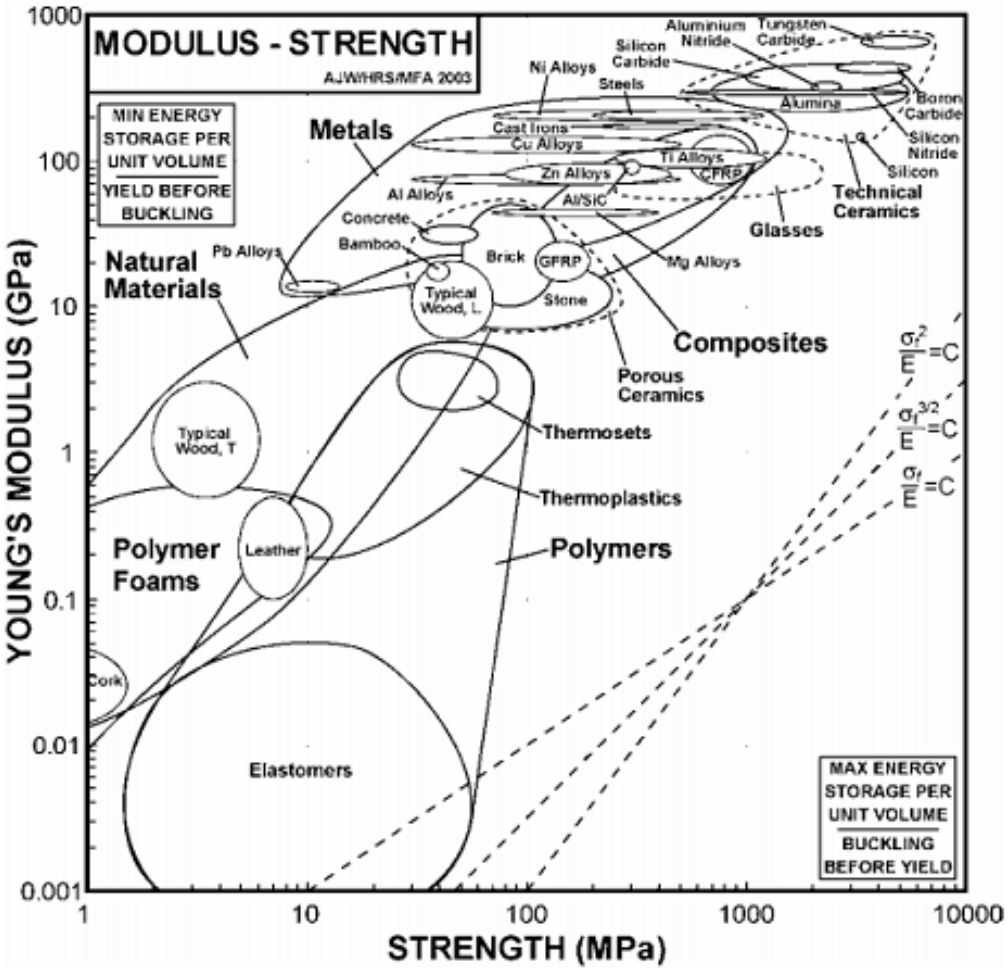

Figure 4.25: Values of Young's Modulus vs strength of common materials [72]

The Young's Modulus (E) can be calculated as in Equation (4.5).

$$E = \frac{\text{Stress}}{\text{Strain}} = \frac{\sigma}{\epsilon} \tag{4.5}$$

The first material considered was an ceramic which proved to be suitable for the purpose. Unfortunately ceramics are very expensive to manufacture and difficult to machine which resulted in the material being disregarded. The next materials considered were thermoplastics which are not as high up on the scale but simulations proved the materials should withstand the required torque levels. TUFNOL and PEEK were two materials next considered which both provide excellent strength, corrosion and hydrolysis resistance [73].

Stellenbosch University https://scholar.sun.ac.za

These materials are available in unfilled, glass filled, paper filled or cotton filled to increase material properties. The material available was a glass filled or unfilled PEEK. The unfilled PEEK was chosen as glass fibres in the material tend to damage cutting machinery and not many manufacturers are willing to perform the task.

Figure 4.26 shows the partial sectional side view of the HS and LS shafts assembly with the PEEK material providing physical separation between the steel shafts and the dense magnetic flux regions. The Peek materials are also used to compress and support the LS laminations as well as stabilise the shafts with bearings on either side. The HS magnets are visible in red.

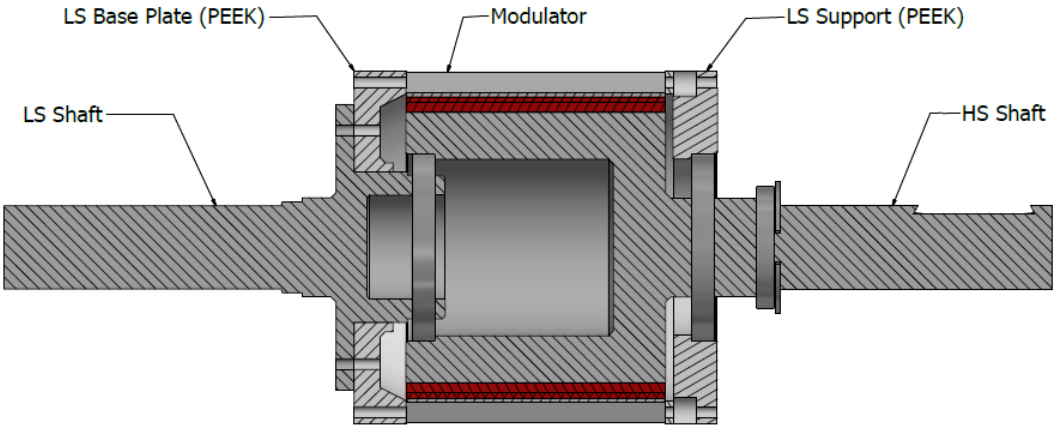

Figure 4.26: Sectional side view of the HS and LS shafts assembly

The threaded rods used to compress the laminations and provide structural support to the LS shaft and rotor would require to be carry the torque load. Figure 4.27 shows the threaded rods used to in the LS assembly.

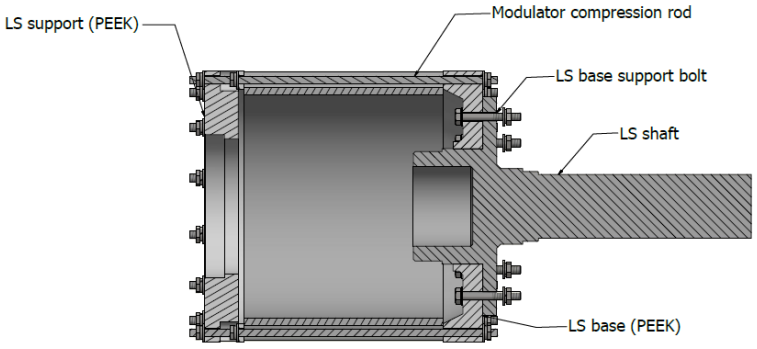

Figure 4.27: Sectional side view of the LS assembly

Stellenbosch University https://scholar.sun.ac.za

Applying force calculations, taking into account the torque load and distance from the centre of the shaft, confirm M3 (3mm diameter) threaded rods would be sufficient but M4 (4mm diameter) rods are chosen for the purpose of a safety factor against failure, especially in load spikes during vibration or start-up conditions.

The PM carrier, also consisting of laminations, requires rods for compression and structurally stability. Figure 4.28 shows the sectional side view of the PM carrier with permanent magnets in the centre and two acetal copolymer rings.

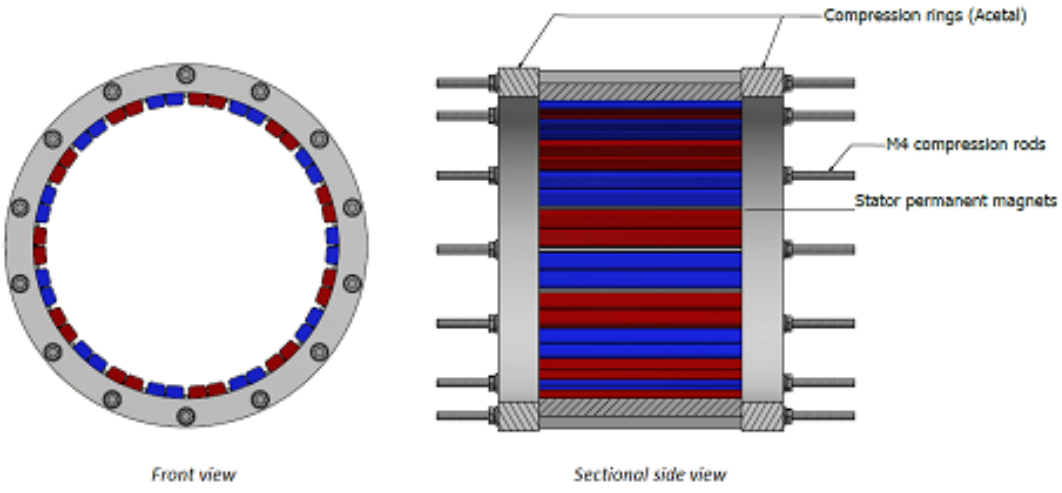

Figure 4.28: Front view and sectional side view of the PM carrier assembly

Acetal was chosen due to it's reduced material cost. The torque on the PM carrier is also lower and rods are situated on the component at larger radius thus reducing the sheer force. The threaded stainless steel rods protrude from the assembly as the ends of these rods are attached to the HS and LS casings as seen in Figure 4.29.

The front view in Figure 4.29 shows nylon insulation bushings used to electrically isolate the stainless steel threaded rods. This is to avoid eddy current circulation through gear casing and rods as discussed in Chapter 3.

The modulator laminations require a mould for proper alignment and positioning. The optimised modulator bridge is 0.65 mm but this is a very weak thickness for the 0.5 mm laminated steel which could easily deform making assembly difficult.

The bridges are therefore thickened to 5 mm and a key is also added. This key allows accurate alignment of the laminations in the radial direction while the

Stellenbosch University https://scholar.sun.ac.za

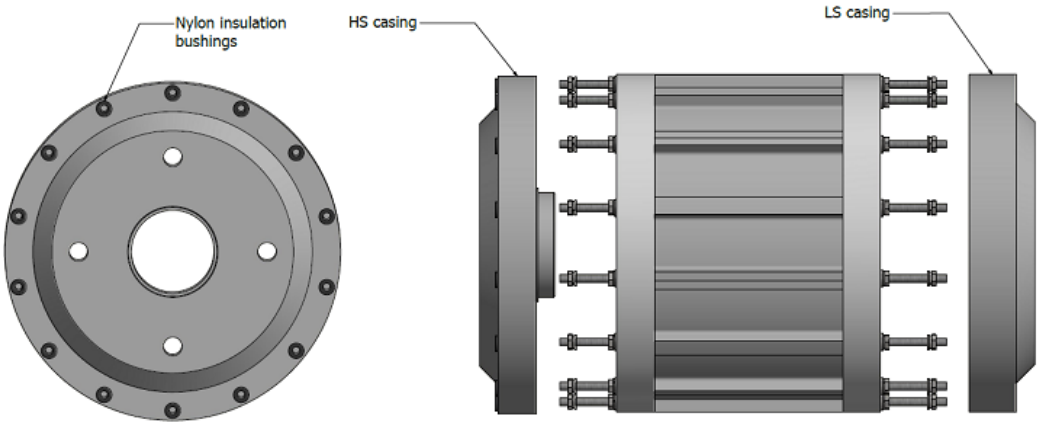

Figure 4.29: Front view and side view of the casing and PM carrier assembly

aluminium mould keeps the components aligned in the axial direction. Figure 4.30 shows the modulator mould assembly.

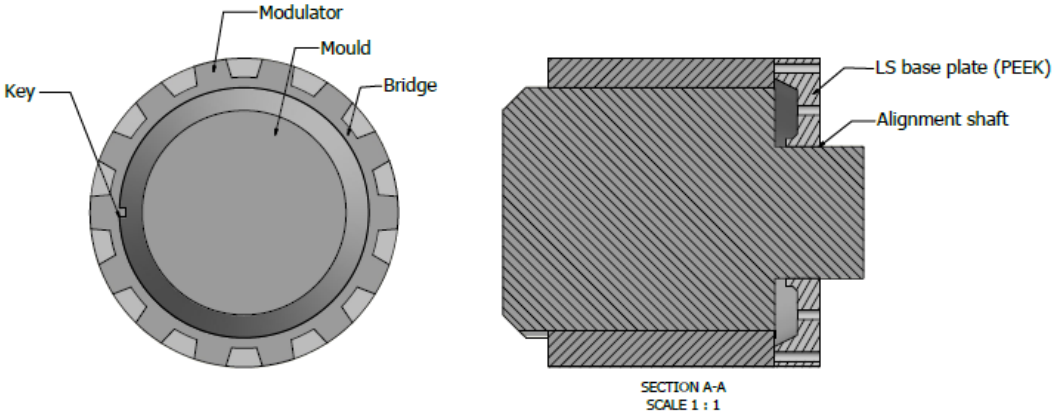

Figure 4.30: Front view and side view of the casing and PM carrier assembly

The Aluminium mould is also cut to the exact dimensions where the LS shaft enters the LS base plate. This further aids in the alignment of the entire sub assembly. Once the LS assembly is completed and epoxy is applied between the lamination and rod sections, the Aluminium mould can simply be pushed out and the remaining components will be accurately aligned.

After the epoxy is cured the thickened bridges and key would need to be machine to the design dimensions. The LS shaft can now be attached to the LS base plate and fastened with M4 (4 mm diameter) bolts.

Stellenbosch University https://scholar.sun.ac.za

Chapter 5

Mechanical construction of a FMMG prototype

In this chapter the manufacturing and assembly process of the FMMG prototype is described in detail. To avoid mechanical failure stress analysis on critical sections of the components will be assessed.

5.1 Mechanical stress analysis of critical components

Before manufacturing can take place the mechanical strength and durability of the components need to be verified.

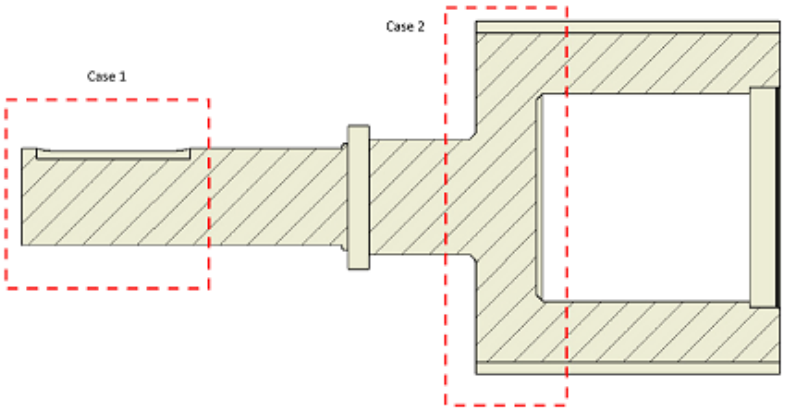

Figure 5.1: Stress cases on the HS shaft

According to simulations the highest torque on the HS is predicted as 88 Nm. Taking this into account the high speed shaft outer diameter is 32 mm with a key placed in the shaft. According to [74] the following stress concentration factors are valid for case 1 shown in Figure 5.1.

Stellenbosch University https://scholar.sun.ac.za

Table 5.1: Stress analysis constants [74]

Factor	Value	Description
OD_1	32 mm	Outer diameter
ID_1	0 mm	Inner diameter
K_{t_z}	2.7	Bending stress
K_{ts_z}	2.2	Torsional stress

The maximum torque is rated at 88 Nm and the minimum at 0 Nm. Obtaining the median (T_mz) and amplitude (T_az) torque is calculated in Equations (5.1) and (5.2):

$$T_mz = \frac{T_{max}z + T_{min}z}{2} = 44\,\text{Nm} \tag{5.1}$$

$$T_az = \frac{T_{max}z - T_{min}z}{2} = 44\,\text{Nm} \tag{5.2}$$

The moment of Inertia for Z axis is calculated in (5.3):

$$I_z = \frac{\pi}{64}\left[OD_1^4 - ID_1^4\right] = 5.1472 \times 10^{-8}\,\text{m}^4 \tag{5.3}$$

The polar moment of inertia for z axis is calculated in (5.4). This is used in the calculation as a material's ability to resist torsion.

$$J_Gz = 2 \times I_z = 1.0294 \times 10^{-7}\,\text{m}^4 \tag{5.4}$$

The shear forces median and amplitude are now calculated as:

$$\tau_mz = \frac{T_mz\frac{OD_1}{2}}{J_Gz} = 6.8775\,\text{MPa} \tag{5.5}$$

$$\tau_az = \frac{T_az\frac{OD_1}{2}}{J_Gz} = 6.8775\,\text{MPa} \tag{5.6}$$

Since σ_mz σ_az equals zero (no moment of inertia on the shaft), the Von Mises constants for the median and amplitude forces are:

$$\sigma_m^{'}z = \sqrt{\left[K_{t_z}\sigma_mz\right]^2 + 3\left[K_{ts_z}\tau_mz\right]^2} = 26.207\,\text{MPa} \tag{5.7}$$

$$\sigma_a^{'}z = \sqrt{\left[K_{t_z}\sigma_az\right]^2 + 3\left[K_{ts_z}\tau_az\right]^2} = 26.207\,\text{MPa} \tag{5.8}$$

Stellenbosch University https://scholar.sun.ac.za

The material properties of EN8 mild steel is shown in Table 5.2 [74].

Table 5.2: Stress analysis constants

Factor	Value	Description
S_y	280 MPa	Yielding force
S_{ut}	550 MPa	Ultimate tensile force
E	200 GPa	Young's modulus

Using the Marin equation to calculate the endurance values of critical points identified on the shaft. To Estimate the endurance limit:

$$\begin{aligned} &\text{if } S_{ut} \leq 1400\,\text{MPa} \\ &\quad S_e^{'} := 0.5 S_{ut} \\ &\text{else} \\ &\quad S_e^{'} := 1400\,\text{MPa} \end{aligned} \tag{5.9}$$

$$\text{Therefore } \; S_e^{'} = 275\,\text{MPa}$$

The surface condition modification factors from [74] using constants for machined or cold drawn mild steel. a = 4.51 and b = -0.265 to calculated:

$$k_a = a\left[\frac{S_{ut}}{1\,\text{MPa}}\right]^b = 0.8472 \tag{5.10}$$

The size modification factor is calculated as:

$$k_b z = 1.24\left[\frac{OD_1}{1\,\text{mm}}\right]^{-0.107} = 0.8558 \tag{5.11}$$

The load modification factor (k_c) equals 0.59 For reliability factor of 99.9% chosen [74]. The Marin equation for endurance limit can now be calculated:

$$\begin{aligned} k_e &= 0.897 \\ S_{ez} &= k_a k_b z k_c k_e S_e^{'} = 105.5184\,\text{MPa} \end{aligned} \tag{5.12}$$

With all this information calculated it is now possible to use the modified-Goodman equation to determine the safety factor (n_z) the critical area:

$$n_z = \frac{1}{\frac{\sigma_a^{'} z}{S_e z} + \frac{\sigma_m^{'} z}{S_u t}} = 3.3782 \tag{5.13}$$

The safety factor on the shaft is calculated to be 3.378 which confirms the shaft is able to support the load. For case two the safety factor is calculated to be 78.917 using similar calculations. Applying similar calculations for the low speed shaft but with higher torque values as shown in the following equations:

Stellenbosch University https://scholar.sun.ac.za

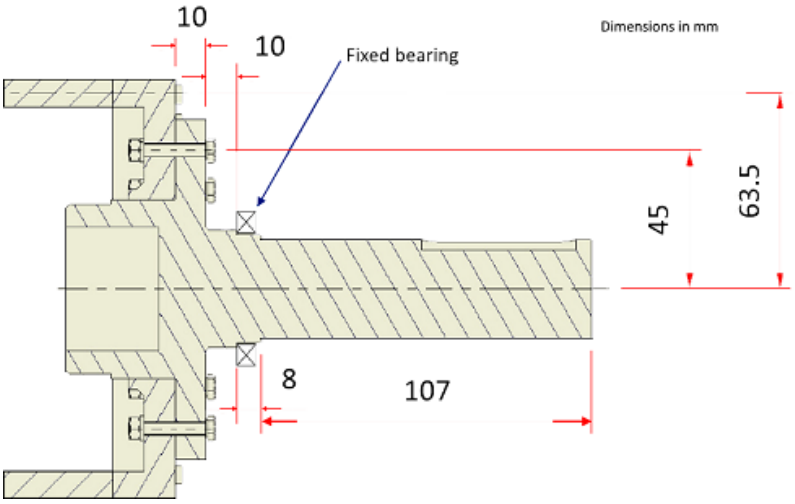

Figure 5.2: Stress cases on the LS shaft

$$T_m z = \frac{T_{max} z + T_{min} z}{2} = 132.5\,\text{Nm} \tag{5.14}$$

$$T_a z = \frac{T_{max} z - T_{min} z}{2} = 132.5\,\text{Nm} \tag{5.15}$$

The safety factor of the low speed shaft is calculated to be 1.3606. This is a smaller safety factor compared to the high speed shaft but as the torque is somewhat over estimated the factor is deemed acceptable. The low-speed shaft support and base plates similar calculations are performed. As a result of the complex structure a 2cm slice of the component is analysed in the stress analysis. Acetal is considered first and achieved a safety factor of 1.7853. But with all the structural weaknesses and vibration on the material a stronger material PEEK was chosen for the design. See Figure 5.3 which shows the PEEK LS base component and dimensions.

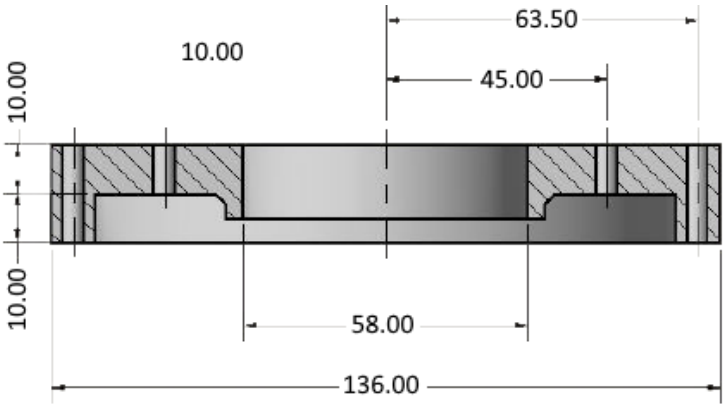

Figure 5.3: LS support stress calculation dimensions

Stellenbosch University https://scholar.sun.ac.za

The support and compression rods are the last section to be analysed. Eight M4 stainless steel rods connect the mild steel low-speed shaft to the LS base at a diameter of 45 mm. Another 15 rods compress and support the modulator laminations at a diameter of 63.5 mm.

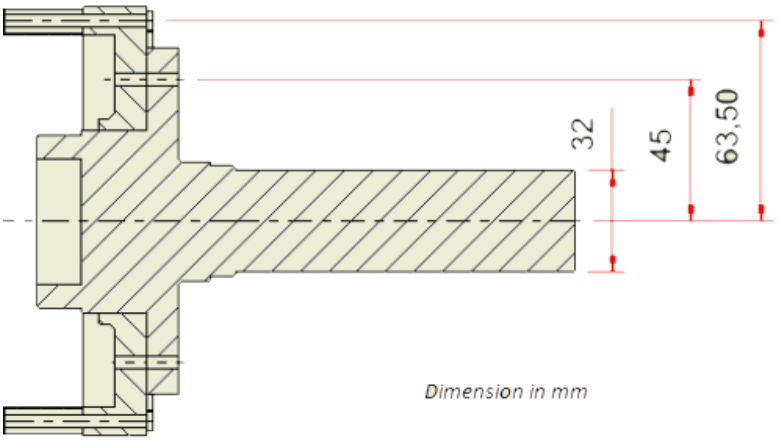

Figure 5.4: Stress cases on the compression rods

For the most critical case the eight bolts which connect the low-speed shaft to the LS base is analysed. In case of failure the smaller diameter placement of these bolts as well as the lower amount of bolts would case failure before the outer rods. Table 5.3 shows the relevant dimensions and factors.

Table 5.3: Stress analysis constants

Factor	Value	Description
n_{bolts}	8	number of bolts
r_{shaft}	45 mm	radius of bolts
d_{bolt}	3.141 mm	minor diameter of bolt
$Torque$	265 Nm	torque with safety factor
S_y	310 MPa	Yielding force (Bolt steel grade 4.8)

The shear yield strength S_{sy} can be calculated by Equation (5.16):

$$S_{sy} = 0.577 S_y = 1.7887 \times 10^8 \,\text{Pa} \tag{5.16}$$

The Forces experience by the bolts can be calculated by Equation (5.17)

$$F = \frac{Torque}{r_{shaft}} = 5888.8889 \,\text{N} \tag{5.17}$$

The area of the bolt is calculated in Equation (5.18)

Stellenbosch University https://scholar.sun.ac.za

$$A_{bolt} = \frac{d_{bolt}^2}{4}\pi = 7.7486 \times 10^{-6} \tag{5.18}$$

The shear forces per bolt is now calculated in Equation (5.19):

$$\tau = \frac{F}{n_{bolts} A_{bolt}} = 9.4999 \times 10^{7}\,\text{Pa} \tag{5.19}$$

The safety factor can now be calculated in Equation (5.20):

$$n = \frac{S_{sy}}{\tau} = 1.8829 \tag{5.20}$$

The safety factor is calculated as 1.889 which is deemed acceptable. The bolts on the outer section can be calculated in a similar fashion and achieves a safety factor of 5.0996. Full calculations for all critical components can be seen in Appendix B.

5.2 Construction

The construction process of an FMMG is described in this section. The list of FMMG components and their material specifications are given in Table 5.4.

Table 5.4: Components of the magnetic gear

Item no.	Parts	Quantity	Part number/Material
1	HS rotor	1	Steel
2	LS rotor	1	Steel
3	LS base plate	1	PEEK thermoplastic
4	LS support	1	PEEK thermoplastic
5	Compression ring	1	Stainless steel
6	Modulator laminations	1	M400-50A (C5 coating)
7	HS casing	1	Aluminium
8	LS casing	1	Aluminium
9	Support ring	2	Acetal copolymer
10	PM carrier laminations	1	M400-50A (C5 coating)
11	HS permanent magnets	16	NdFeB (N48H)
12	PM carrier permanent magnets	44	NdFeB (N48H)
13	Bearing large	2	SKF 61807-2RZ
14	Bearing small	2	SKF 61811-2RZ
15	Modulator threaded rods	14	M4 Stainless steel
16	PM carrier threaded rods	14	M4 Stainless steel
17	Insulation bushes	14	Nylon
18	Circlip	1	3BMI-48
19	Epoxy	-	AMPREG 21

Stellenbosch University https://scholar.sun.ac.za

5.2.1 High speed rotor

The HS PM carrier was made from (EN8 grade) mild steel using a CNC machine as shown in Figure 5.5(a). The spacers for positioning PMs can be clearly seen in Figure 5.5(b).

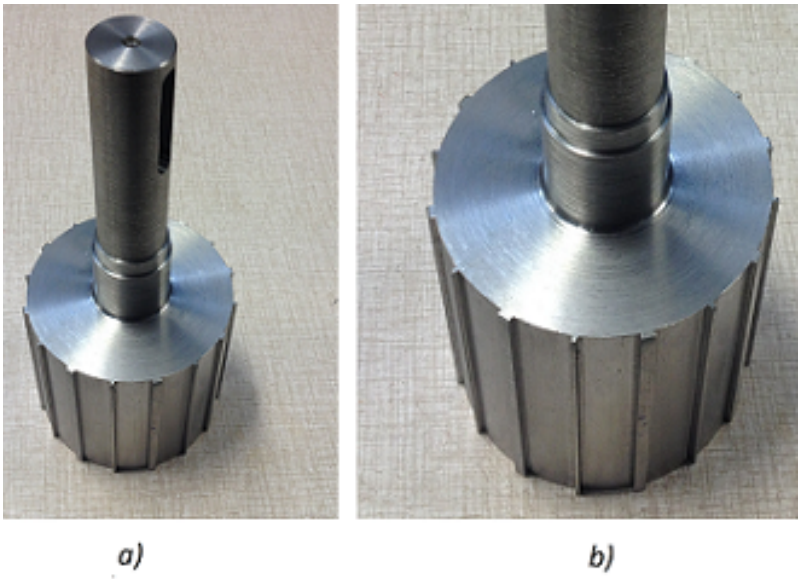

Figure 5.5: (a) HS rotor (b) close up of spacers on HS rotor

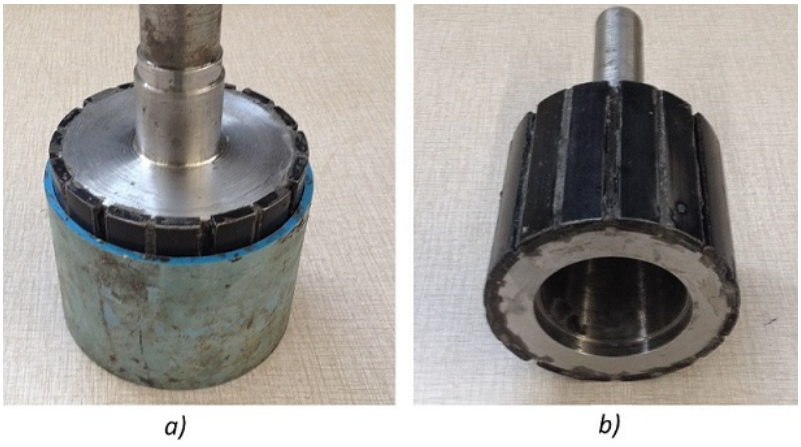

Figure 5.6: (a) HS PMs assembled with PVC tube around the assembly, (b) completed HS rotor with magnets

Permanent magnets are glued into the slots using epoxy. A carefully prepared PVC pipe is used to secure PMs into correct positions as seen in Figure 5.6(a). Figure 5.6(b) Shows the completed HS rotor with magnets.

Stellenbosch University https://scholar.sun.ac.za

5.2.2 Low-speed rotor

The low speed rotor assembly consists of laminations, support rings, the steel shaft and threaded rods used for compression and structural support. Figure 5.7 shows an exploded view of the complete LS assembly and how all parts are interconnected.

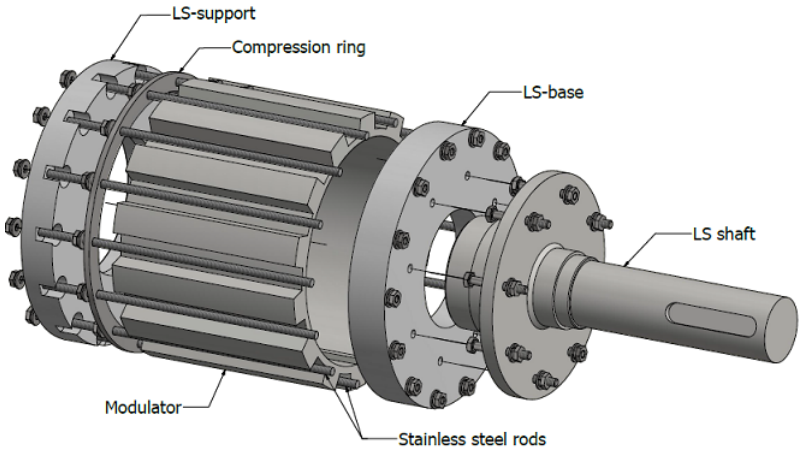

Figure 5.7: An exploded view of the complete LS assembly

The first phase of the LS rotor assembly is to compress the laminations between the LS base and the compression ring as shown in Figure 5.8(a). The mould is fitted to the LS base and laminations are placed over this for alignment (see Figure 5.8(b)).

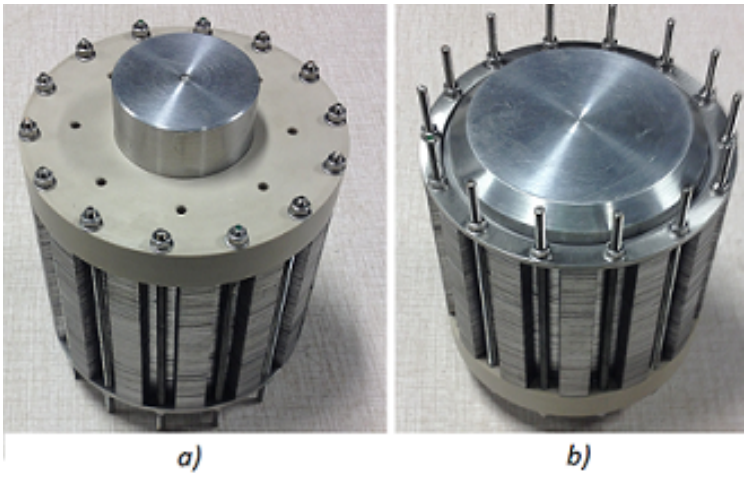

Figure 5.8: Assembly of LS rotor: compression and alignment of laminations

Stellenbosch University https://scholar.sun.ac.za

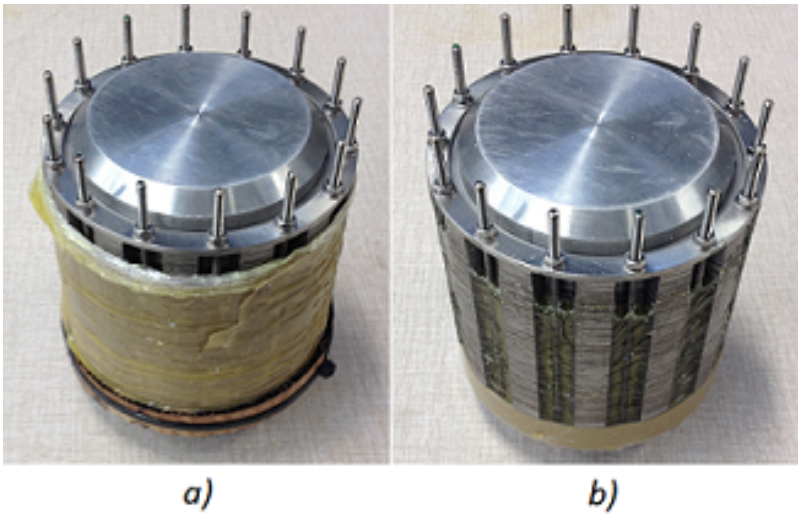

Figure 5.9: The LS rotor during the epoxy phase (a) preparation, and (b) cured by epoxy

Next plastic is wrapped around the lamination sections and supported with tape. Epoxy is then poured into the cavities. Figure 5.9(a) shows the plastic sealed LS assembly and (b) the LS assembly cured by epoxy.

Figure 5.10: Stainless steel vacuum chamber used to remove air pockets from epoxy

Stellenbosch University https://scholar.sun.ac.za

As the epoxy cures the volume shrinking and/or cracking often occur so that it is important to check and fill in epoxy as needed. This ensures that all the cavities are filled. Once the epoxy is applied the component is placed in a vacuum chamber (shown in Figure 5.10) to force out all trapped air pockets and bubbles. The epoxy then cures as a more structurally stable material.

As shown in Figure 5.10(a) thick perspex disc seals the chamber and allows the process to be monitored from the outside, ensuring that no epoxy leakage or excessive bubbling occurs. Once the epoxy is cured the plastic is removed from the laminations and cleaned. The LS assembly is smoothed using a lathe to ensure correct size and surface condition. before the aluminium mould is removed in a press. Once this is completed the LS assembly is attached to the LS base. The inner surface of the LS rotor can be machined and checked on a lathe to ensure accuracy. Figure 5.11 shows the manufactured LS rotor assembly.

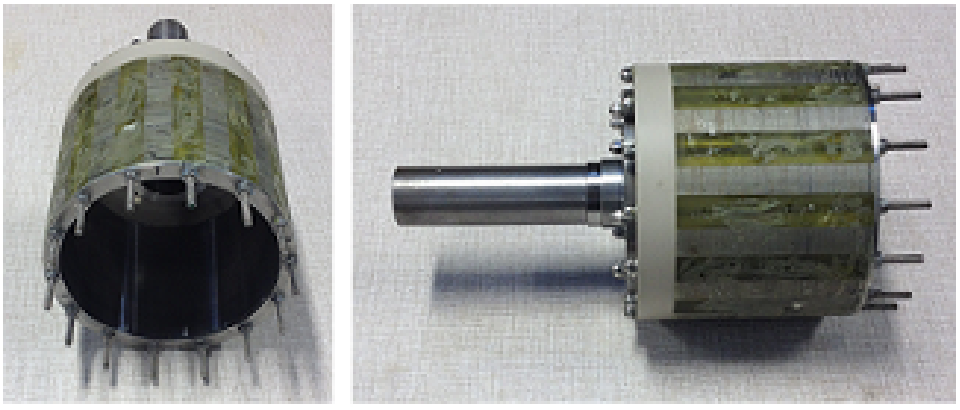

Figure 5.11: The manufactured LS rotor assembly (a) section view (b) side view

5.2.3 Outer PM carrier

The outer PM carrier consists of laminations compressed in a similar fashion to the LS assembly. A mould is placed in the centre to align the laminations vertically. The two white acetal compression rings can be seen in Figure 5.12 on either side of the laminations. A number of threaded rods are placed through the rings and laminations to compress and support the structure.

On the outside of the PM carrier special clips are placed to align the laminations radially. These clips are manufactured from 10 x 16 mm key steel and fit

Stellenbosch University https://scholar.sun.ac.za

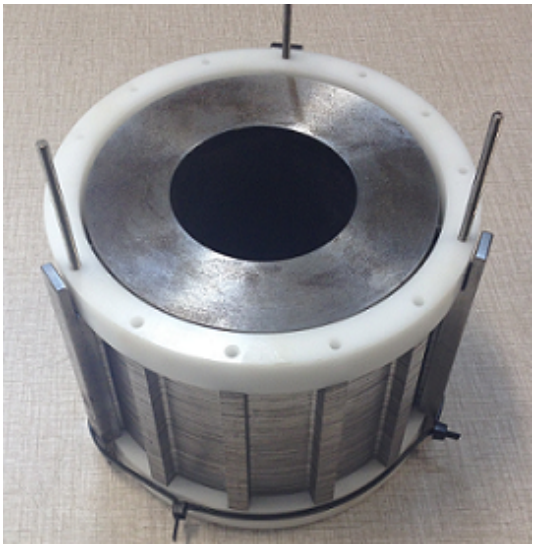

Figure 5.12: (a) HS shaft (b) close up of spacers on HS

tightly over the threaded rod in support of the PM carrier yoke. Figure 5.13 shows three views and dimensions of the PM carrier alignment clips. When the laminations are compressed the clips are removed and the entire component is placed in a press to remove the inner mould. The outside of the PM carrier is then painted with a rust inhibiting paint to avoid corrosion of the outside of the laminations.

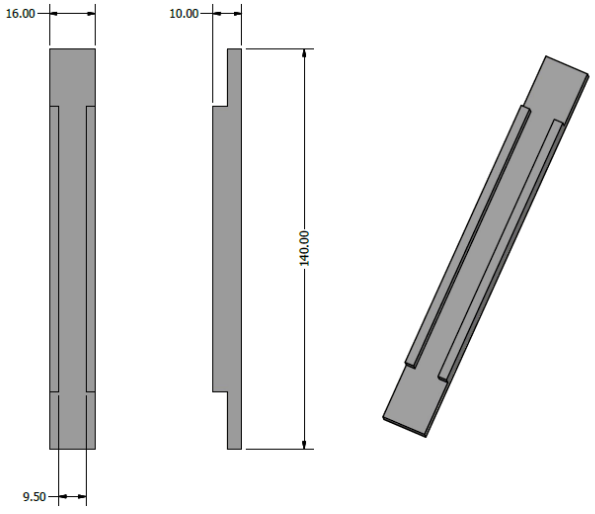

Figure 5.13: Specially made PM carrier alignment clips

The magnets can now be placed on the inside of the PM carrier assembly. The magnets are placed four or five pole pairs at a time depending on the space available for placement. G clamps are used to compress the magnets

Stellenbosch University https://scholar.sun.ac.za

into position with wooden blocks as shown in Figure 5.14(a). The post-epoxy PM carrier assembly is shown in Figure 5.14(b), in which it can be seen that the areas of the PM carrier not involved in the epoxy process are covered with newspaper and tape.

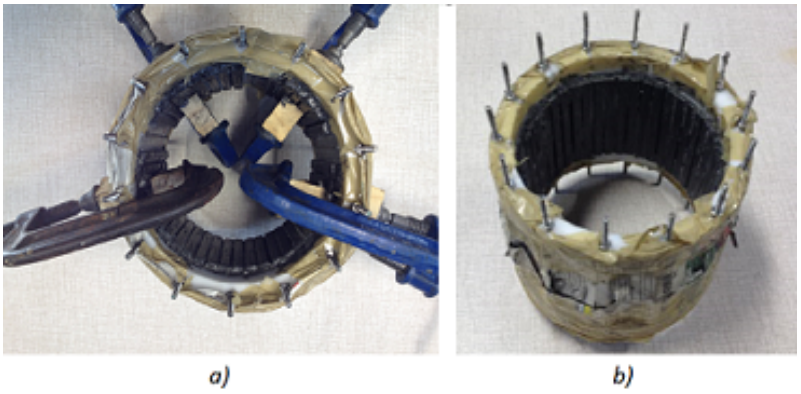

Figure 5.14: Manufacturing of the PM carrier (a) magnets placements, (b) the post-epoxy PM carrier assembly

5.2.4 Assembly

The assembly is performed in a lathe with the LS rotor clamped and kept in stationary, the HS rotor is then secured using a 32 mm cutter clamp which can be moved towards the LS in a controlled manner. As shown in Figure 5.15 the HS rotor is centred with the position pin on the right for precise alignment of the rotors before the assembly. The PVC pipe is kept on the magnets for as long as possible to avoid damage from any nearby tools.

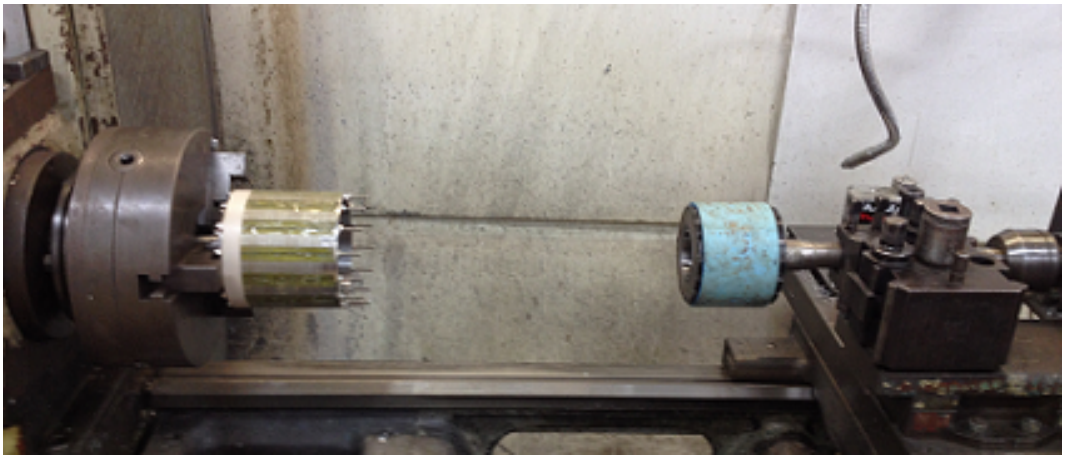

Figure 5.15: Assembling process of the HS-LS rotors assembly

Stellenbosch University https://scholar.sun.ac.za

With the HS rotor inserted safely into the LS rotor supported with a bearing between the two shafts the support disc of LS rotor can be attached to the protruding threaded rods and secured as shown in Figure 5.16 (left). The HS rotor casing is then attached to secure both shafts with bearings on the other side as shown in Figure 5.16 (right).

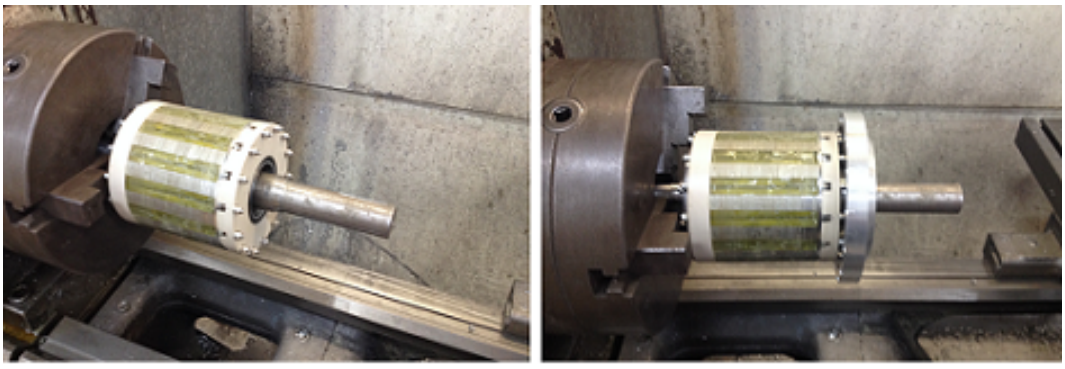

Figure 5.16: Complete HS and LS rotor assembly

Finally, the completed shafts assembly is again secured on the lathe. As shown in Figure 5.17(a) the PM carrier is moved into position with four 100 mm M10 threaded bolts controlling the movement. The bolts are inserted into the mounting holes in the casing and pushes against the LS rotor. Turning these bolts out of the casing allows the PM carrier to slide into position in a controlled manner. The final positioning is performed by fastening the threaded rods on the HS shaft as seen in Figure 5.17(b).

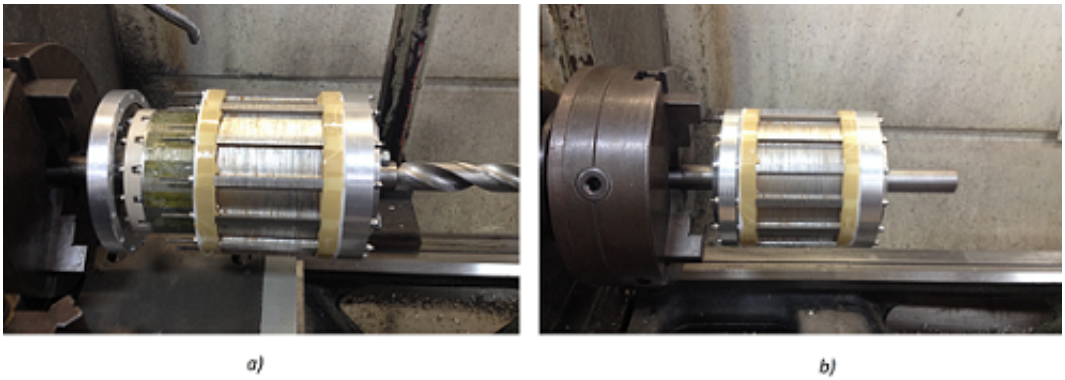

Figure 5.17: Final assembly process (a) inserting the PM carrier using guiding rods (b) final positioning of the PM carrier

Stellenbosch University https://scholar.sun.ac.za

As the gear was fully assembled it was discovered that the PM carrier magnets interfered with the LS rotor and therefore caused friction. The root was identified as tolerance creep from manufacturing multiple components including the laser cut steel laminations, compression rings and drill holes in the aluminium casings.

The fact that a alignment shoulder was not added to the design increased the severity of the problem. To address the issue two aluminium rings were manufactured and press fit over the outside of the gear to align the PM carrier laminations and both the LS and HS rotors casings.

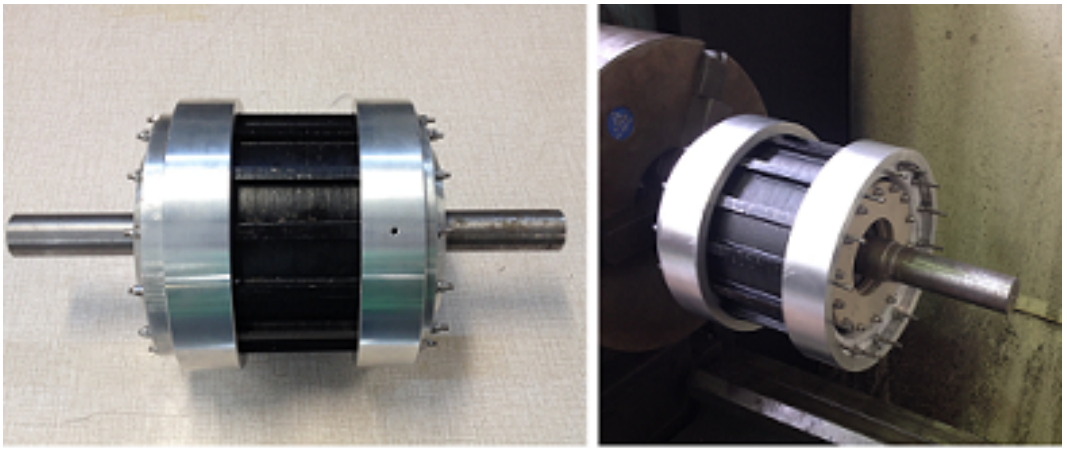

Figure 5.18: Complete MG assembly (a) side view (b) MG assembly with HS casing removed showing the working position of an alignment ring

Figure 5.18(a) shows the completed gear assembly with aluminium alignment rings. In Figure 5.18(b) the gear is shown with HS casing removed clearly showing internal components of the gear and how the alignment rings aligns the laminations and aluminium casing.

Stellenbosch University https://scholar.sun.ac.za

Chapter 6

Performance evaluation

In this chapter the performance characteristics of both the FMMG prototype and an equivalent mechanical gear are experimentally evaluated and compared.

6.1 Experimental setup

The test setup is shown in Figure 6.1, which consists of a geared VSD induction motor drive as the prime mover, two Lorenz torque sensors for input/output speed and torque measurements, and a second geared VSD induction motor drive running in regenerative mode as the load. The gear under test is connected between the two torque sensors. An accelerometer is attached to the gear to measure vibration.

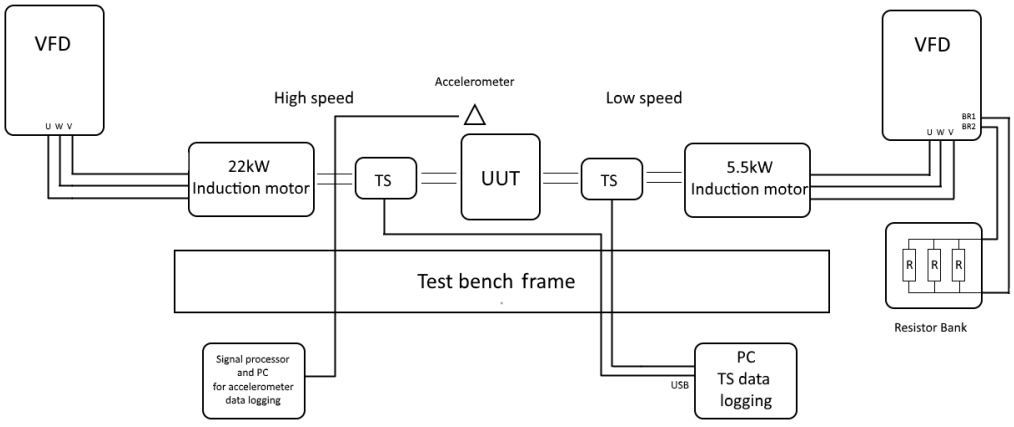

Figure 6.1: Experimental setup diagram for gear performance tests.

Stellenbosch University https://scholar.sun.ac.za

6.2 No-load tests

First the no-load losses of both mechanical and magnetic gears are measured. This entails removing the generator used as load from the output shaft and only driving the gears with the input. The no-load losses of the gears is given in Figure 6.2. It can be observed that the power loss in the FMMG directly follows the speed. The no load losses increase from zero at stand still to a peak of 190 W at rated speed. The no-load loss in the mechanical gear is significantly less than that in the FMMG. The no-load losses in FMMG contains both mechanical and electromagnetic core loss components. Since the electromagnetic losses is proportional to the square of the frequency (speed), the largely linear relation between them indicates that the majority of the no-load loss in the FMMG is mechanical loss.

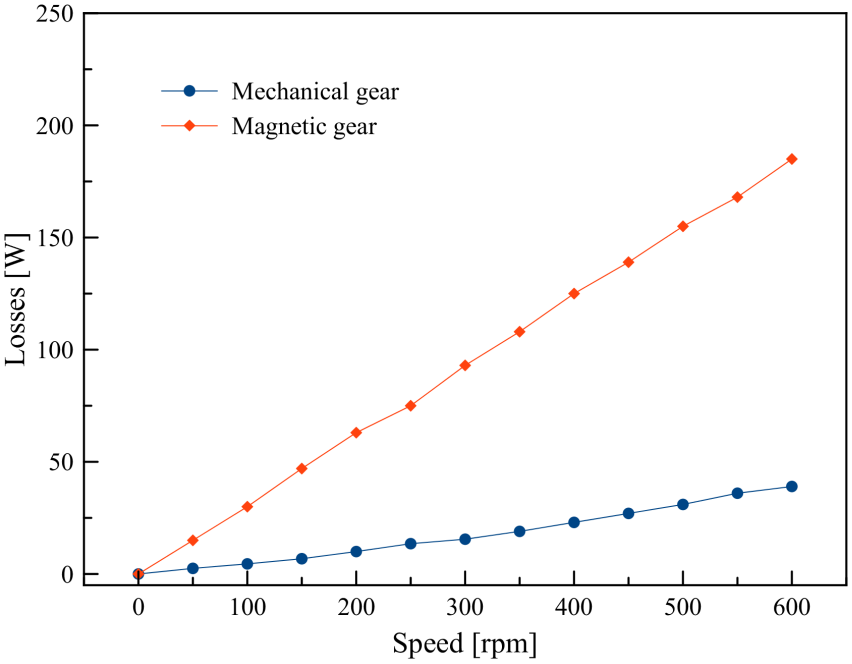

Figure 6.2: No-load losses of gears at different speeds (high speed side).

6.3 Load tests

For load test, both gears are tested at different speeds and torque loads ranging from 80 rpm to 160 rpm and 25 Nm to 132 Nm (rated), respectively on the LS shaft of the MG. The tests are first conducted at ambient temperature of about 20°C and then repeated at artificially created 40°C ambient condition. The latter is the typical on-site ambient temperature of ACC systems.

Stellenbosch University https://scholar.sun.ac.za

Figures 6.3 and 6.4 are the photos of the test setups for mechanical and magnetic gears, respectively.

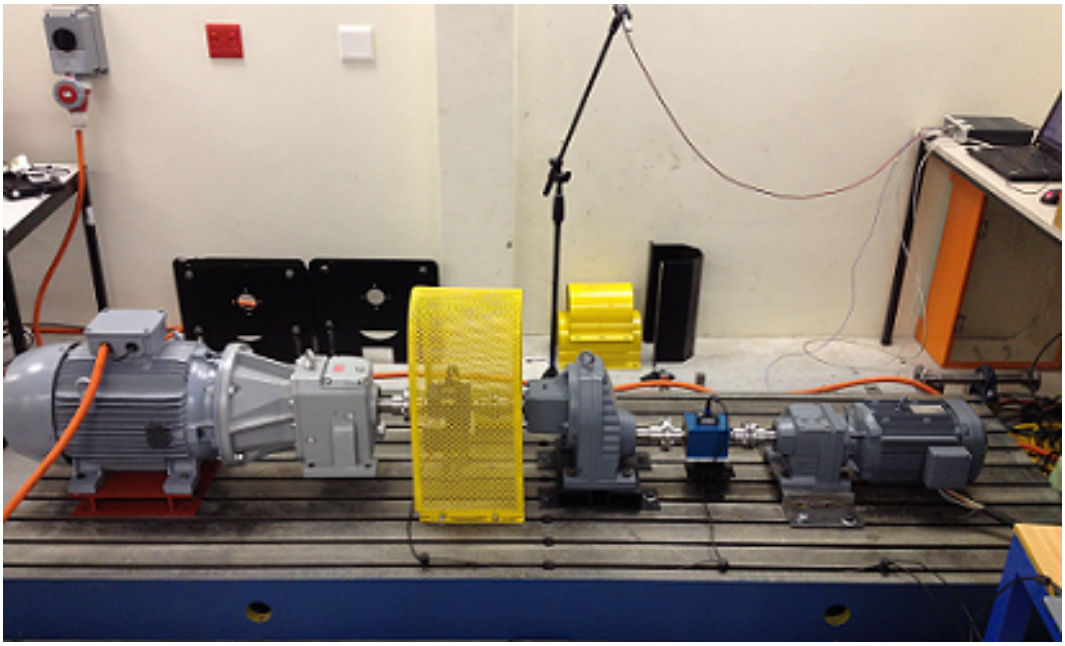

Figure 6.3: Mechanical gear test bench setup

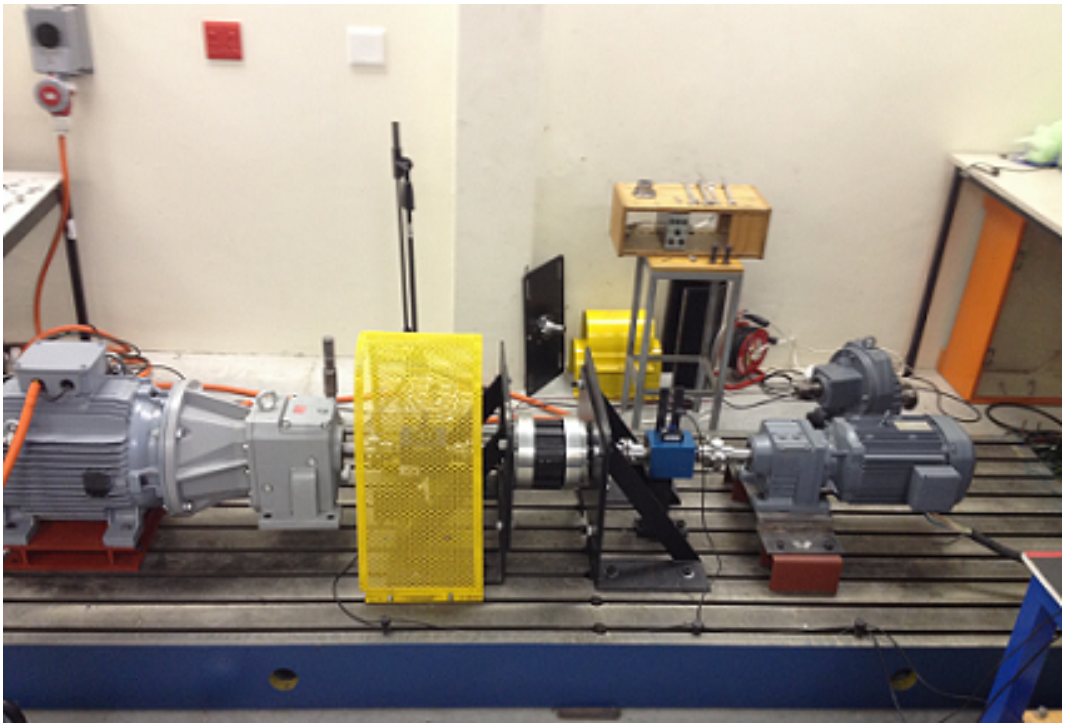

Figure 6.4: Magnetic gear test bench setup

Stellenbosch University https://scholar.sun.ac.za

6.3.1 $T_{ambient} = 20°C$

The measured input and output power of the mechanical gear as a function of speeds with load torque as a parameter is shown in Figure 6.5 ($T_{ambient}$=20°C). The resultant power losses and efficiencies are tabulated in Table 6.1. The efficiency of the mechanical gear ranges from 78-79% at low load conditions to above 95% at rated loads. It can be observed that the losses increase with both load and speed for mechanical gears. The efficiency map of the mechanical gear is given in Figure 6.6, in which the blue regions represent lower efficiency values and the red areas higher efficiency values as shown in the colour key.

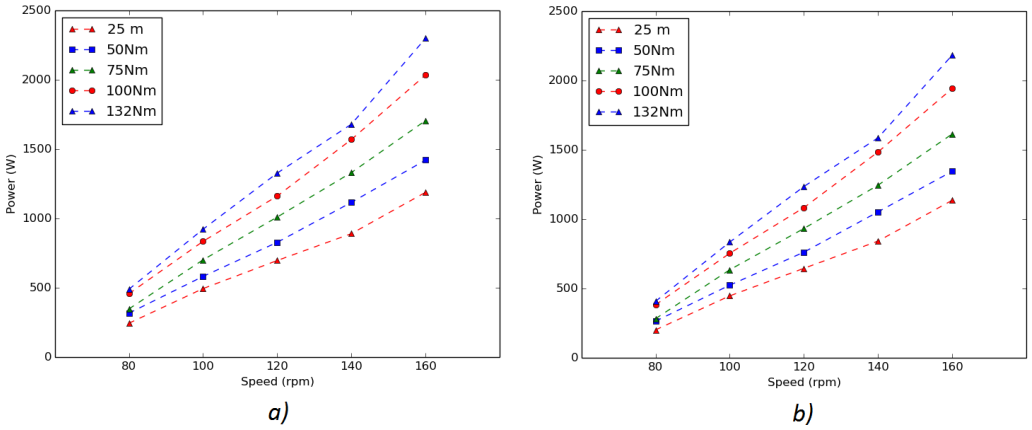

Figure 6.5: The measured input (a) and output (b) powers of the mechanical gear as a function of speeds with torque rating as a parameter ($T_{ambient}$=20°C).

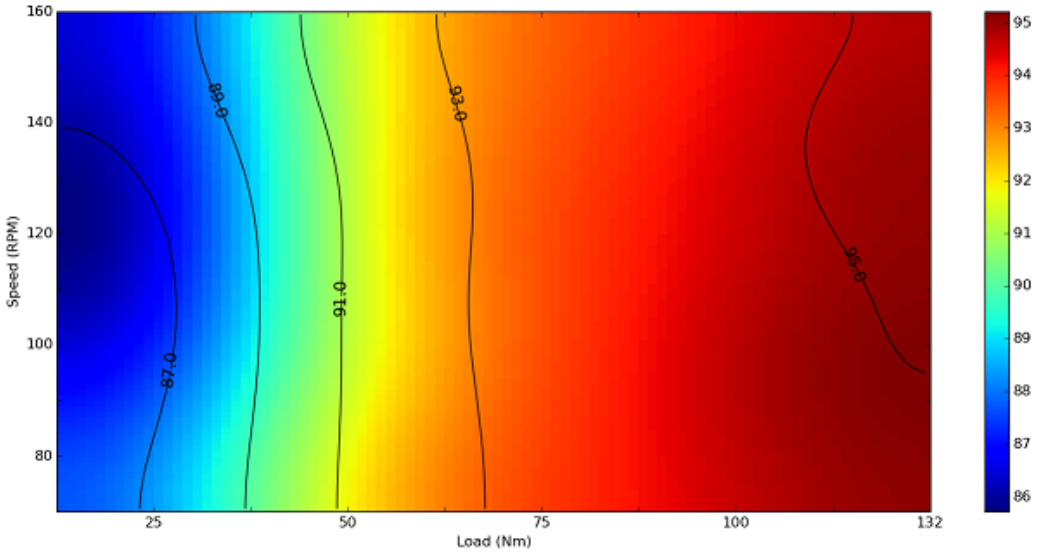

Figure 6.6: The efficiency map of the mechanical gear ($T_{ambient}$=20°C).

Stellenbosch University https://scholar.sun.ac.za

Table 6.1: Measured losses and efficiencies of the mechanical gear at different speeds and torques ($T_{ambient}$=20°C)

(a) Power losses [W] for different speeds and torques

Speed [rpm]	25	50	75	100	132
160	81.6	76.4	88.8	102.6	102.5
140	67.9	78.6	83.2	86.8	70.6
120	61.0	63.0	69.9	73.8	72.9
100	51.5	56.0	56.8	61.9	58.8
80	36.2	42.3	40.7	41.3	45.6
	Torque [Nm]				

(b) Efficiency [%] for different speeds and torques

Speed [rpm]	25	50	75	100	132
160	78.9	91.3	92.7	94.1	95.2
140	79.0	90.2	92.7	94.0	96.1
120	83.1	90.4	92.7	94.0	95.3
100	77.9	89.4	93.0	94.1	95.4
80	78.9	90.7	93.4	94.9	95.6
	Torque [Nm]				

The corresponding set of measurements for the magnetic gear are given in Figures 6.7 and 6.8 and Table 6.2. It is noticeable that the losses are slightly higher compared to the mechanical counterpart. It was previously accentuated that the mechanical gear losses are closely related to both the load torque and speed.

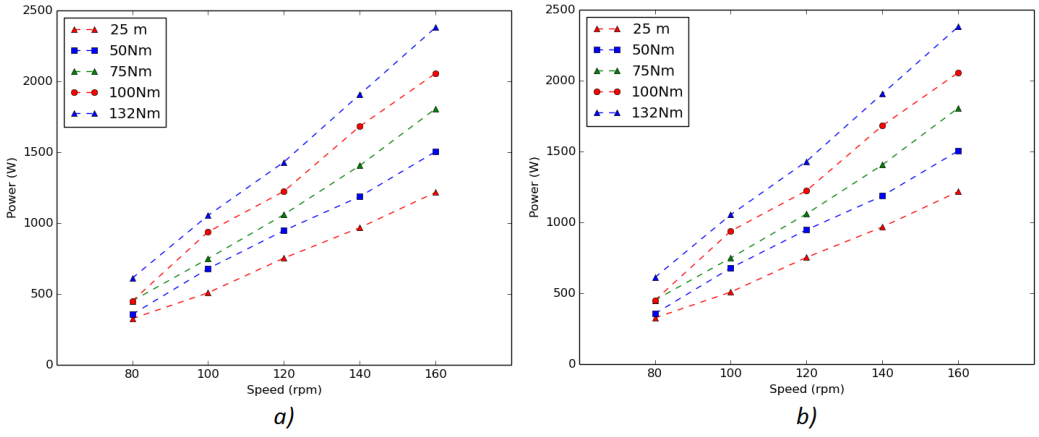

Figure 6.7: The measured input (a) and output (b) powers of the magnetic gear as a function of speeds with torque rating as a parameter ($T_{ambient}$=20°C).

According to Table 6.2 the losses in the magnetic gear are much more sensitive to the speed than to the load torque. During test, especially at no load, an

Stellenbosch University https://scholar.sun.ac.za

eccentricity is present on the low speed shaft, which causes undesired vibration and noise on the low speed shaft and connected components. This is believed to be the cause of the additional losses which are unaccounted for by the simulations. The gear reaches an efficiency at rated load and speed of 93.5%. The gear is also tested at 1.5 times rated torque with a measured efficiency of 94.9%. This equals a power output of 3.3 kW delivered by the gear.

Table 6.2: Measured losses and efficiencies of the FMMG at different speeds and torques ($T_{ambient}$=20°C)

(a) Power losses [W] for different speeds and torques

Speed [rpm]	Torque [Nm]				
	25	50	75	100	132
160	161.8	159.8	158.3	156.0	155.1
140	133.9	134.8	137.9	148.8	153.0
120	116.1	115.5	112.3	110.8	110.6
100	95.3	92.8	91.5	95.6	91.0
80	74.7	76.0	75.1	73.4	73.7

(b) Efficiency [%] for speed vs torque

Speed [rpm]	Torque [Nm]				
	25	50	75	100	132
160	75.0	85.0	88.6	91.7	93.5
140	72.2	85.2	88.6	91.0	92.7
120	75.8	85.1	89.7	91.9	93.8
100	74.4	84.6	89.9	91.7	93.9
80	75.7	84.5	89.7	92.0	94.0

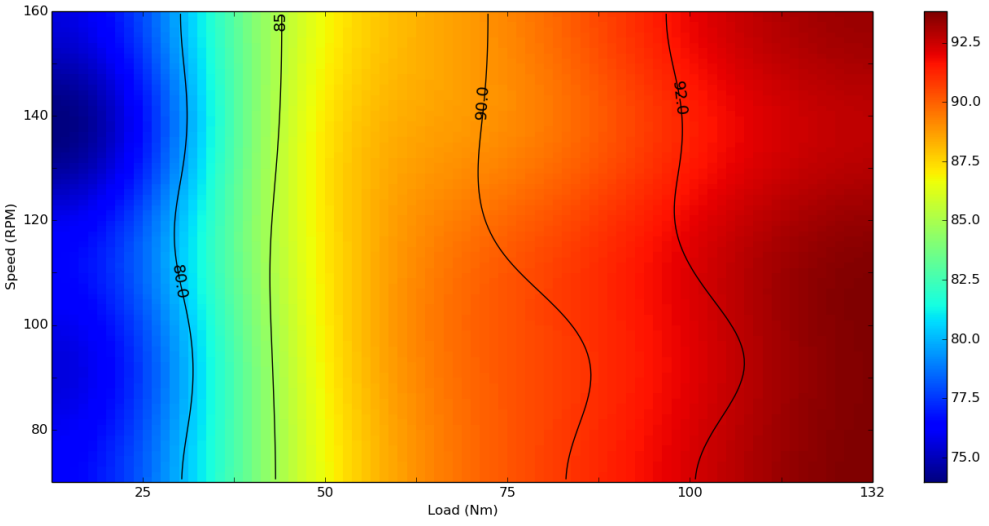

Figure 6.8: The efficiency map of the FMMG ($T_{ambient}$=20°C).

Stellenbosch University https://scholar.sun.ac.za

6.3.2 $\mathbf{T_{ambient}} = 40°\mathbf{C}$

To assess the gear performance under similar on-site ambient temperatures of ACC systems, the same tests are repeated for an ambient temperature of 40°C. To artificially render such a working condition, the gear is operated at rated condition for extended time (about 2 hours) so that the internal heat losses increase the gear temperature. The measurements are taken as soon as the gear's casing reaches 40°C. To reduce the time required for heating up the gear, the gear is wrapped in thermal insulation as shown in Figure 6.9.

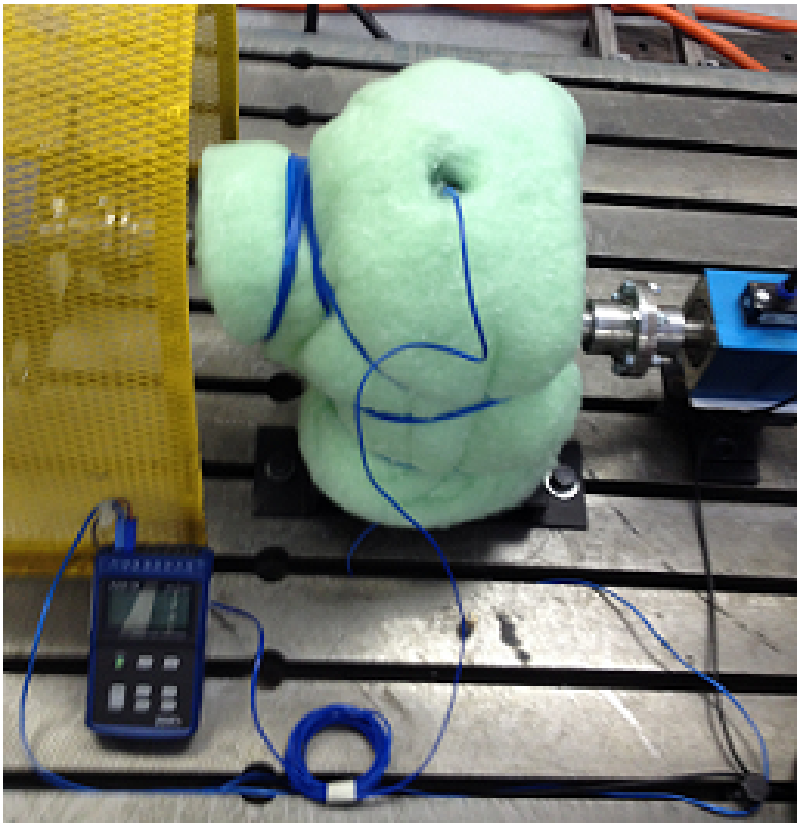

Figure 6.9: Gear wrapped in thermal insulation with temperature sensors

During this heating process a performance reading is taken every 2.5° increase in temperature to determine the temperature effect on the efficiency of the gear at rated torque and speed. As can be seen in Figures 6.10, the efficiency range of both mechanical and magnetic gears at rated conditions remains relatively constant around 95% and 93 to 94%, respectively.

The measured power losses and efficiencies are given in Table 6.3. The efficiency map of the mechanical gear is given in Figure 6.11. The efficiency of the gear increased slightly at lower loads and speed in comparison with the

Stellenbosch University https://scholar.sun.ac.za

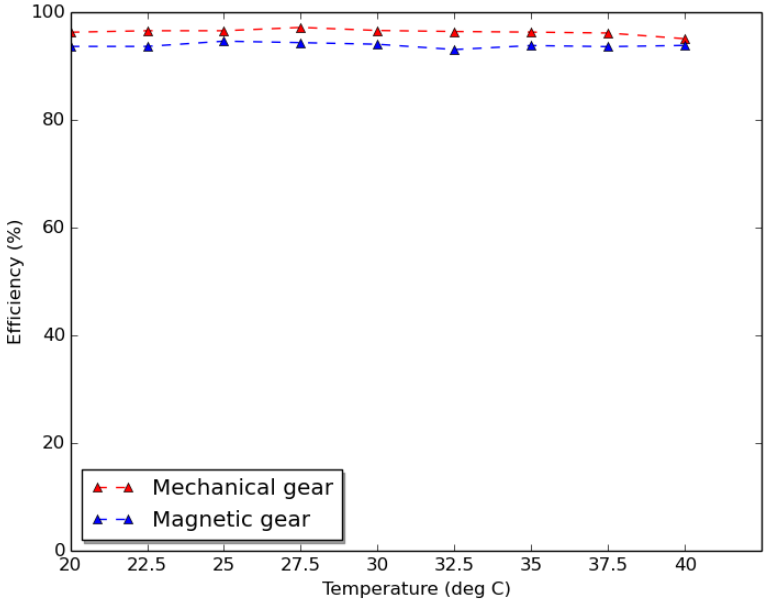

Figure 6.10: Efficiency of mechanical and magnetic gear vs temperature at rated torque and speed

lower temperature tests and stayed relatively similar at rated conditions. The gear tested at 1.5 times rated torque and at rated speed achieved an efficiency of 95.7%. The gear appears to run more efficiently at lower loads and speeds compared to the cold gear.

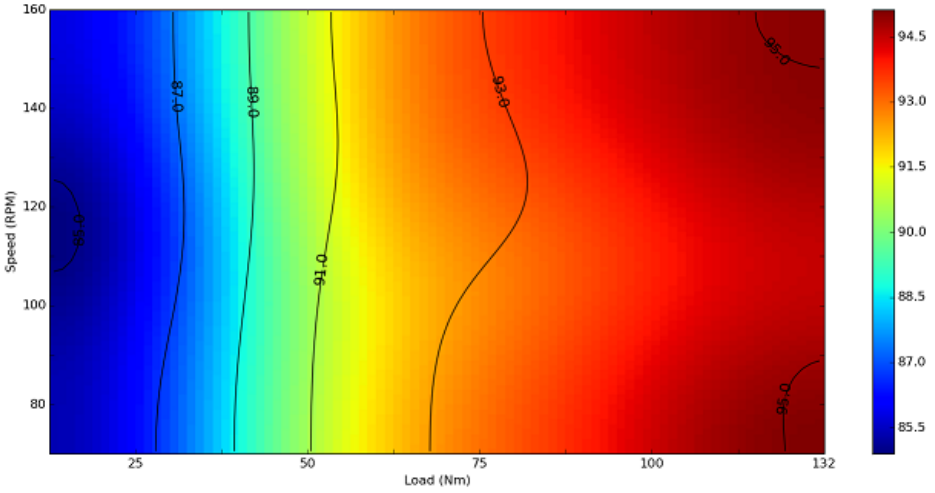

Figure 6.11: The efficiency map of the mechanical gear ($T_{ambient}$=40°C).

The measurements for the magnetic gear under the same temperature condition are given in Table 6.4 and Figure 6.12. The efficiency appears to be almost identical to the cold tested gear, therefore no unwanted effects are discovered

Stellenbosch University https://scholar.sun.ac.za

Table 6.3: Measured losses and efficiencies of the mechanical gear at different speeds and torques ($T_{ambient}$=40°C)

(a) Power losses [W] for different speeds and torques

Speed [rpm]	25	50	75	100	132
160	81.7	87.8	91.8	92.8	115.9
140	74.7	81.0	78.3	84.6	91.9
120	65.0	66.7	77.1	85.9	91.2
100	52.3	57.9	66.0	63.2	75.6
80	42.7	47.4	51.2	48.5	52.3
	Torque [Nm]				

(b) Efficiency [%] for speed vs torque

Speed [rpm]	25	50	75	100	132
160	83.2	90.4	93.0	94.4	94.9
140	83.5	90.2	93.2	94.5	95.4
120	81.1	90.4	92.3	93.5	94.6
100	83.3	90.0	92.0	94.3	94.6
80	82.3	90.3	92.6	94.5	95.5
	Torque [Nm]				

by the higher temperature operation. The 1.5 times rated torque (198 Nm) measurement also resulted in a measured efficiency of 95.0%.

Table 6.4: Measured losses and efficiencies of the FMMG at different speeds and torques ($T_{ambient}$=40°C)

(a) Power losses [W] for different speeds and torques

Speed [rpm]	25	50	75	100	132
160	158.6	161.4	165.1	167.7	147.9
140	134.9	136.5	139.4	114.5	146.5
120	112.6	114.8	119.0	121.6	124.4
100	95.1	97.6	101.5	104.2	104.6
80	77.3	79.6	81.7	82.4	85.3
	Torque [Nm]				

(b) Efficiency [%] for speed vs torque

Speed [rpm]	25	50	75	100	132
160	73.9	84.6	88.4	91.1	93.7
140	69.8	85.4	88.5	93.1	92.8
120	74.9	84.6	88.7	91.3	93.1
100	73.1	85.5	89.2	91.2	93.0
80	76.1	84.2	89.1	91.4	92.9
	Torque [Nm]				

Stellenbosch University https://scholar.sun.ac.za

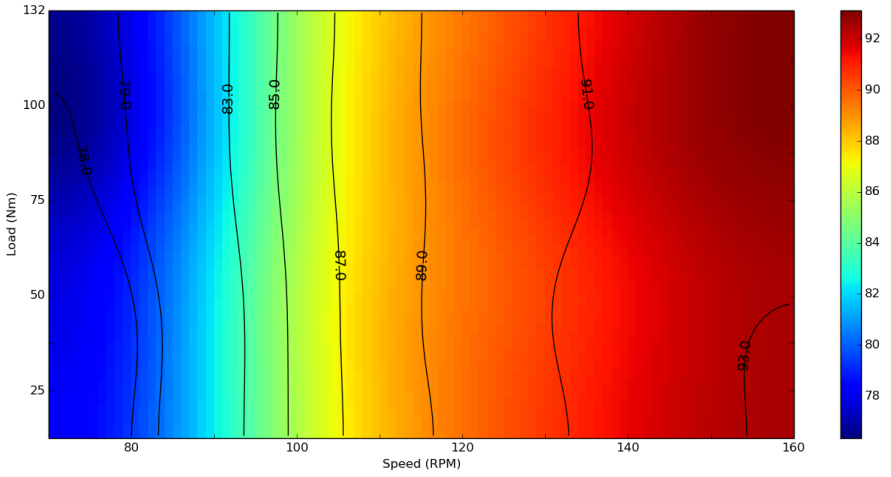

Figure 6.12: The efficiency map of the magnetic gear ($T_{ambient}$=40°C).

6.4 Test under up-speed configuration

For the purpose of further performance analysis both the mechanical and magnetic gears are also tested in the up-speed configuration. Similar tests as performed on down-speed configuration are performed. The test setup is largely the same with the exception that the two VSD induction motor drives swap their respective roles.

Table 6.5: Measured losses and efficiencies of the mechanical gear at different speeds and torques ($T_{ambient}$=40°C) (up-speed configuration)

(a) Power losses [W] for different speeds and torques

Speed [rpm]	25	50	75	100	132
160	81.6	76.4	88.8	102.6	102.5
140	67.9	78.6	83.2	86.8	70.6
120	61.0	63.0	69.9	73.8	72.9
100	51.5	56.0	56.8	61.9	58.8
80	36.2	42.3	40.7	41.3	45.6
	Torque [Nm]				

(b) Efficiency [%] for speed vs torque

Speed [rpm]	25	50	75	100	132
160	78.9	91.3	92.7	94.1	95.2
140	79.0	90.2	92.7	94.0	96.1
120	83.1	90.4	92.7	94.0	95.3
100	77.9	89.4	93.0	94.1	95.4
80	78.9	90.7	93.4	94.9	95.6
	Torque [Nm]				

Stellenbosch University https://scholar.sun.ac.za

Table 6.5 and 6.6 show the power losses and efficiencies for the two gears at an ambient temperature of 40°C, respectively. The efficiency of mechanical gear at rated torque and speed conditions once again hovers around the 95% mark while the efficiency of FMMG is slightly lower.

Table 6.6: Measured losses and efficiencies of the FMMG at different speeds and torques ($T_{ambient}$=40°C) (up-speed configuration)

(a) Power losses [W] for different speeds and torques

Speed [rpm]	25	50	75	100	132
160	152.7	154.9	153.6	153.5	152.4
140	137.6	137.2	138.1	138.2	138.0
120	111.0	113.8	112.5	112.7	113.2
100	92.2	93.5	91.9	89.8	148.2
80	99.1	99.4	98.2	99.1	102.0
	Torque [Nm]				

(b) Efficiency [%] for speed vs torque

Speed [rpm]	25	50	75	100	132
160	66.9	81.4	87.7	91.0	92.9
140	61.3	81.0	87.9	90.5	92.8
120	66.1	82.9	88.0	90.7	92.7
100	67.5	83.2	88.3	91.0	92.7
80	64.3	82.0	88.5	90.9	93.0
	Torque [Nm]				

The constructed efficiency maps of both gears for up-speed configuration at temperatures at $T_{ambient} = 40°C$ are shown in Figures 6.13 and 6.14.

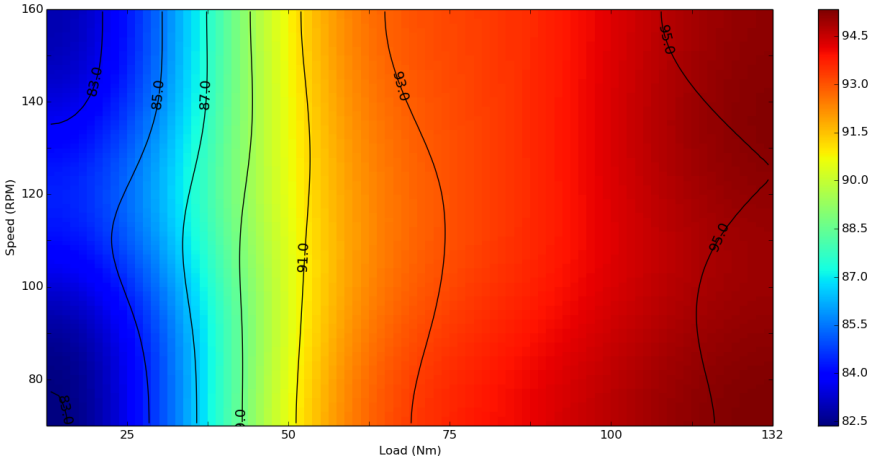

Figure 6.13: Efficiency heat map for up-speed mechanical gear test results at different torque loads and speeds ($T_{ambient} = 40°C$)

Stellenbosch University https://scholar.sun.ac.za

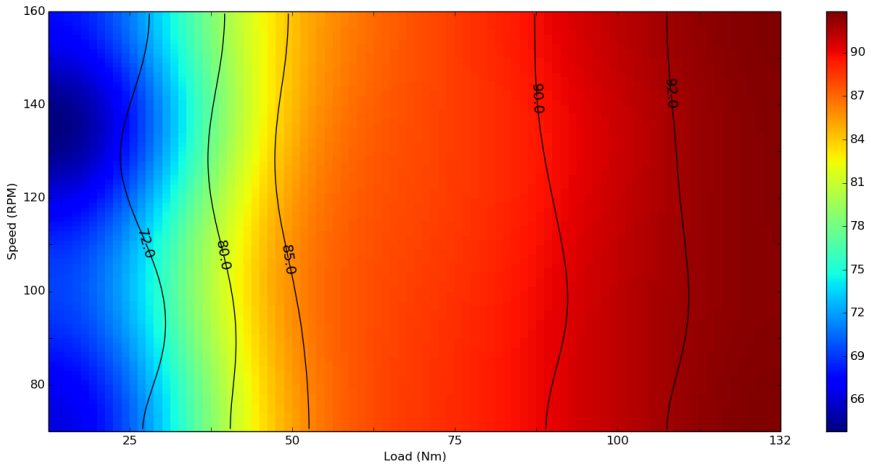

Figure 6.14: Efficiency heat map for up-speed FMMG test results at different torque loads and speeds ($T_{\text{ambient}} = 40°\text{C}$)

6.5 Peak torque measurement of FMMG

The peak torque measurement requires the gear shafts to be slipped out of sync. The test bench setup is shown in Figure 6.15. The high speed shaft of the gear is clamped in a frame shown on the left. The low speed shaft on the right is connected to an adjustable steel arm. The threaded rod allows the low speed shaft to be rotated in a controlled manner.

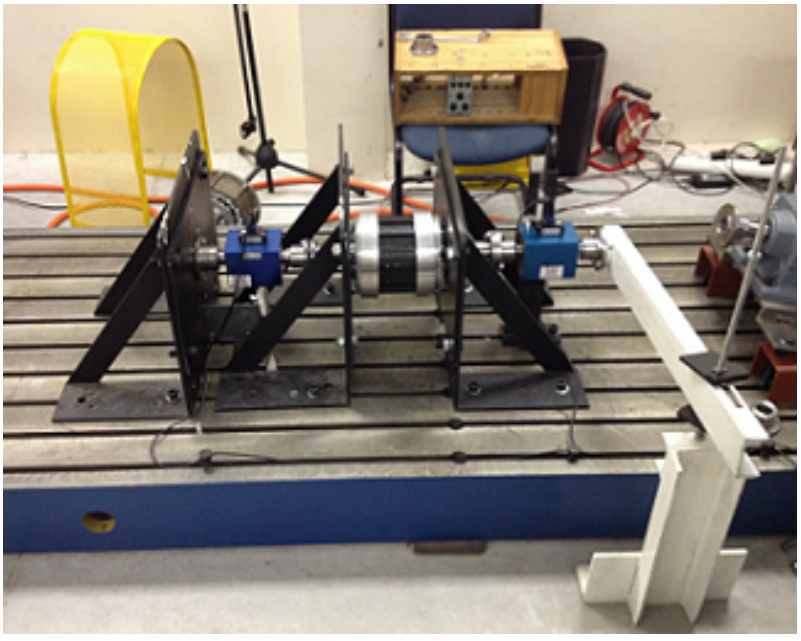

Figure 6.15: Test bench setup for peak torque measurement

Stellenbosch University https://scholar.sun.ac.za

The steel arm is adjusted until both torque sensors read zero. The nut beneath the arm is then turned upwards pushing the steel arm and rotating the shaft. The torque gradually increases until the peak point is reached. In Figure 6.16 the measured, 2D simulated and 3D simulated peak torque values are plotted. As expected the 2D simulation results are the highest at 294 Nm as 3D end effects are not taken into consideration. The 3D simulation results are much closer to the measured at 254 Nm. The measured peak torque results achieved a value of 243 Nm. This can be attributed to manufacturing tolerances and unaccounted losses and leakage in the gear.

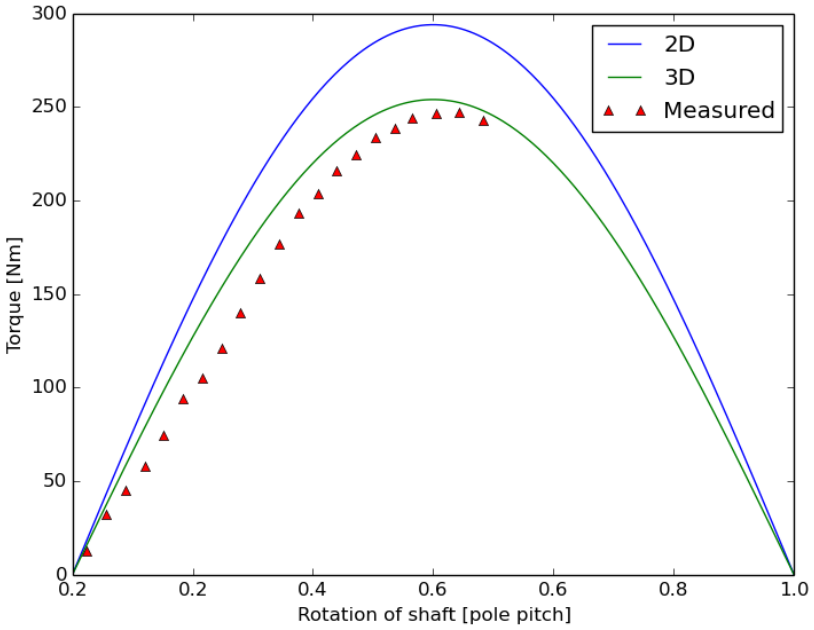

Figure 6.16: Peak torque measurement with 2D and 3D FE simulation values as reference

The peak torque output results for 2D and 3D FE simulations as well as measured results are shown in Table 6.7. The difference between the 2D and 3D FE results are 15.7% and as discussed in Chapter 3, the measured peak torque value is approximately 80% of the 2D peak torque output.

Table 6.7: Comparison of predicted and measured peak torque of FMMG ptototype

Source	Result [Nm]	difference [%]
2D simulated	294	-
3D simulated	254	15.7
Measured	243	20.9

Stellenbosch University https://scholar.sun.ac.za

6.6 Performance comparison

Apart from the mechanical issues identified on the testing of the MG, the gear performed generally well. The efficiency across all tests on average fell within 2% lower compared to the mechanical gear. Temperature has relatively little effect on the performance of the mechanical gear nor the magnetic gear at rated conditions. The magnetic gear merely experience a slight decreases in performance during rated conditions at higher temperatures.

The magnetic gear achieved a similar torque ripple on the output shaft compared to the mechanical gear although a much larger component is measured on the input shaft. Table 6.8 shows all test results at rated and 1.5 rated conditions.

Table 6.8: Performance summary of the gear test case

Type of test	Mechanical gear [%]	Magnetic gear [%]
Down speed (20°C)	95.2	93.5
Down speed (40°C)	94.9	93.7
Up speed (40°C)	95.7	92.8
Up speed (40°C)	95.2	92.9
1.5 pu torque (Down)	96.0	94.9
1.5 pu torque (Up)	95.7	95.0

Stellenbosch University https://scholar.sun.ac.za

Chapter 7

Conclusions and recommendations

In this thesis the design optimization and performance evaluation of a flux modulated magnetic gear has been presented. A magnetic gear prototype has been designed, manufactured and experimentally evaluated against an equivalent mechanical gear. The work covered in this thesis forms part of the investigation of alternative gear technology to address the frequently failing ACC mechanical gears. The main findings and conclusions of the work are summarized as follows:

- Among the most promising magnetic gear technologies to date, FMMG is mechanically least complex and can potentially realize both high torque density and high efficiency. Thus, it might be the MG technology that is closest to the commercial applications.
- The developed FMMG features a long stack length with bearing support from both sides. The flux modulator acts as low-speed rotor while the outer PM carrier serves as both mechanical earth and the casing of the FMMG. Despite the benefits these changes brought such as manufacturing cost saving as well as reduction of leakage flux induced losses in conductive casing material, some mechanical difficulties arose during the manufacturing phase.
- Owing to severe 3D end effects, a known issue of FMMG, there is a significant difference (about 17% in this case) between 2D and 3D FE predicted torque results. The measured stall torque of the FMMG is in good agreement with that of 3D FE (about 4% difference in this case).
- The FMMG prototype compares reasonably well with the equivalent mechanical gear in terms of efficiency under rated operating condition (93.5% vs 95.2%). The slightly less efficiency of FMMG may be attributed to relatively high mechanical loss.
- Both gears were tested in up-speed configuration to further investigate any differences in performance in the two technologies. Both gears show

Stellenbosch University https://scholar.sun.ac.za

reasonable efficiency performance. At a slightly elevated temperature, mechanical gear shows marginally improved efficiency, which is likely caused by the reduced friction of warmed up lubricants.

- The predicted electromagnetic losses of the FMMG (excluding mechanical losses) are around 30 W, which is significantly less than the measured no-load loss (190 W at 600 rpm). The larger than expected mechanical losses is believed to be responsible for this discrepancy. Difficulty in manufacturing accurate components as well as assembly of the components are likely the causes for the high mechanical losses.

7.1 Recommendations

The longer stack length of the gear increased any tolerances as was previously experienced from machining and manufacturing. The previous small FMMG prototype modulator with a 40 mm stack length was easily machinable and centred from the casing allowing near perfect placement. The new 100 mm stack length modulator/low speed shaft supported from both side required alignment with a mould and perfect machining and assembly. Even after machining the component experienced vibration during operation caused by unbalanced and off-centre alignment. It is recommended that the entire modulator assemble process receives a design revisit to address the problem which arose in this study.

The laminations used to form the PM carrier yoke requires compression from threaded rods in order to function correctly and to be structurally stable. The tolerances experienced in the laser cutting, the channels in the yoke for the rods to penetrate the PM carrier as well as the compression rings used between the laminations caused mechanical issues. This resulted in the PM carrier magnets and the modulator to interfere with one another. Two aluminium rings were manufactured and pressed around the casings and laminations to align the components. Although this was a successful modification, it is recommended to tighten tolerances or redesign alignment jigs in the future to avoid re-occurrence of the problem.

The magnet segmentation has been implemented in the design in an attempt to reduce the eddy current loss in the PMs. While this is an effective measure for PM loss reduction, its impact on the core loss, torque rating and torque quality should be investigated. The torque ripple of the FMMG is high, which is not ideal from the operation perspective. Future design improvements are required.

Stellenbosch University https://scholar.sun.ac.za

List of References

[1] Nave, R.: Heat engine cycle. [Online]. Available: http://hyperphysics.phy-astr.gsu.edu/hbase/thermo/heaeng.html#c1 [accessed 2016].

[2] Kuma: Difference between first and second law of thermodynamics. Available [online] : http://pediaa.com/difference-between-first-and-second-law-of-thermodynamics.

[3] Wandrei, K.: What are some everyday examples of the first and second laws of thermodynamics? [Online]. Available: http://education.seattlepi.com/everyday-examples-first-second-laws-thermodynamics-4740.html [accessed 2016].

[4] Kapooria, R.K., Kumar, S. and Kasana, K.S.: An analysis of a thermal power plant working on a rankine cycle: A theoretical investigation. *Journal of Energy in Southern Africa*, vol. 19, no. 1, 2008.

[5] Raiz, S., Chapman, A.C. and Verbic, G.: Evaluation of concentrated solar-thermal generation for provision of power system flexibility. *Power Systems Computation Conference (PSCC)*, 2016.

[6] Xu, T. and Zhang, N.: Coordinated operation of concentrated solar power and wind resources for the provision of energy and reserve services. *IEEE Transactions on Power Systems*, 2016.

[7] Higher Education Technology (Ecatepec): Tecnologico de estudios superiores de ecatepec. [Online]. Available: http://www.tese.edu.mx/tese2010/loader_gallery.aspx?n=UTWXOSNY&i_d=0 [accessed 2016], 2016.

[8] U.S. Energy Information Administration: Concentrating solar power technologies offer utility-scale power production. [Online]. Available: http://www.eia.gov/todayinenergy/detail.cfm?id=530 [accessed 2016], 2011.

[9] Simbolotti, G.: Concentrating solar power technology brief. *IEA-ETSAP and IRENAÂ© Technology Brief E1*, 2013.

[10] Shi, L., Wang, J., Shi, C. and Wu, X.: Numerical investigation of influence on heat transfer performance of direct air cooled condenser under different wind directions. *International Joint Conference on Computational Sciences and Optimization*, 2009.

Stellenbosch University https://scholar.sun.ac.za

[11] Zhao, W. and Liu, P.: The influence of thermal flow field on recirculation of air-cooled tower for a large power plant. In: *Asia-Pacific Power and Energy Engineering Conference (APPEEC)*. 2011.

[12] Spig: Air cooled condensers. [Online]. Available: `http://www.spig-int.com/core-activities/air-cooled-condensers/air-cooled-condensers.html` [accessed 2016], 2016.

[13] POWERMAG: Air-cooled condensers eliminate plant water use. [Online]. Available: `http://www.powermag.com/air-cooled-condensers-eliminate-plant-water-use` [accessed 2015], 2008.

[14] Goldschagg, H.: Acc fan gearboxes: Eskom's experience in selection and maintenance of acc gearboxes. In: *ACCUG Navada conference*. 2013.

[15] Eskom Holdings: Matimba power station - the bushvled giant. [Online]. Available: `http://www.eskom.co.za/sites/heritage/Pages/Matimba-Power-Station.aspx` [accessed 2016], 2016.

[16] Shaltout, A.: Analysis of torsional torques in starting of large squirrel cage induction motors. *IEEE Transactions on Energy Conversion*, vol. 9, 1994.

[17] Zenginobuz, G., Cadirci, I., Ermis, M. and Barlak, C.: Soft starting of large induction motors at constant current with minimized starting torque pulsations. *IEEE Transactions on Industry Applications*, vol. 5, 2001.

[18] Li, Y., Tang, D., Zhang, J. and Wen, J.: An experimental study of pulsatile airflow in the fan inlet of an air-cooling heat exchanger using power spectrum analysis. *Power Engineering and Automation Conference (PEAM)*, vol. 1, pp. 138–141, 2011.

[19] Liu, P. and Zhao, W.: Effect of wind on recirculation of direct air-cooled condenser for a large power plant. *Asia-Pacific Power and Energy Engineering Conference*, pp. 1–4, 2009.

[20] Parey, A., Jain, N.K. and Koria, S.C.: Failure analysis of air cooled condenser gearbox. [Online]. Available: `http://www.sciencedirect.com/science/article/pii/S2213290214000200` [accessed 2016], 2016.

[21] Gerber, S.: *Evaluation and Design Aspects of Magnetic Gears and Magnetically Geared Electrical Machines*. PhD Dissertation, University of Stellenbosch, 2015.

[22] Tlali, P.M., Wang, R.J. and Gerber, S.: Magnetic gear technologies: A review. In: *International Conference on Electrical Machines (ICEM), Berlin*, pp. 544–550. September 2014.

[23] Baermann, M.: Magnetic worm drive. [Online]. Available: `https://www.google.com/patents/US3814962` [accessed 2016], 1974. US Patent 3,814,962.

Stellenbosch University https://scholar.sun.ac.za

[24] Linni, J.: *Design, Analysis and Application of Coaxial Magnetic Gears.* PhD Dissertation, The University of Hong Kong, 2010.

[25] Atallah, K. and Howe, D.: A novel high-performance magnetic gear. *IEEE Transactions on Magnetics*, vol. 37, no. 4, pp. 2844–2846, 2001.

[26] Huang, C., Tsai, M. and Dorrell, D. nad Lin, B.: Development of a magnetic planetary gearbox. *IEEE Transactions on Magnetics*, vol. 44, no. 3, pp. 403–412, 2014.

[27] Davey, K., Hutson, T., Mcdonald, L., Ras, C., Weinstein, R., Parks, D. and Sawh, R.P.: Rotating cylinder planetary gear motor. *IEEE Transactions on Industry Applications*, vol. 52, no. 3, pp. 2253–2260, 2016.

[28] Niguchi, N. and Hirata, K.: Transmission torque analysis of a novel magnetic planetary gear employing 3-d fem. *IEEE Transactions on Magnetics*, vol. 48, no. 2, 2012.

[29] Wang, R.J., Matthee, A., Gerber, S. and Tlali, P.: Calculation of torque performance of a novel magnetic planetary gear. *IEEE Magnetics Letters*, vol. 7, 2016.

[30] Gouda, E., Mezani, S., Baghli, L. and Rezzoug, A.: Comparative study between mechanical and magnetic planetary gears. *IEEE Transactions on Magnetics*, vol. 47, no. 2, 2011.

[31] Rens, J., Atallah, K., Calverly, S.D. and Howe, D.: A novel magnetic harmonic gear. *IEEE Int. Electric Machines Drives Conf. (IEMDC)*, vol. 1, pp. 698–703, 2007.

[32] Rens, J., Clark, R., Calverly, S., Atallah, K. and Howe, D.: Design, analysis and realization of a novel magnetic harmonic gear. *International Conference on Electrical Machines*, pp. 1–4, 2008.

[33] Rens, J., Atallah, K., Calverly, S. and Howe, D.: A novel magnetic harmonic gear. *IEEE Transaction on industry applications*, vol. 46, no. 1, 2010.

[34] Rens, J., Atallah, K., Calverly, S. and Howe, D.: A novel magnetic harmonic gear. *IEEE Transactions on Industry Applications*, vol. 46, no. 1, 2010.

[35] Windpower: How are gears and gearboxes used in wind turbines. [Online]. Available: `http://www.windpowerengineering.com/design/mechanical/how-are-gears-gearboxes-used-in-wind-turbines/` [accessed 2015], 2011.

[36] Gerber, S. and Wang, R.J.: Evaluation of a prototype magnetic gear. In: *IEEE International Conference on Industrial Technology, (ICIT), Cape Town*, pp. 319–324. February 2013.

[37] Pellerey, P., Favennec, G., Lanfranchi, V. and Friedrich, G.: Active reduction of electrical machines magnetic noise by the control of low frequency current harmonics. In: *IECON 2012 - 38th Annual Conference on IEEE Industrial Electronics Society*, pp. 1654–1659. 2012.

Stellenbosch University https://scholar.sun.ac.za

[38] Matthee, A., Gerber, S. and Wang, R.J.: A high performance concentric magnetic gear. In: *Southern African Universities Power Engineering Conference, (SAUPEC), Johannesburg*, pp. 203–207. January 2015.

[39] Atallah, K., Calverley, S. and Howe, D.: Design, analysis and realisation of a high-performance magnetic gear. *IEEE Electric Power Applications*, vol. 151, no. 2, pp. 135–143, 2004.

[40] Rens, J., Calverly, S., Atallah, K. and Howe, D.: A novel magnetic harmonic gear. *IEEE International Electric Machines and Drives Conference*, vol. 1, pp. 698–703, 2007.

[41] Niguchi, N., Hirate, K. and Sakai, M.: High performance hybrid-type magnetic planetary gear. In: *IEEE Internation conference on Mechatronics and Automation*. 2013.

[42] Davey, K., McDonald, L. and Hutson, T.: Axial flux cycloidal magnetic gears. *IEEE Transactions on Magnetics*, vol. 50, no. 4, 2014.

[43] Zhu, D., Yang, F. and Du, Y.: An axial-field flux-modulated magnetic gear. *IEEE Transactions on Applied Superconductivity*, vol. 26, no. 4, 2016.

[44] Gill, H.: Cogging and torque ripple questions. [Online]. Available: `http://www.kollmorgen.com/en-us/blogs/_blog-in-motion/articles/hurley-gill/cogging-and-torque-ripple-questions/`[accessed 2016], 2013.

[45] Piccoli, M. and Yim, M.: Cogging torque ripple minimization via position-based characterization.

[46] Zhu, Z.Q. and Howe, D.: Influence of design parameters on cogging torque in permanent magnet machines. *IEEE Transactions on Magnetics*, vol. 15, no. 4, pp. 407–412, 2000.

[47] McGraw-Hill: Dictionary of scientific and technical terms "leakage flux". [Online]. Available: `http://encyclopedia2.thefreedictionary.com/leakage+flux` [accessed 2016], 2016.

[48] Frandsen, T.V. and Rasnussen, P.O.: Slip torque investigation and magnetic redesign of motor integrated permanent magnet gear. In: *International Conference on ELectrical Machines and Systems (ICEMS)*. 2015.

[49] Allegro: Guidelines for designing a concentrator for high-current sensing applications with an allegro hall-effect sensor ic. [Online]. Available: `http://www.allegromicro.com/en/Design-Center/Technical-Documents/Hall-Effect-Sensor-IC-Publications/Current-Sensor-Concentrator.aspx` [accessed 2016], 2016.

[50] Nair, S.S., Wang, J., Chen, L., Chin, R., Manolas, I. and Svechkarenko, D.: Prediction of 3-d high-frequency eddy current loss in rotor magnets of spm machines. *IEEE Transactions on Magnetics*, vol. 52, no. 9, 2016.

Stellenbosch University https://scholar.sun.ac.za

[51] Brönn, L., Wang, R.J. and Kamper, M.J.: Development of a shutter type magnetic gear. In: *Southern African Universities Power Engineering Conference SAUPEC*. 2010.

[52] JMAG: High-speed magnet eddy current calculation. [Online]. Available: `https://www.jmag-international.com/products/jmag-designer/magnetic_field.html` [accessed 2016], 2016.

[53] Brittanica, E.: Hysteresis. [Online]. Available: `https://global.britannica.com/science/hysteresis` [accessed 2016], 2016.

[54] Hyperphysics: Coercivity and remanence in permanent magnets. [Online]. Available: `http://hyperphysics.phy-astr.gsu.edu/hbase/solids/magperm.html` [accessed 2016], 2016.

[55] Sandstrom, R. and Helene, L.: Hard magnetic materials. Seminar on Functional materials (Course: 4H1609), 2002.

[56] Bacha, G.E., Milano, S. and Viola, S.: Hysteresis mitigation in current sensor ics using ferromagnetic cores. 2014.

[57] Hysteresis. [Online]. Available: `http://www.tpub.com/neets/book5/15g.htm` [accessed 2016], 2016.

[58] Wrobel, R., Vainel, G. and Copeland, C.: Investigation of mechanical loss components and heat transfer in an axial-flux pm machine. *IEEE Transactions on Industry Applications*, vol. 51, no. 4, 2015.

[59] Yang, R., Kang, J., Zhao, J., Li, J. and Li, H.: A case study of bearing condition monitoring using spm. *Prognostics and System Health Management Conference (PHM-2014 Hunan)*, vol. 51, no. 4, 2014.

[60] Liu, H.P., Hearn, C.S., Werst, M.D., Hahne, J.J. and Bogard, D.: Splits of windage losses in integrated transient rotor and stator thermal analysis of a highspeed alternator during multiple discharges. In: *12th Symposium on Electromagnetic Launch Technology*. 2004.

[61] Clarke, R.: Magnetic properties of materials. [Online]. Available: `http://info.ee.surrey.ac.uk/Workshop/advice/coils/mu/` [accessed 2016], 2008.

[62] What-When-How: Applications (magnetic properties of materials) part 1. [Online]. Available: `http://what-when-how.com/electronic-properties-of-materials/applications-magnetic-properties-of-materials-part-1` [accessed 2016], 2014.

[63] Liu, J.: Some design considerations using permanent magnets. [Online]. Available: `http://www.magneticsmagazine.com/main/articles/some-design-considerations-using-permanent-magnets/`, 2016.

Stellenbosch University https://scholar.sun.ac.za

[64] Liu, J.F. and Walmer, M.H.: Thermal stability and performance data for sm-co 2:17 high temperature magnets on ppm focusing structures. In: *Fifth IEEE International Vacuum Electronics Conference, (IVEC)*. 2004.

[65] Li, S., Sarlioglu, B., Jurkovic, S., Patel, N. and Savagian, P.: Evaluation of torque compensation control algorithm of ipm machines considering the effects of temperature variations. *Transportation Electrification Conference and Expo (ITEC)*, 2016.

[66] Tlali, P., Gerber, S. and Wang, R.J.: Optimal design of an outer-stator magnetically geared permanent magnet machine. *IEEE Transactions on Magnetics*, vol. 52, 2016.

[67] Gerber, S. and Wang, R.J.: Analysis of the end-effects in magnetic gears and magnetically geared machines. In: *Electrical Machines (ICEM), 2014 International Conference on*, pp. 396–402. Sept 2014.

[68] SEW: Helical gearmotor r series. [Onli ne]. Available:`http://ww2.sew-eurodrive.com/produkt/helical-gearmotor-r-series.htm` [accessed 2016], 2016.

[69] Ruoho, S., Ikäheimo, J. and Arkkio, A.: Interdependence of demagnetization, loading, and temperature rise in a permanent-magnet synchronous motor. *IEEE Transactions on Magnetics*, vol. 46, no. 3, 2010.

[70] Casadei, D., Mengoni, M., Serra, G., Tani, A. and Zarri, L.: Behavior of a five-phase surface-mounted permanent magnet motor under magnet demagnetization. In: *IEEE International Symposium on Diagnostics for Electric Machines, Power Electronics and Drives (SDEMPED)*. 2011.

[71] Casadei, D., Filippetti, F., Mengoni, M., Gritli, Y., Serra, G., Tani, A. and Zarri, L.: Detection of magnet demagnetization in five-phase surface-mounted permanent magnet generators. In: *IEEE International Symposium on Power Electronics for Distributed Generation Systems (PEDG)*. 2013.

[72] Department, C.U.E.: Materials data book. [Online]. Available: `http://www-mdp.eng.cam.ac.uk/web/library/enginfo/cueddatabooks/materials.pdf` [accessed 2016], 2003.

[73] TUFNOL composites limited: Thermoplastic materials for engineering components. [Online]. Available: `http://www.tufnol.com/materials-full/thermoplastic-full.aspx` [accessed 2016], 2003.

[74] Budynas, R.G. and Nisbett, J.K.: *Shigley's Mechanical engineering design, Ninth edition*. McGraw-Hill 2008, Sept 2011.

Stellenbosch University https://scholar.sun.ac.za

Appendices

Stellenbosch University https://scholar.sun.ac.za

Harmonic order calculation

The radial magnetic field in the air-gap adjacent to the LS rotor of an FMMG may be expressed by Equation (2.6), where P_h is the number of PM pole pairs on the HS rotor, N_s the number of segments on the stator (Modulator), Ω_r and Ω_s are the speed of the rotor and stator, respectively:

$$B_r(r,\theta) = \sum_{m=1,3,5...} b_{rm}(r)cos(mP_h(\theta - \Omega_r t) + mP_h\theta_0) \times (\lambda_{r0}(r) + \sum_{j=1,3,5...} \lambda_{rj}(r)cos(jN_s(\theta - \Omega_s t))) \tag{1}$$

using identity:

$$cosacosb = \frac{1}{2}[cos(a-b) + cos(a+b)]$$

with

$$a = mP_h(\theta - \Omega_s t) + mP_h\theta_0$$
$$b = jN_s(\theta - \Omega_s t)$$

Rearranging these terms into the following:

$$\begin{aligned} a + b =& jN_s(\theta - \Omega_s t) + mP_h(\theta - \Omega_r t) + mP_h\theta_0 \\ &= jN_s\theta - jN_s\Omega_s t + mP_h\theta - mP_h\Omega_r t + mP_h\theta_0 \\ &= jN_s\theta + mP_h\theta - jN_s\Omega_s t - mP_h\Omega_r t + mP_h\theta_0 \\ &= \theta(jN_s + mP_h) - jN_s\Omega_s t - mP_h\Omega_r t + mP_h\theta_0 \\ &= (jN_s + mP_h)(\theta - \frac{jN_s\Omega_s t + mP_h\Omega_r t}{jN_s + mP_h}) + mP_h\theta_0 \end{aligned} \tag{2}$$

and:

$$\begin{aligned} a - b =& -jN_s(\theta - \Omega_s t) + mP_h(\theta - \Omega_r t) + mP_h\theta_0 \\ &= -jN_s\theta + jN_s\Omega_s t + mP_h\theta - mP_h\Omega_r t + mP_h\theta_0 \\ &= -jN_s\theta + mP_h\theta + jN_s\Omega_s t - mP_h\Omega_r t + mP_h\theta_0 \\ &= \theta(mP_h - jN_s) - (mP_h\Omega_r t - jN_s\Omega_s t) + mP_h\theta_0 \\ &= (mP_h - jN_s)(\theta - \frac{mP_h\Omega_r t - jN_s\Omega_s t}{mP_h - jN_s}) + mP_h\theta_0 \end{aligned} \tag{3}$$

and substituting back into the formula:

Stellenbosch University https://scholar.sun.ac.za

$$B_r(r,\theta) = \lambda_{r0} \sum_{m=1,3,5} b_{rm}(r)cos(mP_h(\theta - \Omega_r t) + mp\theta_0) + \frac{1}{2}[$$
$$\sum_{m=1,3,5} \sum_{j=1,3,5} \lambda_{rj}(r)B_{rm}(r)cos((mP_h + jn_s)(\theta - \frac{jn_s\Omega_s t + mP_h\Omega_r t}{mP_h + jn_s}) + mP_h\theta_0) +$$
$$\sum_{m=1,3,5} \sum_{j=1,3,5} \lambda_{rj}(r)B_{rm}(r)cos((mP_h - jn_s)(\theta - \frac{mP_h\Omega_r t - jN_s\Omega_s t}{mP_h - jN_s}) + mp\theta_0)] \tag{4}$$

With the modulator stationary the speed $\Omega_s = 0$. Equation (5) proves that the flux waveform produced by the HS and LS have a space harmonic flux waveform given by [39]:

$$\begin{aligned} P_{mk} &= |mP_h + kN_s| \\ m &= 1, 3, 5, ...\infty \\ k &= 0, \pm 1, \pm 2, \pm 3, ... \pm \infty \end{aligned} \tag{5}$$

with m = 1 and k = -1 producing the largest flux harmonic field. With N_s = 15 and P_h = 4 the resultant harmonic order is:

$$\begin{aligned} P_{mk} &= |mP_h + kN_s| \\ P_{1,-1} &= |(1)(4) + (-1)(15)| \\ &= 11 \end{aligned} \tag{6}$$

Stellenbosch University https://scholar.sun.ac.za

HS shaft stress analysis

13 Sep 2016 08:10:05 - HS_Shaft.sm

Force and Stress analysis on high speed shaft

The critical area on this shaft was taken at the end where the shaft diameter is the smallest and the key stress concentration is present. Furthermore, the calculation was done for pure torsional force, as stated previously in the bolt calculations.

Section details:

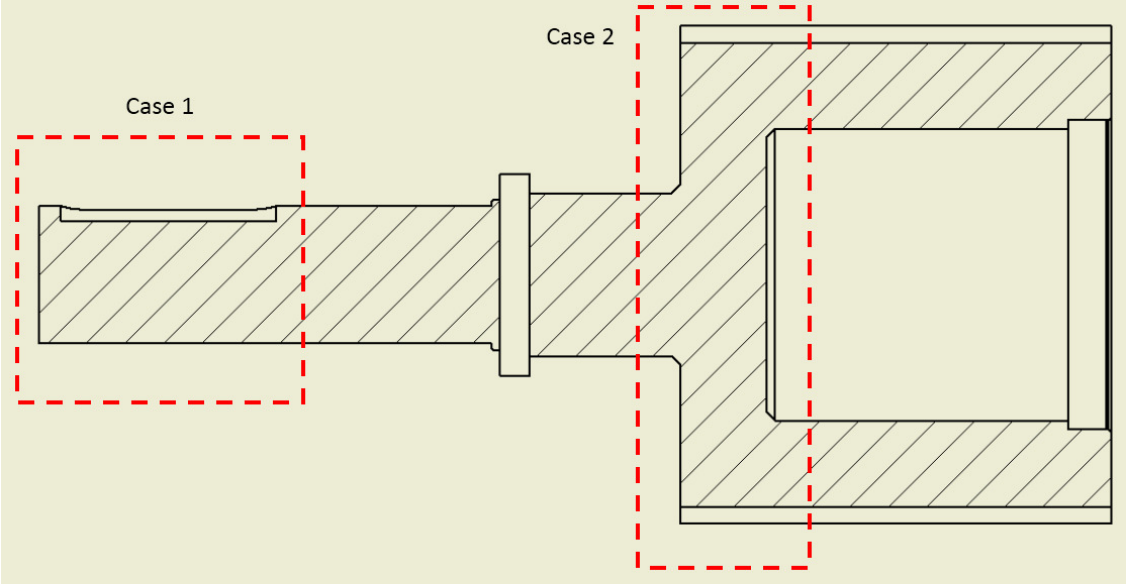

Case 1:

$Torque := 88.5\ N\ m$ Torque from simulation

$OD_4 := 32\ mm$ $ID_4 := 0\ mm$

$K_{t\_z} := 2.7$ $K_{ts\_z} := 2.2$ Read from table 7-1

Worst Case if sharp corner is machined

$M_{max\_z} := 0 = 0\ N\ m$ $M_{min\_z} := 0 = 0\ N\ m$

$M_{m\_z} := \frac{M_{max\_z} + M_{min\_z}}{2} = 0\ N\ m$ $M_{a\_z} := \frac{M_{max\_z} - M_{min\_z}}{2} = 0\ N\ m$

$I_z := \frac{\pi}{64} \cdot \left(OD_4^{\,4} - \left(ID_4 \right)^4 \right) = 5.1472 \cdot 10^{-8}\ m^4$

Stellenbosch University https://scholar.sun.ac.za

$$\sigma_{m\_z} := \frac{M_{m\_z} \cdot \frac{OD_4}{2}}{I_z} = 0 \qquad \sigma_{a\_z} := \frac{M_{a\_z} \cdot \frac{OD_4}{2}}{I_z} = 0\ MPa$$

Assuming that the electric motor runs at full speed in reverse shows that the maximum and minimum torque is the positive and negative torque.

$$T_{max\_z} := Torque = 88.5\ N\,m \qquad T_{min\_z} := -0 = 0\ N\,m$$

$$T_{m\_z} := \frac{T_{max\_z} + T_{min\_z}}{2} = 44.25\ N\,m \qquad T_{a\_z} := \frac{T_{max\_z} - T_{min\_z}}{2} = 44.25\ N\,m$$

$$J_{G\_z} := 2 \cdot I_z = 1.0294 \cdot 10^{-7}\ m^4$$

$$\tau_{m\_z} := \frac{T_{m\_z} \cdot \frac{OD_4}{2}}{J_{G\_z}} = 6.8775\ MPa \qquad \tau_{a\_z} := \frac{T_{a\_z} \cdot \frac{OD_4}{2}}{J_{G\_z}} = 6.8775\ MPa$$

$$\sigma'_{m\_z} := \sqrt{\left(K_{t\_z} \cdot \sigma_{m\_z}\right)^2 + 3 \cdot \left(K_{ts\_z} \cdot \tau_{m\_z}\right)^2} = 26.207\ MPa$$

$$\sigma'_{a\_z} := \sqrt{\left(K_{t\_z} \cdot \sigma_{a\_z}\right)^2 + 3 \cdot \left(K_{ts\_z} \cdot \tau_{a\_z}\right)^2} = 26.207\ MPa$$

Material Properties (EN 8) Mild Steel

$S_y := 280\ MPa$ $S_{ut} := 550\ MPa$ $E := 200\ GPa$ (Table A-20 Shigley)

Using the Marin equation to calculate the endurance limit at the various critical points on the shaft.

Estimate the endurance limit:

if $S_{ut} \le 1400\ MPa$

$S'_e := 0.5 \cdot S_{ut}$ (eqn. 6-8)

else

$S'_e := 1400\ MPa$

$S'_e = 275\ MPa$

Surface condition modification factor:

$a := 4.51$ $b := -0.265$ Read from table 6-2 for Machined or cold-drawn

$$k_a := a \cdot \left(\frac{S_{ut}}{1\ MPa}\right)^b = 0.8472$$ (eqn. 6-19)

Stellenbosch University https://scholar.sun.ac.za

Size modification factor:

$$k_{b\_z} := 1.24 \cdot \left(\frac{OD_4}{1\ mm}\right)^{-0.107} = 0.8558$$ (eqn. 6-20)

Load modification factor:

$$k_c := 0.59$$ (eqn. 6-26)

Reliability factor:

Read from table 6-5 for 99.99% reliability

Marin equation for endurance limit:

$$k_e := 0.897$$ (eqn. 6-18)

$$S_{e\_z} := k_a \cdot k_{b\_z} \cdot k_c \cdot k_e \cdot S'_e = 105.5184\ MPa$$

Use the modified-Goodman equation to determine the safety factor for each section:

Section z:

$$n_z := \frac{1}{\frac{\sigma'_{a\_z}}{S_{e\_z}} + \frac{\sigma'_{m\_z}}{S_{ut}}} = 3.3782$$ (eqn. 6-46)

The safety factor for yield design is given above, this is more realistic. This is a considered a high safety factor, the diameter was chosen according to coupling size.

Case 2:

$Torque := 88.5\ N\ m$ Torque from simulation

$OD_4 := 104\ mm$ $ID_4 := 73\ mm$

$K_{t\_z} := 2.7$ $K_{ts\_z} := 2.2$ Read from table 7-1

Worst Case if sharp corner is machined

$M_{max\_z} := 0 = 0\ N\ m$ $M_{min\_z} := 0 = 0\ N\ m$

$$M_{m\_z} := \frac{M_{max\_z} + M_{min\_z}}{2} = 0\ N\ m$$ $$M_{a\_z} := \frac{M_{max\_z} - M_{min\_z}}{2} = 0\ N\ m$$

Stellenbosch University https://scholar.sun.ac.za

$$I_z := \frac{\pi}{64}\cdot\left(OD_4^{\,4} - \left(ID_4\right)^4\right) = 4.3485\cdot 10^{-6}\ m^4$$

$$\sigma_{m\_z} := \frac{M_{m\_z}\cdot\frac{OD_4}{2}}{I_z} = 0 \qquad \sigma_{a\_z} := \frac{M_{a\_z}\cdot\frac{OD_4}{2}}{I_z} = 0\ MPa$$

Assuming that the electric motor runs at full speed in reverse shows that the maximum and minimum torque is the positive and negative torque.

$$T_{max\_z} := Torque = 88.5\ N\,m \qquad T_{min\_z} := -0 = 0\ N\,m$$

$$T_{m\_z} := \frac{T_{max\_z} + T_{min\_z}}{2} = 44.25\ N\,m \qquad T_{a\_z} := \frac{T_{max\_z} - T_{min\_z}}{2} = 44.25\ N\,m$$

$$J_{G\_z} := 2\cdot I_z = 8.6971\cdot 10^{-6}\ m^4$$

$$\tau_{m\_z} := \frac{T_{m\_z}\cdot\frac{OD_4}{2}}{J_{G\_z}} = 0.2646\ MPa \qquad \tau_{a\_z} := \frac{T_{a\_z}\cdot\frac{OD_4}{2}}{J_{G\_z}} = 0.2646\ MPa$$

$$\sigma'_{m\_z} := \sqrt{\left(K_{t\_z}\cdot\sigma_{m\_z}\right)^2 + 3\cdot\left(K_{ts\_z}\cdot\tau_{m\_z}\right)^2} = 1.0082\ MPa$$

$$\sigma'_{a\_z} := \sqrt{\left(K_{t\_z}\cdot\sigma_{a\_z}\right)^2 + 3\cdot\left(K_{ts\_z}\cdot\tau_{a\_z}\right)^2} = 1.0082\ MPa$$

Material Properties (EN 8) Mild Steel

$S_y := 280\ MPa$ $S_{ut} := 550\ MPa$ $E := 200\ GPa$ (Table A-20 Shigley)

Using the Marin equation to calculate the endurance limit at the various critical points on the shaft.

Estimate the endurance limit:

if $S_{ut} \le 1400\ MPa$

$S'_e := 0.5\cdot S_{ut}$ (eqn. 6-8)

else

$S'_e := 1400\ MPa$

$$S'_e = 275\ MPa$$

Surface condition modification factor:

$a := 4.51$ $b := -0.265$ Read from table 6-2 for Machined or cold-drawn

Stellenbosch University https://scholar.sun.ac.za

$$k_a := a \cdot \left(\frac{S_{ut}}{1\ MPa} \right)^b = 0.8472$$ (eqn. 6-19)

Size modification factor:

$$k_{b\_z} := 1.24 \cdot \left(\frac{OD_4}{1\ mm} \right)^{-0.107} = 0.7544$$ (eqn. 6-20)

Load modification factor:

$$k_c := 0.59$$ (eqn. 6-26)

Reliability factor:

Read from table 6-5 for 99.99% reliability

Marin equation for endurance limit:

$$k_e := 0.897$$ (eqn. 6-18)

$$S_{e\_z} := k_a \cdot k_{b\_z} \cdot k_c \cdot k_e \cdot S'_e = 93.0158\ MPa$$

Use the modified-Goodman equation to determine the safety factor for each section:

Section z:

$$n\_z := \frac{1}{\frac{\sigma'_{a\_z}}{S_{e\_z}} + \frac{\sigma'_{m\_z}}{S_{ut}}} = 78.917$$ (eqn. 6-46)

The safety factor for yield design is given above, this is extremely high. However, this was not the critical case and did not have a direct impact on the design.

Stellenbosch University https://scholar.sun.ac.za

LS shaft stress analysis

13 Sep 2016 08:12:30 - LS_Shaft.sm

Force and Stress analysis on low speed shaft

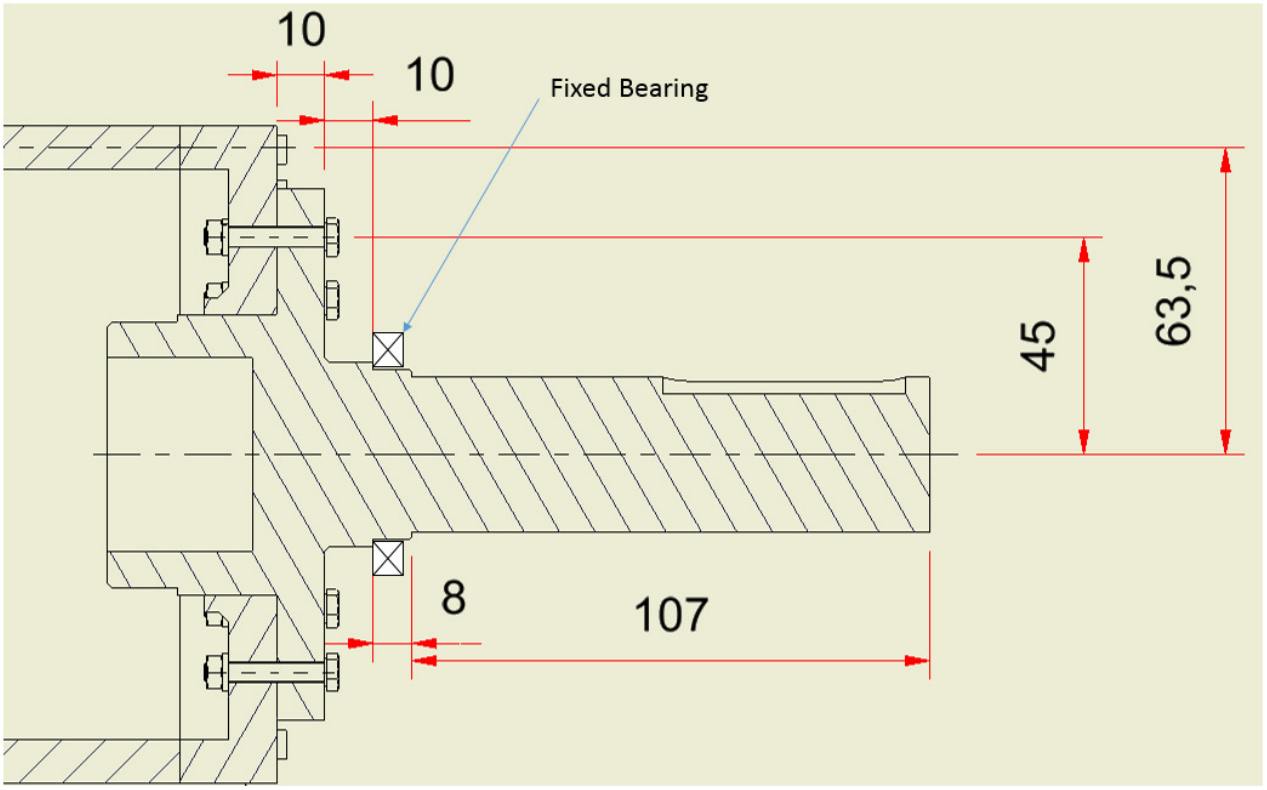

The critical area on this shaft was taken at the end where the shaft diameter is the smallest and the key stress concentration is present. Furthermore, the calculation was done for pure torsional force, as stated previously in the bolt calculations.

Section details

$Torque := 265\ N\ m$ Torque from simulation

$OD_4 := 32\ mm$

$K_{t\_z} := 2.7$

$K_{ts\_z} := 2.2$

Read from table 7-1

Worst Case if sharp corner is machined

$M_{max\_z} := 0 = 0\ N\ m$

$M_{min\_z} := 0 = 0\ N\ m$

$M_{m\_z} := \frac{M_{max\_z} + M_{min\_z}}{2} = 0\ N\ m$

$M_{a\_z} := \frac{M_{max\_z} - M_{min\_z}}{2} = 0\ N\ m$

Stellenbosch University https://scholar.sun.ac.za

$$I_z := \frac{\pi}{64}\cdot\left(OD_4^{\,4}\right) = 5.1472\cdot 10^{-8}\ m^4$$

$$\sigma_{m\_z} := \frac{M_{m\_z}\cdot\frac{OD_4}{2}}{I_z} = 0 \qquad \sigma_{a\_z} := \frac{M_{a\_z}\cdot\frac{OD_4}{2}}{I_z} = 0\ MPa$$

Assuming that the electric motor runs at full speed in reverse shows that the maximum and minimum torque is the positive and negative torque.

$$T_{max\_z} := Torque = 265\ N\,m \qquad T_{min\_z} := -0 = 0\ N\,m$$

$$T_{m\_z} := \frac{T_{max\_z} + T_{min\_z}}{2} = 132.5\ N\,m \qquad T_{a\_z} := \frac{T_{max\_z} - T_{min\_z}}{2} = 132.5\ N\,m$$

$$J_{G\_z} := 2\cdot I_z = 1.0294\cdot 10^{-7}\ m^4$$

$$\tau_{m\_z} := \frac{T_{m\_z}\cdot\frac{OD_4}{2}}{J_{G\_z}} = 20.5938\ MPa \qquad \tau_{a\_z} := \frac{T_{a\_z}\cdot\frac{OD_4}{2}}{J_{G\_z}} = 20.5938\ MPa$$

$$\sigma'_{m\_z} := \sqrt{\left(K_{t\_z}\cdot\sigma_{m\_z}\right)^2 + 3\cdot\left(K_{ts\_z}\cdot\tau_{m\_z}\right)^2} = 78.4728\ MPa$$

$$\sigma'_{a\_z} := \sqrt{\left(K_{t\_z}\cdot\sigma_{a\_z}\right)^2 + 3\cdot\left(K_{ts\_z}\cdot\tau_{a\_z}\right)^2} = 78.4728\ MPa$$

Material Properties (EN 19) Mild Steel

$S_y := 495\ MPa$ $S_{ut} := 700\ MPa$ $E := 200\ GPa$ (Table A-20 Shigley)

Using the Marin equation to calculate the endurance limit at the various critical points on the shaft.

Estimate the endurance limit:

if $S_{ut} \le 1400\ MPa$

$S'_e := 0.5\cdot S_{ut}$ (eqn. 6-8)

else

$S'_e := 1400\ MPa$

$S'_e = 350\ MPa$

Stellenbosch University https://scholar.sun.ac.za

Surface condition modification factor:

$a := 4.51$ $b := -0.265$

Read from table 6-2 for Machined or cold-drawn

$$k_a := a \cdot \left(\frac{S_{ut}}{1\ MPa} \right)^b = 0.7947$$ (eqn. 6-19)

Size modification factor:

$$k_{b\_z} := 1.24 \cdot \left(\frac{OD_4}{1\ mm} \right)^{-0.107} = 0.8558$$ (eqn. 6-20)

Load modification factor:

$k_c := 0.59$ (eqn. 6-26)

Reliability factor:

Read from table 6-5 for 99.99% reliability

Marin equation for endurance limit:

$k_e := 0.897$ (eqn. 6-18)

$S_{e\_z} := k_a \cdot k_{b\_z} \cdot k_c \cdot k_e \cdot S'_e = 125.9821\ MPa$

Use the modified-Goodman equation to determine the safety factor for each section:

Section z:

$$n_z := \frac{1}{\frac{\sigma'_{a\_z}}{S_{e\_z}} + \frac{\sigma'_{m\_z}}{S_{ut}}} = 1.3606$$ (eqn. 6-46)

The safety factor for yield design is given above, this is more realistic and acceptable. Since their is a high amount of torque present on the low speed shaft.

Stellenbosch University https://scholar.sun.ac.za

LS support stress analysis

15 Sep 2016 08:38:15 - Shaft_support.sm

Force and Stress analysis on support shaft

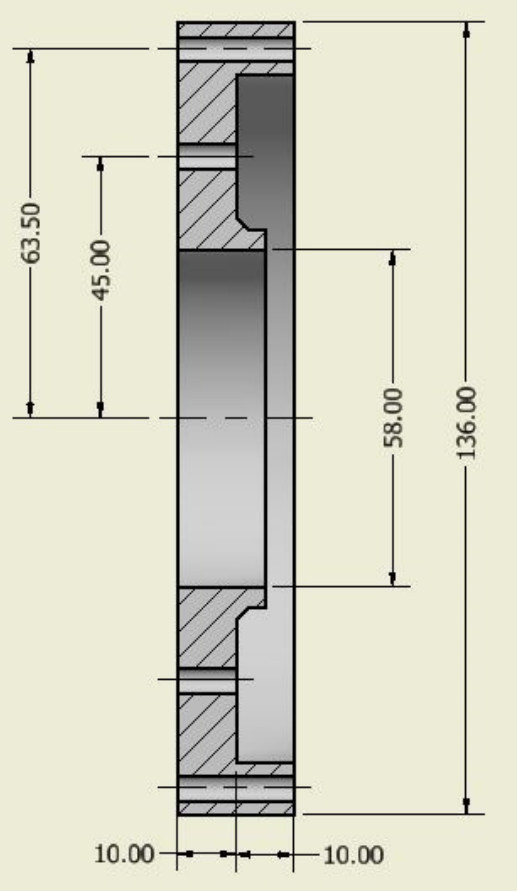

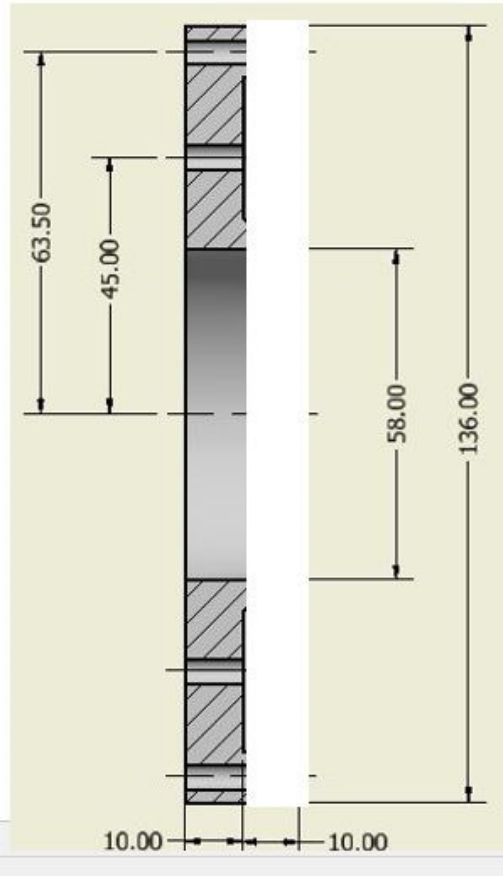

Case 1: Taking only into account force from torque and ignoring any bending, due to bearings supports. Assuming the worst case of 330 N.m

$Torque := 330\ N\ m$ Torque from simulation

Case1:

$d_{crit} := 147\ mm$

$r_1 := 63.5\ mm$

$f_{y1} := \frac{Torque}{r_1} = 5196.8504\ N$

Stellenbosch University https://scholar.sun.ac.za

Section details

Read from table 7-1

Assumging worst case

$OD_4 := 80\ mm$ $ID := 58\ mm$

$K_{t\_z} := 2.7$ $K_{ts\_z} := 2.2$

$M_{max\_z} := 0 = 0\ N\ m$ $M_{min\_z} := 0 = 0\ N\ m$

$M_{m\_z} := \frac{M_{max\_z} + M_{min\_z}}{2} = 0\ N\ m$ $M_{a\_z} := \frac{M_{max\_z} - M_{min\_z}}{2} = 0\ N\ m$

$I_z := \frac{\pi}{64} \cdot \left(OD_4^{\ 4} - ID^{\ 4} \right) = 1.4551 \cdot 10^{-6}\ m^{\ 4}$

$\sigma_{m\_z} := \frac{M_{m\_z} \cdot \frac{OD_4}{2}}{I_z} = 0$ $\sigma_{a\_z} := \frac{M_{a\_z} \cdot \frac{OD_4}{2}}{I_z} = 0\ MPa$

$T_{min\_z} := -0\ N\ m = 0\ N\ m$

$T_{max\_z} := Torque = 330\ N\ m$

$T_{m\_z} := \frac{T_{max\_z} + T_{min\_z}}{2} = 165\ N\ m$ $T_{a\_z} := \frac{T_{max\_z} - T_{min\_z}}{2} = 165\ N\ m$

$J_{G\_z} := 2 \cdot I_z = 2.9102 \cdot 10^{-6}\ m^{\ 4}$

$\tau_{m\_z} := \frac{T_{m\_z} \cdot \frac{OD_4}{2}}{J_{G\_z}} = 2.2679\ MPa$ $\tau_{a\_z} := \frac{T_{a\_z} \cdot \frac{OD_4}{2}}{J_{G\_z}} = 2.2679\ MPa$

$\sigma'_{m\_z} := \sqrt{\left(K_{t\_z} \cdot \sigma_{m\_z} \right)^2 + 3 \cdot \left(K_{ts\_z} \cdot \tau_{m\_z} \right)^2} = 8.6417\ MPa$

$\sigma'_{a\_z} := \sqrt{\left(K_{t\_z} \cdot \sigma_{a\_z} \right)^2 + 3 \cdot \left(K_{ts\_z} \cdot \tau_{a\_z} \right)^2} = 8.6417\ MPa$

$p := \frac{9.86 - 8.64}{8.64} \cdot 100 = 14.1204$

Stellenbosch University https://scholar.sun.ac.za

Material Properties First look at Acetal

Finest Quality				Acetal	Nylon 6	Cast Nylon	Cast Nylon HR	Oil-filled Nylon	Nylon 66	Omnianite PET	PET + PTFE	HDPE	PE 500	UHMWPE	Polypropylene	PVC	PTFE	Polycarbonate
Mechanical Properties	Guide to material selection																	
Tensile strength at break	ISO 527	MPa	dry	66	80	85	90	70	85	85	75	31	32	40	35	30	25	60
			moist		54	58	60	50	60									
Elongation at break	ISO 527	%	dry	40	60	20	30	35	40	5	5	>50	>50	>200	600	10	>50	100
			moist		180	100	100	100	150									
Tensile modulus of elasticity	ISO 527	MPa	dry	2700	3000	3300	3200	3100	3200	3100	2200	1000	1200	700	1300	3000	700	2300
			moist		1800	1900	1900	1700	1900									
Impact strength (Charpy)	ISO 179	kJ/m²	dry	n b	n b	n b	n b	n b	nb	n b	n b	n b	n b	n b	n b	n b	n b	n b
Notched impact strength (Charpy)	ISO 179	kJ/m²	dry	9	5	5	5	8	5	5	2	29	n b	n b	50	3	16	23
			moist		25	23	23	25	18									
Shore Hardness	ISO 868	Scale D	dry	82	80	83	83	82	83	84	83	61	65	63	70	82	55	85
Ball indentation hardness	ISO 2039-1	MPa	dry	150	160	160	170	150	170	170	-	-	50	40	60	120	30	110
			moist		70	100	100	100	100									
Coefficient of friction to steel			dry	0.30	0.42	0.42	0.40	0.34	0.42	0.25	0.20	0.30	0.25	0.20	0.35	0.70	0.08	0.50
Thermal Properties																		
Operating temp (**long term**)		°C	max	+110	+85	+100	+100	+100	95	+115	+115	+80	+80	+80	+100	+50	+260	+110
		°C	min	- 40	-40	-30	-30	-30	-30	-20	-20	-50	-100	-200	-5	-10	-200	-40
Heat Deflection Temp (**HDT-A**)	ISO 75	°C		+100	+70	+80	+80	+75	+103	+80	+75	+45	+44	+42	+65	-	+55	+135
Coefficient of linear expansion	DIN 53752	$10^{-5}\cdot K^{-1}$	dry	10	9	8	9	9	8.5	7	7	14	16	20	17	8	12	7
Dielectric Properties																		
Volume resistance	ISO 93	Ω·cm	dry	10^{15}	10^{14}	10^{14}	10^{14}	10^{14}	10^{14}	10^{13}	10^{13}	10^{14}	10^{14}	10^{14}	10^{14}	10^{16}	10^{16}	10^{15}
			moist		10^{12}	10^{12}	10^{12}	10^{12}	10^{12}									
Surface resistance	ISO 93	Ω	dry	10^{13}	10^{13}	10^{13}	10^{13}	10^{13}	10^{13}	10^{13}	10^{13}	10^{12}	10^{12}	10^{12}	10^{13}	10^{13}	10^{16}	10^{15}
			moist		10^{12}	10^{12}	10^{12}	10^{12}	0^{12}									
Dielectric strength	ISO 243	kV/mm	dry	20	25	25	25	23	25	22	20	45	45	45	100	40	48	30
			moist		16	16	16	14	16									
Physical Properties																		
Density (S.G.)	ISO 1183	g / cm³		1.41	1.14	1.15	1.15	1.14	1.14	1.38	1.40	0.95	0.95	0.94	0.93	1.38	2.18	1.20
Moisture Absorption 23°C, 50% RH	ISO 62	%		0.2	2.8	2.4	2.2	1.5	2.6	0.2	0.2	0.01	0.01	0.01	0.01	0.2	0.05	0.2
Water Absorption (till saturation)	ISO 62	%		0.7	9	7	6	4.8	8	0.5	0.4	0.1	0.1	0.1	0.1	0.2	0.05	0.36
Flammability	UL94			HB	HB	HB	HB	HB	HB	HB	HB	HB	HB	HB	HB	V-0	V-0	V-2

$S_y := 66\,MPa$ $S_{ut} := 66\,MPa$ $E := 2700\,MPa$ (Table A-20 Shigley)

Using the Marin equation to calculate the endurance limit

at the various critical points on the shaft.

Estimate the endurance limit:

if $S_{ut} \le 1400\,MPa$

$S'_e := 0.5 \cdot S_{ut}$ (eqn. 6-8)

else

$S'_e := 1400\,MPa$

$S'_e = 33\,MPa$

Surface condition modification factor:

$a := 4.51$ $b := -0.265$ Read from table 6-2 for Machined or cold-drawn

Stellenbosch University https://scholar.sun.ac.za

$$k_a := a \cdot \left(\frac{S_{ut}}{1\ MPa} \right)^b = 1.4859 \qquad \text{(eqn. 6-19)}$$

Size modification factor:

$$k_{b\_z} := 1.24 \cdot \left(\frac{OD_4}{1\ mm} \right)^{-0.107} = 0.7759 \qquad \text{(eqn. 6-20)}$$

Load modification factor:

$$k_c := 0.59 \qquad \text{(eqn. 6-26)}$$

Reliability factor:

$k_e := 0.897$ Read from table 6-5 for 99.99% reliability

Marin equation for endurance limit:

$$S_{e\_z} := k_a \cdot k_{b\_z} \cdot k_c \cdot k_e \cdot S'_e = 20.1348\ MPa \qquad \text{(eqn. 6-18)}$$

Use the modified-Goodman equation to determine the safety factor for each section:

Section z:

$$n_z := \frac{1}{\frac{\sigma'_{a\_z}}{S_{e\_z}} + \frac{\sigma'_{m\_z}}{S_{ut}}} = 1.7853 \qquad \text{(eqn. 6-46)}$$

The safety factor for yield design is given above, this is considered acceptable. However, a more advanced plastic, PEEK, was used to ensure dimensional stability.

Stellenbosch University https://scholar.sun.ac.za

Threaded rods and bolts stress analysis

13 Sep 2016 07:51:51 - Bolts.sm

Shaft to bolt analysis

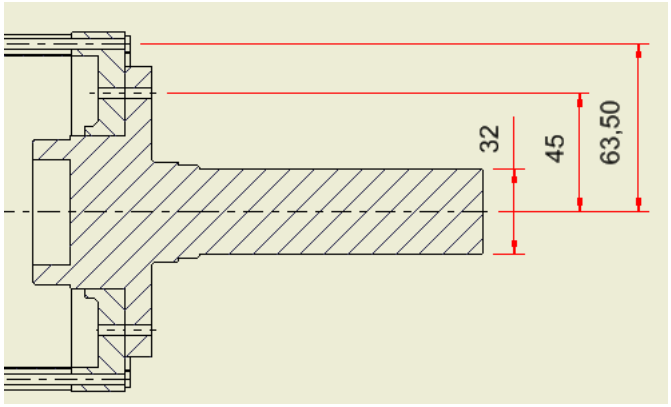

CASE 1: most critical case with least amount of bolts at the smallest radius

$n_{bolts} := 8$ number of bolts:

$r_{shaft} := 45\ mm$ radius to bolts

$d_{bolt} := 3.141\ mm$ minor diameter of bolt

$Torque := 265\ N\ m$ Torque from simulation

$F := \frac{Torque}{r_{shaft}} = 5888.8889\ N$

$A_{bolt} := \frac{d_{bolt}^{2}}{4} \cdot \pi = 7.7486 \cdot 10^{-6}\ m^{2}$

$\tau := \frac{F}{n_{bolts} \cdot A_{bolt}} = 9.4999 \cdot 10^{7}\ Pa$

$n := \frac{S_{sy}}{\tau} = 1.8829$ Safety factor

$S_y := 310\ MPa$ Grade 4.8

$S_{sy} := 0.577 \cdot S_y = 1.7887 \cdot 10^{8}\ Pa$

CASE 2: Assumed to be less critical, since more bolts on larger radius

$n_{bolts} := 14$ number of bolts:

$r_{shaft} := 63.5\ mm$ radius to bolts

$d_{bolt} := 3.141\ mm$ minor diameter of bolt

$Torque := 265\ N\ m$ Torque from simulation

$F := \frac{Torque}{r_{shaft}} = 4173.2283\ N$

$S_y := 340\ MPa$ Grade 4.8

$S_{sy} := 0.577 \cdot S_y = 1.9618 \cdot 10^{8}\ Pa$

Stellenbosch University https://scholar.sun.ac.za

$$A_{bolt} := \frac{d_{bolt}^{2}}{4} \cdot \pi = 7.7486 \cdot 10^{-6}\ m^{2}$$

$$\tau := \frac{F}{n_{bolts} \cdot A_{bolt}} = 3.847 \cdot 10^{7}\ Pa$$

$$n := \frac{S_{sy}}{\tau} = 5.0996$$ Safety factor

Thus it can be seen that the bolts must have a grade of 4.8 to ensure they will be strong enough. Also in the calculation pure shear loading was assumed, with no bending. This was assumed since the gearbox was designed in a manner that no, or little, axial and radial forces are generated. If bending however if bending does occurs failure of bolt may result.